JAERI-M
85-169

DESIGN CONCEPTS AND PERFORMANCE TESTS OF THE 60GHz ELECTRON CYCLOTRON HEATING (ECH) SYSTEM FOR THE JFT-2M TOKAMAK

November 1985

Katsumichi HOSHINO, Takumi YAMAMOTO, Hisato KAWASHIMA
Takatoshi SHIBATA and Toshihiro SHIBUYA

日本原子力研究所
Japan Atomic Energy Research Institute

JAERI-Mレポートは，日本原子力研究所が不定期に公刊している研究報告書です。
入手の問合わせは，日本原子力研究所技術情報部情報資料課（〒319-11 茨城県那珂郡東海村）あて，お申しこしください。なお，このほかに財団法人原子力弘済会資料センター（〒319-11 茨城県那珂郡東海村日本原子力研究所内）で複写による実費領布をおこなっております。

JAERI-M reports are issued irregularly.
Inquiries about availability of the reports should be addressed to Information Division Department of Technical Information, Japan Atomic Energy Research Institute, Tokaimura, Naka-gun, Ibaraki-ken 319-11, Japan.

編集兼発行　日本原子力研究所
印　　刷　日青工業株式会社

JAERI-M 85-169

Design Concepts and Performance Tests of the 60GHz Electron Cyclotron Heating (ECH) System for the JFT-2M Tokamak

Katsumichi HOSHINO, Takumi YAMAMOTO, Hisato KAWASHIMA,
Takatoshi SHIBATA and Toshihiro SHIBUYA
Department of Thermonuclear Fusion Research,
Naka Fusion Research Establishment, JAERI

(Received October 7, 1985)

60GHz overmoded microwave launch system for the JFT-2M tokamak is described. The basic design concepts, specifications of each microwave component and the results of the performance tests are reported. The transmission of the microwave power is done in the circular TE_{01} mode which has a low loss along the overmoded circular transmission components of 33 m in length. The microwave power of 80 - 90 kW, pulse width 100 ms in the circular TE_{11} mode is finally launched into the JFT-2M tokamak plasma.

Keywords: Electron Cyclotron Heating System, Gyrotron, Microwave Components, JFT-2M Tokamak.

JAERI－M　85－169

JFT－2Mトカマク用の60GHz電子サイクロトロン加熱（ECH）システムの設計概念および発振試験結果

日本原子力研究所那珂研究所核融合研究部

星野　克道，山本　　巧，川島　寿人
柴田　孝俊，渋谷　俊広

（1985年 10月 7日受理）

JFT－2Mトカマク装置用のオーバーサイズ径の導波管を用いた60GHz マイクロ波入射装置について報告する。基本的設計思想，各立体回路要素の特性および発振試験結果について述べる。

高周波電力は，オーバーサイズ径の伝送系（全長約33m）により，低損失の円形TE_{01}モードで伝送される。

最終的に円形TE_{11}モードで80－90kW，パルス幅100msのマイクロ波電力がJFT－2Mトカマクプラズマ中に入射された。

Contents

1. Introduction 1
2. Physical Considerations about the Wave which should be launched 3
2.1 Consideration about the Cutoff Density of the Electromagnetic Wave 3
2.2 Consideration about the Power Absorption at the Electron Cyclotron Resonance Layer 7
2.3 Summary 13
3. ECH System 18
3.1 RF Transmission System 18
3.1.1 General Design Concepts of the RF Transmission System 18
(1) Joule Loss in the Circular Waveguide and the Minimization of the Loss 19
(2) Field Strength in the Waveguide and Avoidance of the Breakdown 24
(3) Mode Conversion at the Wave Guide Bend 28
3.1.2 Constitution of the RF Transmission System 30
3.1.3 High Power Overmoded Microwave Transmission Components 30
(1) Two Kinds of the Mode Converters ($TE_{02} \rightarrow TE_{01}$, $TE_{01} \rightarrow TE_{11}$) .. 30
(2) Corrugated 90° Bends 36
(3) Raised Cosine Tapers 36
(4) Straight Waveguides 40
(5) Vacuum Window 40
(6) DC Break/Mode Filter 40
(7) Conical Horn Antenna 40
(8) Arc Detecters 45
3.2 RF Monitor System 45
(1) Sampler/Arc Detector and Monitor Circuit of the general Power and Frequency 47
(2) Mode Filter 47
(3) Raised Consine Tapers 47
(4) TE_{02} mode Directional Coupler 47
(5) Microwave Circuits for the Power and Frequency Detection 47
(6) Water Load/Calorimeter 52
3.3 Gyrotron 58
3.4 Super Conducting Magnet System 62
3.5 Power Supply/Cooling System 62

3.6 Gas supply 67
4. Power Tests of the ECH System 71
4.1 Operation Region of the Gyrotron 71
4.2 Monitor Waveform during the Gyrotron Operation 73
4.3 Measurement of the Overall Transmission Loss in the RF Transmission System (Cold Test) 75
4.4 Measurement of the Forward RF Power 75

Conclusion 79
Acknowledgements 79
References 80
Appendix 1. RF Current Drive (LHH + ECH) and Electron Cyclotron Heating Experiments on JFT-2M Tokamak 81
Appendix 2. Layouts of the ECH system 88
Appendix 3. Main control panel of the ECH system 89
Appendix 4. Drawings of the microwave components 90

目　　次

1. 序 …… 1
2. 入射される波の物理的検討 …… 3
2.1 電磁波のしゃ断密度の検討 …… 3
2.2 電子サイクロトロン共鳴層でのパワー吸収の検討 …… 7
2.3 まとめ …… 13
3. ＥＣＨ装置 …… 18
3.1 高周波伝送系 …… 18
3.1.1 高周波伝送系の一般的設計概念 …… 18
(1) 円形導波管のジュール損失及び損失の低減 …… 19
(2) 円形導波管中の電界強度及び絶縁破壊の低減 …… 24
(3) 円形導波管の曲がりによるモード変換 …… 28
3.1.2 高周波伝送系の構成 …… 30
3.1.3 大電力オーバーサイズマイクロ波伝送要素 …… 30
(1) 二種のモード変換器（$TE_{02} \rightarrow TE_{01}$, $TE_{01} \rightarrow TE_{11}$） …… 30
(2) 溝付き90度ベンド …… 36
(3) レイズド余弦テーパー …… 36
(4) 直線導波管 …… 40
(5) 真空窓 …… 40
(6) ＤＣ絶縁/モードフィルター …… 40
(7) 円錘ホーンアンテナ …… 40
(8) アーク検出器 …… 45
3.2 高周波モニター装置 …… 45
(1) サンプラ/アーク検出器及び一般パワー，周波数のモニター回路 …… 47
(2) モードフィルター …… 47
(3) レイズド余弦テーパー …… 47
(4) TE_{02} モード方向性結合器 …… 47
(5) パワー，周波数検出のためのマイクロ波回路 …… 47
(6) 水負荷/熱量計 …… 52
3.3 ジャイロトロン …… 58
3.4 超電導電磁石装置 …… 62
3.5 電源/冷却装置 …… 62
3.6 ガス供給 …… 67
4. パワー試験 …… 71
4.1 ジャイロトロンの動作領域 …… 71

4.2 ジャイロトロン動作中のモニター波形 …… 73
4.3 高周波伝送系での全伝送損失の測定（コールド試験）…… 75
4.4 前方高周波電力の測定結果 …… 75
結 論 …… 79
謝 辞 …… 79
参考文献 …… 80
付録1 ＪＦＴ－２Ｍにおける高周波電流駆動（ＬＨＨ＋ＥＣＨ）及び
電子サイクロトロン加熱実験 …… 81
付録2 ＥＣＨ装置の配置 …… 88
付録3 ＥＣＨ装置の主制御パネル …… 89
付録4 マイクロ波要素の図面 …… 90

1. Introduction

The electromagnetic wave (EMW) with the freuency close to the electron cyclotron frequency (We call the EMW as ECW) is absorbed at the electron cyclotron resonance (ECR) layer via the electron cyclotron damping in the linear theory. For the heating of the tokamak plasmas, this local power deposition is favourable for the efficient core plasma heating, or the current profile control to improve the MHD stability. Due to the local power deposition and the good propagation characteristic of the EMW from the plasma edge region (absence of the evanescent region), the impurity problem may be minimized in the ECH. Besides, there is a possibility of driving the toroidal current which has a role of confining the tokamak plasma.

28 GHz ECH was first studied[1)~4)] in the JFT-2 (R = 90 cm, a = 25 cm) tokamak of JAERI. Electron heatings by the fundamental resonance ($\omega = \omega_{ce}$, ω_{ce}: electron cyclotron frequency) were investigated by launching X, O, and TE_{02} mode. Efficient electron heating and localized power deposition were varified. It was shown that the mode conversion at the upper hybrid resonance layer contributes to the heating by the off-center ECR layer. On the other hand, density limit of heating ($n_{e0} \simeq 1.5 \times 10^{13}$ cm^{-3}) by the EMW was observed in consistent with the theoretical cutoff density. Therefore, for the heating of the higher density plasma, the EMW of the higher frequency has to be launched in the higher magnetic field, or the harmonic electron cyclotron frequency heating has to be employed.

From these points of view (as will be described in chap. 2), 60 GHz gyrotron was chosen for the ECH of the JFT-2M tokamak machine which has a noncircular plasma cross section (R = 131 cm, a = 35 × 55 cm). That is a maximum frequency now available in commerce. The JFT-2M tokamak operates with the toroidal magnetic field of less than B_t = 1.5 T, because the capacity of the power supply is restricted. Therefore, the 2nd harmonic heating ($\omega = 2\omega_{ce}$) was taken. The 2nd ECR layer is at the center of the plasma column when Bt is 1.07 T.

The aims of the first stage ECH experiment on the JFT-2M tokamak which was carried in Nov.-Dec. last year were to investigate

(1) the effects of the ECH to the current drive/ramp up by the lower hybrid wave (LHW), and

(2) electron heating by the 2nd harmonic extraordinary mode

(X-mode) ECH.

The first stage experimental results are reported briefly in the paper[5] submitted to the 12th European Conf. on Controlled Fusion and Plasma Physics which is given in the appendix.

We describe the 60 GHz ECH system of the JFT-2M tokamak, by putting the stress on the basic design concepts and performance tests. Therefore the descriptions of the high voltage power supply or super conducting magnet system are minimum.

The ECW is launched from a horn antenna. The wave launch by the horn antenna has an advantage that the wave power can be radiated into a vacuum region. Therefore the antenna loading (matching) as is the important problem in the case of coupling by the loop antenna is not a problem in the launch of the ECW.

The points of the design of the ECH system may be summarized as follows.

(1) How to choose the launch angle with respect to the magnetic field, and launched mode (physics consideration).

(2) How to minimize the rf transmission loss between the gyrotron and the antenna.

(3) How to avoid the break down in the waveguides for the transmission of high rf power density.

(4) How to know the exact imput power to the plasma.

These points are described in this report.

In Chap. 2, the physics consideration are presented. In Chap. 3, the basic design concepts and specifications of each microuave components are described. Gyrotron, super conducting magnet, power supply system and gas supply are also described briefly in this chapter. In Chap. 4, the results of the cold and hot tests of the whole rf transmission system are reported. Finally the experimental results of the first stage ECH of a tokamak plasma are given in the Appendix.

2. Physical Considerations about the Wave which should be launched

2.1 Consideration about the Cutoff Density of the Electromagnetic Wave

"Cutoff" and "resonance" of the wave in the plasma is obtained from the cold plasma dispersion relation which is a polynomial of the forth order in the refractive index n, and expressed as[6)]

$$An^4 - Bn^2 + C = 0 \tag{2.1}$$

where

$$A = S \sin^2\theta + P \cos^2\theta \tag{2.2}$$

$$B = RL \sin^2\theta + PS(1+\cos^2\theta) \tag{2.3}$$

$$C = PRL \tag{2.4}$$

$$R = 1 - \sum_{\alpha} \frac{\omega_{p\alpha}^2}{\omega^2} \left(\frac{\omega}{\omega + \varepsilon_{\alpha}\omega_{c\alpha}} \right) \tag{2.5}$$

$$L = 1 - \sum_{\alpha} \frac{\omega_{p\alpha}^2}{\omega^2} \left(\frac{\omega}{\omega - \varepsilon_{\alpha}\omega_{c\alpha}} \right) \tag{2.6}$$

$$P = 1 - \sum_{\alpha} \frac{\omega_{p\alpha}^2}{\omega^2} \tag{2.7}$$

$$S = \frac{1}{2}(R + L) \ . \tag{2.8}$$

θ denotes an angle between the magnetic field vector $\vec{B}$ and the wave vector $\vec{k}$, ω denotes the wave frequency, $\omega_{p\alpha}$ is the plasma frequency of the particles of species α, and $\omega_{c\alpha}$ is the cyclotron frequency of species α. ε_{α} is the sign of the electric charge of particle α.

A "cutoff" of the wave is defined by $n^2 = 0$. Then,

$$C = 0 \ . \tag{2.9}$$

Namely,

$$P = 0 \ , \text{ (plasma cutoff)} \tag{2.10}$$

or

$$R = 0 \ , \text{ (right hand wave cut off)} \tag{2.11}$$

or

$$L = 0 \ , \text{ (left hand wave cutoff)} \ . \tag{2.12}$$

The equations (2.10) - (2.12) determines the cutoff frequency $\omega = \omega_c$. For a single species electron plasma,

$$\omega_c = \omega_{pe} \quad \text{(plasma frequency)} \tag{2.13}$$

$$\omega_c = \omega_R = \frac{\omega_{ce}}{2} + \frac{1}{2}\sqrt{\omega_{ce}^2 + 4\omega_{pe}^2}$$

$$\text{(reght hand wave cutoff frequency)} \tag{2.14}$$

$$\omega_c = \omega_L = -\frac{\omega_{ce}}{2} + \frac{1}{2}\sqrt{\omega_{ce}^2 + 4\omega_{pe}^2}$$

$$\text{(left hand wave cutoff frequency).} \tag{2.15}$$

A "resonance" is defined by $n^2 \to \infty$.

Then,

$$A = 0 \ . \tag{2.16}$$

Namely,

$$S \sin^2\theta + P \cos^2\theta = 0 \ . \tag{2.17}$$

For the perpendicular propagation ($\theta = \frac{\pi}{2}$), the resonance condition becomes

$$S = 0 \ . \tag{2.18}$$

This condition leads to the upper hybrid resonance frequency expressed as,

$$\omega_{UH} = \sqrt{\omega_{pe}^2 + \omega_{ce}^2}$$

$$\text{(upper hybrid resonance frequency).} \tag{2.19}$$

These well known cutoff's and a resonance are obtained from the conditions on n^2. Further, n^2 is decomposed into the perpendicular component and parallel component as

$$n^2 = n_\perp^2 + n_{/\!/}^2 \ . \tag{2.20}$$

Substituting eq. (2.20) into eq. (2.1), one obtains the two branches of the wave as

$$n_\perp^2 = 1 - n_{/\!/}^2 - X \pm \frac{XY}{2} \frac{\sqrt{(1-n_{/\!/}^2)^2 Y^2 + 4n_{/\!/}^2(1-X)} \mp Y(1+n_{/\!/}^2)}{1 - X - Y^2} \tag{2.21}$$

where

$$X \equiv \frac{\omega_{pe}^2}{\omega^2} \propto n_e \text{ (density)}, \quad Y \equiv \frac{|\omega_{ce}|}{\omega} \propto B \text{ (mangetic field)}. \tag{2.22}$$

Eq. (2.21) is the Appleton-Hartree dispersion relation. The branch expressed by the upper sign is called the "ordinary mode (O-mode)" and that of the lower sign as the "extraordinary mode (X-mode)".

The propagation of the wave is possible in the region $n_\perp^2 > 0$. The wave evanescence occurs in the region $n_\perp^2 < 0$. The boundary is expressed by

$$n_\perp^2 = 0 \ . \tag{2.23}$$

By substituting eq. (2.23) into (2.21), one obtains the cutoff's and a resonance[7] as follows.

$$X = 1 \quad \text{O-mode cutoff } (\omega_{pe}) \tag{2.24}$$

$$X = (1 - n_{/\!/}^2)(1 + Y) \tag{2.25}$$

$$\begin{cases} n_{/\!/}^2 = \dfrac{Y}{Y+2} & \left.\begin{matrix}\text{O-mode}\\ \text{X-mode}\end{matrix}\right\} \text{ cutoff } (\omega_L) \\ n_{/\!/}^2 \leq \dfrac{Y}{Y+2} & \text{X-mode cutoff } (\omega_L) \\ n_{/\!/}^2 > \dfrac{Y}{Y+2} & \text{O-mode cutoff } (\omega_L) \end{cases}$$

$$X = (1 - n_{/\!/}^2)(1 - Y) \quad \text{X-mode cutoff } (\omega_R) \tag{2.26}$$

$$X = 1 - Y^2 \quad \text{X-mode resonance } (\omega_{UH}). \tag{2.27}$$

The confluence point of O-mode and X-mode is expressed by

$$X = 1 + \frac{(1 - n_{/\!/}^2)^2}{4n_{/\!/}^2} Y^2 \ . \tag{2.28}$$

Thus one obtains the $n_{/\!/}$ dependence of the cutoff density of the EMW.

Next, we calculate the cutoff and resonance density for the

fundamental (S = 1) and harmonic (S = 2, 3) waves. We set the frequency of the wave as

$$\omega = S\,\omega_{ce} \quad (S = 1, 2, 3, \ldots) \tag{2.29}$$

Here we put the restriction that $S \leq 3$. Then,

$$Y = \frac{|\omega_{ce}|}{\omega} = \begin{cases} 1 & (S = 1) \\ 1/2 & (S = 2) \\ 1/3 & (S = 3) \end{cases} . \tag{2.30}$$

Therefore one obtains

(1) S = 1

X = 1 O-mode cutoff (ω_{pe})

$X = 2(1 - n_{/\!/}^2)$

$$\begin{cases} n_{/\!/}^2 \leqq 1/3 & \text{X-mode cutoff } (\omega_L) \\ n_{/\!/}^2 \geqq 1/3 & \text{O-mode cutoff } (\omega_L) \end{cases} \tag{2.31}$$

X = 0 (ω_R)

X = 0 (ω_{UH}) no accessibility from the low field side

$$X = 1 + \frac{(1 - n_{/\!/}^2)^2}{4n_{/\!/}^2}$$

(2) S = 2

X = 1 O-mode cutoff (ω_{pe})

$$X = \frac{3}{2}(1 - n_{/\!/}^2)$$

$$\begin{cases} n_{/\!/}^2 \leqq 1/5 & \text{X-mode cutoff } (\omega_L) \\ n_{/\!/}^2 \geqq 1/5 & \text{O-mode cutoff } (\omega_L) \end{cases} \tag{2.32}$$

$$X = \frac{1}{2}(1 - n_{/\!/}^2) \quad \text{X-mode cutoff } (\omega_R)$$

X = 3/4 X-mode resonance (ω_{UH})

$$X = 1 + \frac{(1 - n_{/\!/}^2)^2}{16n_{/\!/}^2}$$

(3) S = 3

X = 1 O-mode cutoff (ω_{pe})

$$X = \frac{4}{3}(1 - n_{/\!/}^2)$$

$$\begin{cases} n_{/\!/}^2 \leqq 1/7 & \text{X-mode cutoff } (\omega_L) \\ n_{/\!/}^2 \geqq 1/7 & \text{O-mode cutoff } (\omega_L) \end{cases} \tag{2.33}$$

$$X = \frac{2}{3}(1 - n_{/\!/}^2) \quad \text{X-mode cutoff } (\omega_R)$$

$$X = 8/9 \quad \text{X-mode resonance } (\omega_{UH})$$

$$X = 1 + \frac{(1 - n_{/\!/}^2)^2}{36 n_{/\!/}^2} \quad .$$

The cutoff density expressed by (2.31) ~ (2.33) is depicted in Fig. 2-1. The cutoff density of the X-mode is represented by the solid line and that for the O-mode is represented by the broken line. As shown, the cutoff density decreases as $n_{/\!/}$. The cutoff density of the O-mode is larger than that of the X-mode except the s = 1 case.

For the perpendicular propagation ($n_{/\!/} = 0$), $n^2 = n_\perp^2$, the cutoff frequency is expressed by ω_{pe} (O-mode), ω_R, ω_L (X-mode). The frequency dependence of the cutoff density n_c is depicted in Fig. 2-2. The cutoff density n_c is a quadrature of the frequency. For example, the cutoff density of the O-mode is $n_{co} = 4.46 \times 10^{13}$ cm^{-3} for S = 2 and f = 60 GHz.

It is desireable to choose the frequency as large as possible, and the injection angle should near $\frac{\pi}{2}$ from the point of view of the cutoff density. But, further consideration about the damping rate at the ECR layer is important. That point of view is discussed in the next section.

2.2 Consideration about the Power Absorption at the Electron Cyclotron Resonance Layer

For the local efficient heating, a large energy absorption rate in single path at the ECR layer ($\omega = S\,\omega_{ce}$) is required. The absorption rate is a function of the launch angle with respect to the stationary magnetic field namely a function of the parallel refractive index $n_{/\!/}$, harmonic number S and plasma density n_e, once the wave frequency is fixed. The absorbed power in single path P_{ab} at the ECR layer is calculated using the geometrical optics approximation.

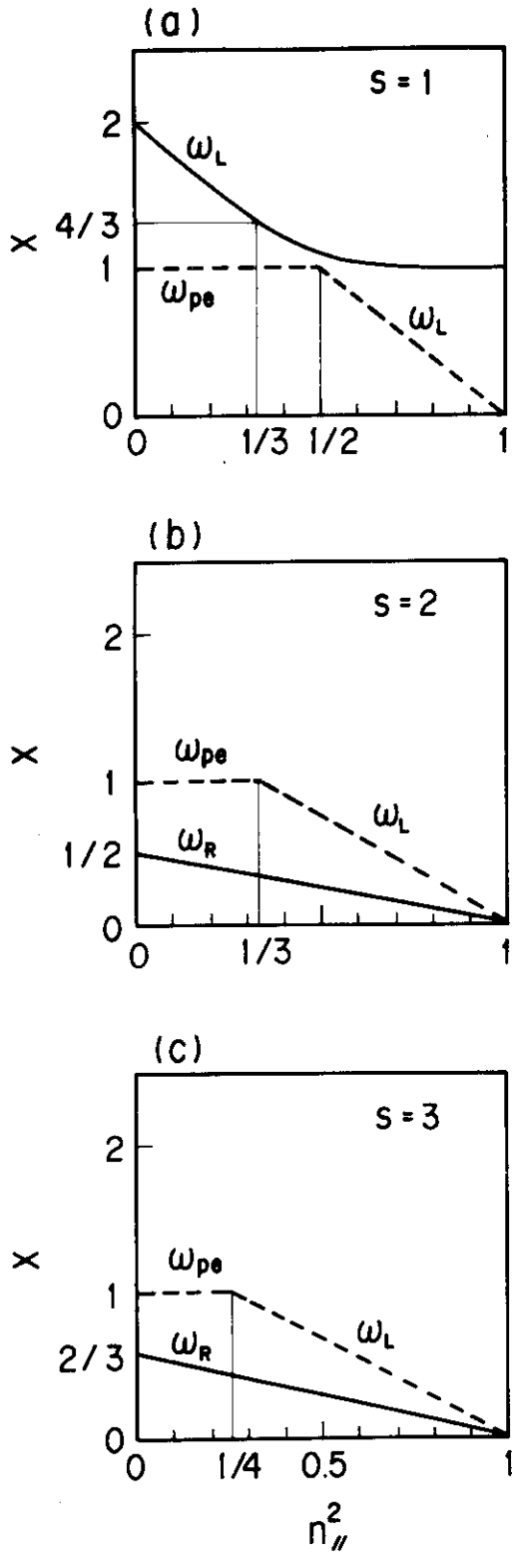

Fig. 2-1 Cutoff density as a function of the parallel refractive index $n_{//}$. $X \equiv \frac{\omega_{pe}^2}{\omega^2} \propto n_e$. S is a harmonic number. $\omega = S\omega_{ce}$. (a) S = 1, (b) S = 2, (c) S = 3.

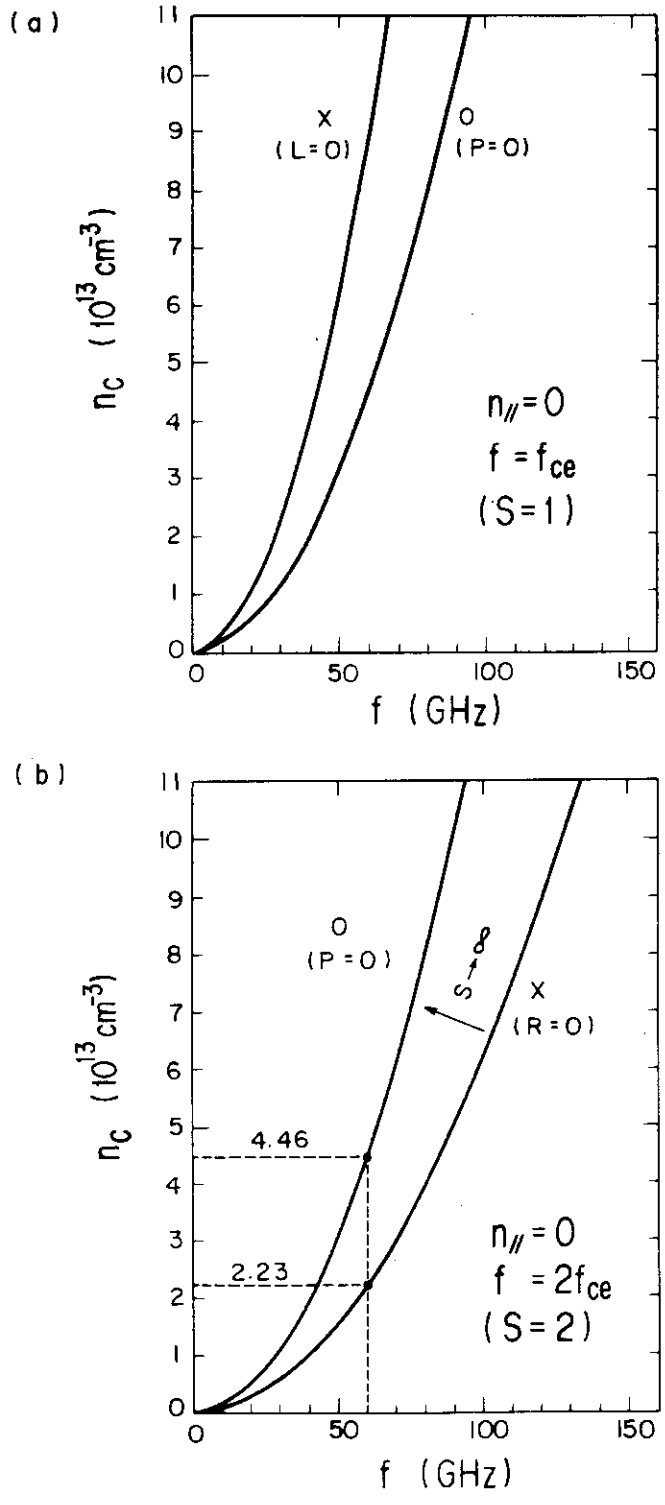

Fig. 2-2 Cutoff density n_c as a function of the frequency f. $n_{//} = 0$. (a) $f = f_{ce}$, S = 1, (b) $f = 2f_{ce}$, S = 2.

$$P_{ab} = P_{(\ell_1)}\left(1 - e^{\int_{\ell_1}^{\ell_2} 2\mathrm{Im}\, k_\perp \, d\ell}\right) \tag{2.34}$$

Here, P_{ab} denotes the absorbed power between the coordinate $\ell = \ell_2, \ell_1$ and $P(\ell_1)$ is the wave power at $\ell = \ell_1$. The imaginary part of the perpendicular wave number $\mathrm{Im}\, k_\perp$ in (2.34) is obtained from the warm plasma dispersion relation which is a complex transcendental equation expressed as[6]

$$\begin{vmatrix} -n_{/\!/}^2 + K_{xx} & K_{xy} & n_\perp n_{/\!/} + K_{xz} \\ K_{yx} & -n_\perp^2 - n_{/\!/}^2 + K_{yy} & K_{yz} \\ n_\perp n_{/\!/} + K_{zx} & K_{zy} & -n_\perp^2 + K_{zz} \end{vmatrix} = 0 \ . \tag{2.35}$$

Here K_{ij} (i, j = x, y, z) are the components of the warm plasma dielectric tensor. The dispersion relation (2.35) is solved exactly by the numerical method. This method was used in 4). But in this report, an analytic solution of (2.35) with an approximation which uses the real part of the cold refractive index. By the analytic solution the parameter dependence of the absorption is easily obtained without using a computer and one can get a good perspective about the absorption rate.

An intensity of the radiation I (unit: $J\, m^{-2} str^{-1}$) is obtained from the equation of transfer[8]. Using a source function S of the plasma media the intensity is written as

$$I(\ell_2) = I(\ell_1)\, e^{-\tau(\ell_2, \ell_1)} + \int_{\ell_1}^{\ell_2} S(\ell') e^{-\tau(\ell, \ell')} \, d\ell' \ . \tag{2.36}$$

The second term of the right hand side of (2-36) represents the contribution of the emission from the plasma. The first term in the right hand side represents that the intensity at $\ell = \ell_2$ is reduced by a factor $e^{-\tau}$ due to the absorption by the intervening medium. τ is called as the optical thickness and is the function of the absorption coefficient of the medium between $\ell_2 \leq \ell \leq \ell_1$. The absorbed fraction of the intensity is thus expressed as

$$\frac{I(\ell_1) - I(\ell_2)}{I(\ell_1)} = 1 - e^{-\tau(\ell_2,\ell_1)} \equiv \frac{P_{ab}}{P} . \tag{2.37}$$

The optical thickness τ of a finite density plasma $\left(\left(\frac{\omega_p}{S\omega_{ce}}\right)^2 \lesssim 1\right)$ in a space-dependent magnetic field is obtained using the real part of the refractive index N'[9] as,

$$S = 1$$

$$\tau_1^{(O)} = \pi^2 N_o' \left(\frac{\omega_p}{\omega_{ce}}\right)^2 \left(\frac{V_t}{C}\right)^2 \frac{(1+2\cos^2\theta)^2\sin^4\theta}{(1+\cos^2\theta)^3} \frac{L_B}{\lambda_0}$$

$$\tau_1^{(X)} = \pi^2 N_X'^5 \left(1+\frac{\omega_p^2}{\omega_{ce}^2}\right)^2 \left(\frac{\omega_{ce}}{\omega_p}\right)^2 \left(\frac{V_t}{C}\right)^2 \cos^2\theta \frac{L_B}{\lambda_0}$$

$$N'^2_{O,X} = \frac{1}{\sin^2\theta} \left\{1 - \left(\frac{\omega_p}{\omega_{ce}}\right)^2 + \frac{\sin^2\theta}{2} \mp \frac{1}{2}\sqrt{\sin^4\theta + 4\left(1-\left(\frac{\omega_p}{\omega_{ce}}\right)^2\right)^2 \cos^2\theta}\right\}$$

$$S \geq 2 \tag{2.38}$$

$$\tau_s^{(O,X)} = \frac{\pi^2 S^{2(S-1)}}{2^{S-1}(S-1)!} \left(\frac{\omega_p}{\omega_{ce}}\right)^2 \left(\frac{V_t}{C}\right)^{2(S-1)} (\sin\theta)^{2(S-1)} (1+\cos^2\theta)\, \mu_s^{(O,X)}(\theta) \frac{L_B}{\lambda_0}$$

$$N'^2_{O,X} = 1 - \left(\frac{\omega_p}{s\omega_{ce}}\right)^2 f_{O,X;S} .$$

Here suffix (O) represents the ordinary mode and (X) represents the extraordinary mode.

$$V_t = \sqrt{\frac{Te}{m}} = 4.1938 \times 10^5 \sqrt{\frac{Te[eV]}{e}} \quad [m/s]$$

(electron thermal velocity)

$$C = 2.9979 \times 10^8 \quad [m/s]$$

(light velocity in vacuum)

$$\omega_p = 2\pi \times 89.8 \times 10^9 \sqrt{\frac{n_e[m^{-3}]}{10^{20}}} \quad [s^{-1}]$$

(plasma frequency)

$$\omega_{ce} = 2\pi \times 28.0 \times 10^9 \ B\ [T] \quad [s^{-1}]$$

(electron cyclotron frequency)

θ : angle between $\vec{k}$ and $\vec{B}$

$$\lambda_0 = \frac{2\pi C}{\omega_{ce}}$$

$$L_B = \frac{B_o}{|dB_o/d\ell|} = \frac{R_o}{\sin\theta}$$

$$\mu_s^{(O,X)}(\theta) = \frac{N'^{2S-3}_{(O,X)} \ (S-1)^2 \left(1 - \frac{S+1}{S} f_{(O,X)S}\right)^2}{(1+\cos^2\theta)\sqrt{a_s^2 + b_s^2}}$$

$$a_s^2 = \left[1 + \frac{1 - \left(\frac{\omega_p}{s\omega_{ce}}\right)^2 N'^2\cos^2\theta}{\left(1 - \left(\frac{\omega_p}{s\omega_{ce}}\right)^2 - N'^2\sin^2\theta\right)^2} S^2 \left(1 - \frac{S^2-1}{S^2} f_{(o,x)s}\right)^2\right]^2 \sin^2\theta$$

$$b_s^2 = \left[1 + \frac{1 - \left(\frac{\omega_p}{s\omega_{ce}}\right)^2}{1 - \left(\frac{\omega_p}{s\omega_{ce}}\right)^2 - N'^2\sin^2\theta} S^2 \left(1 - \frac{S^2-1}{S^2} f_{(o,x)s}\right)^2\right]^2 \cos^2\theta$$

$$f_{\substack{o,s \\ x,s}} = \frac{2\left(S^2 - \left(\frac{\omega_p}{\omega_{ce}}\right)^2\right)}{2\left(S^2 - \left(\frac{\omega_p}{\omega_{ce}}\right)^2\right) - (\sin^2\theta \mp \rho_s)}$$

$$\rho_s^2 = \sin^4\theta + \frac{4}{S^2}\left(S^2 - \left(\frac{\omega_p}{\omega_{ce}}\right)^2\right)^2 \cos^2\theta \ .$$

The calculated refractive index $N'(\equiv \mathrm{Re}\, n_\perp)$ is depicted in Fig. 2-3 (a) ~ (c). For the low density plasma, Re $n_\perp$ is nearly 1.

The calculated absorption rate in single path across the ECR layer P_{ab}/P is shown in Fig. 2-4 (a) ~ (c). The frequency of the wave is fixed to f = 60 GHz and the electron temperature at the ECR layer to T_e = 600 eV in the calculation. The angle θ and density n_e are taken as the variables. As shown in the figure, the absorption of the X-mode is large for $\omega = \omega_{ce}$ (s = 1) and $\omega = 2\omega_{ce}$ (s = 2) but small for $s \geq 3$. The absorption of the O-mode is small (a few per cent) except s = 1. By the perpendicular injection ($\theta \simeq 90°$) the 2nd harmonic X-mode is absorbed almost completely at the ECR layer. Namely, the local power deposition which is necessary for the profile control is possible by the 2nd harmonic heating. A small absorption at the ECR layer is unfavourable for the local heating, because the power deposition profile on the ECR layer becomes broad by the divergence of the beam due to the multiple reflections at the metallic chamber wall.

2.3 Summary

1. Consideration from the point of view of the cut off density, the frequency of the wave has to be as large as possible and the perpendicular injection should be taken. If the wave frequency is fixed in the perpendicular injection, the cutoff density n_c of the EMW has a relation as follows (c.f. Fig. 2-1),

$$n_{c,x}(S = 1) > n_{c,o} > n_{c,x}(S \to \infty) > \cdots > n_{c,x}(S = 3) > n_{c,x}(S = 2).$$

2. Consideration from the point of view of the absorption at the ECR layer, X-mode of the lower harmonics ($S \leq 2$) should be launcled for the large absorption rate at the ECR layer. In the launch of the 2nd harmonic X-mode, near perpendicular injection should be taken for the large absorption at the ECR layer.
3. Though the fundamental (S = 1) X-mode has large n_c and large absorption rate, the injection should be at the high field side of the torus and should be launched obliquely. But, from the technical point of view, the inside launch is more difficult than the outside launch.
4. The maximum frequency now available is 60 GHz which corresponds to the electron cyclotron frequency at B = 2.14 T (S = 1) or B = 1.07 T.

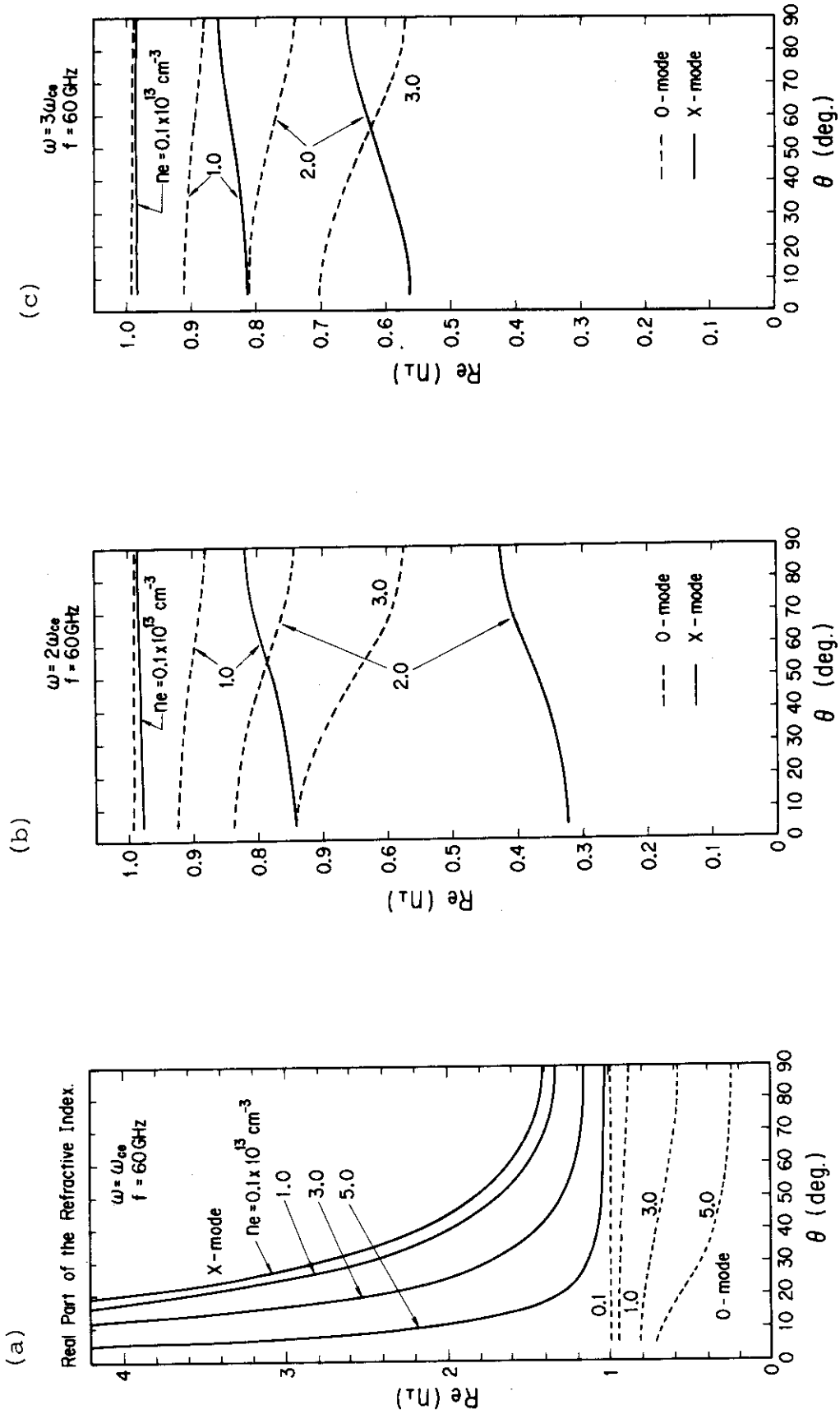

Fig. 2-3 Real part of the refractive index $R_e n_{\perp}$ as a function of angle θ between the wave vector k and magnetic field B.

f = 60 GHz. T_e = 600 eV.

(a) S = 1, (b) S = 2, (c) S = 3.

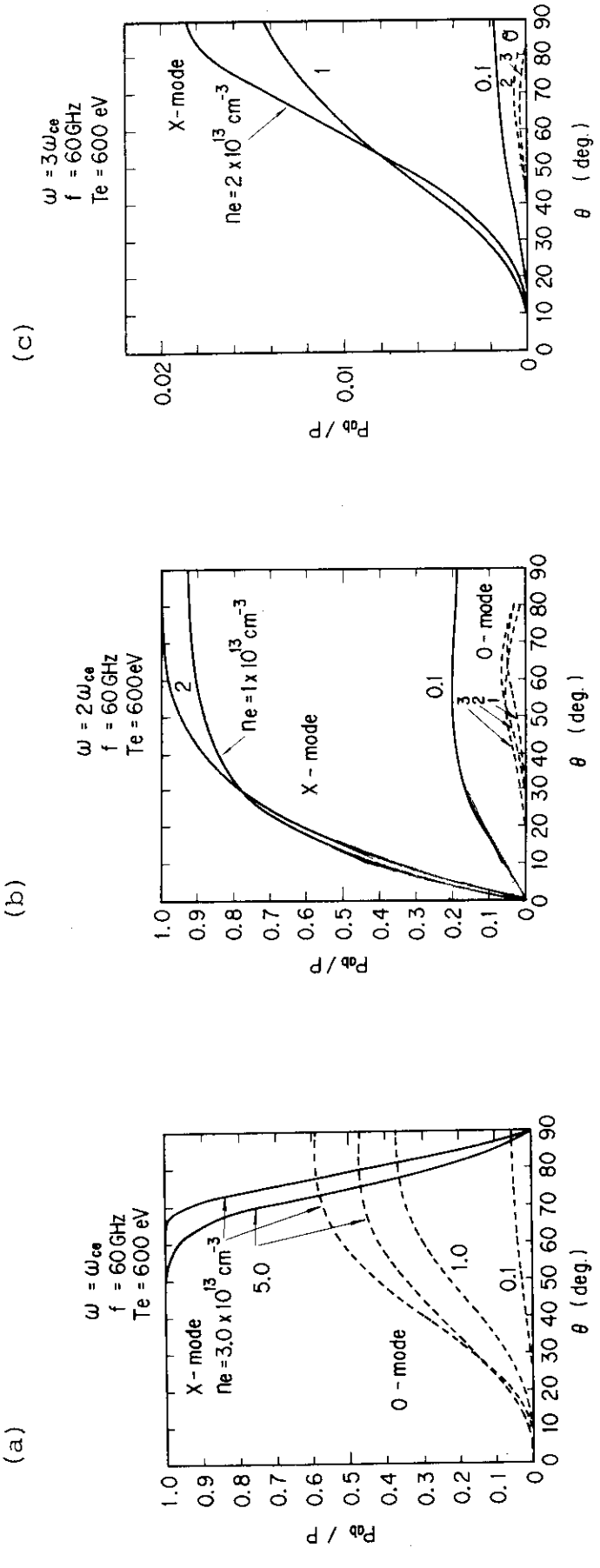

Fig. 2-4 Single path absorption rate P_{ab}/P at the ECR layer as a function of the angle θ.
(a) S = 1, (b) S = 2, (c) S = 3.

(S = 2). The maximum field of the JFT-2M tokamak is B = 1.5 T. Therefore we cannot employ the fundamental heating. But by injecting the 2nd harmonic X-mode nearly perpendiculadly, we can obtain a large single path absorption. Therefore local heating is posible in the JFT-2M tokamak.

5. The parameter dependence (n_e, T_e) of the P_{ab}/P is shown in Fig. 2-5. Here the launch angle is fixed to $\theta = 80°$ ($n_{/\!/} = 0.17$). We can expect $P_{ab}/P \geqq 90$ % at $n_e \geq 1 \times 10^{13}$ cm^{-3} and $T_e \geq 600$ eV. Such plasma parameters are easily obtained in the JFT-2M tokamak.
6. For the local heating, the launched microwave beam should have the gaussian-like profile (ex. circular TE_{11} mode) rather than the hollow profile (ex. circalar TE_{on} mode which is the output of the gyrotron). And linearly polarized wave should be launched perpendicularly to launch the pure plasma modes (X-mode or O-mode).

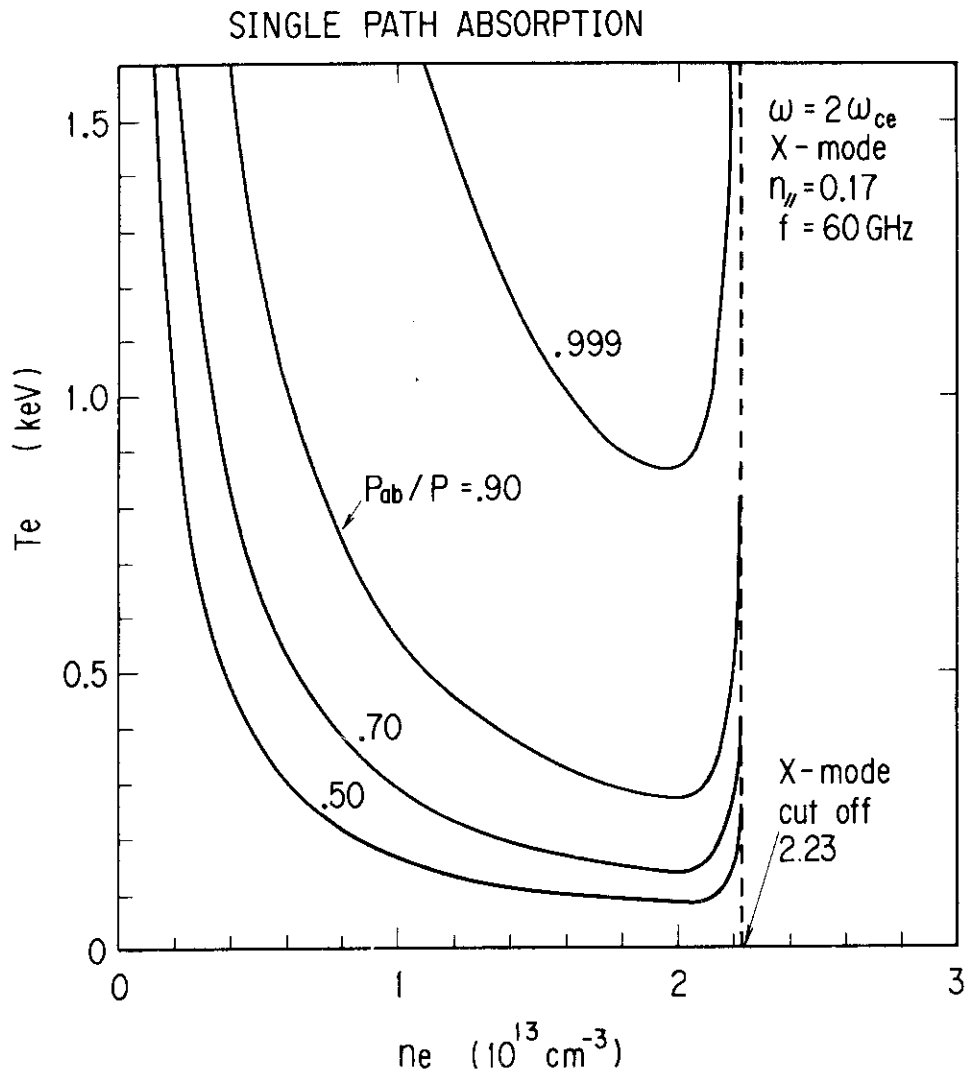

Fig. 2-5 Single path absorption rate of the X-mode $\frac{P_{ab}}{P}$ at the 2nd harmonic ECR layer as a function of the local density n_e and temperature T_e. $n_{/\!/} = 0.17$ ($\theta = 80°$). $f = 60$ GHz. Cutoff of the X-mode occurs at the density $n_c = 2.23 \times 10^{13}$ cm^{-3} (right hand cutoff density).

3. ECH System

3.1 RF Transmission System

3.1.1 General Design Concepts of the RF Transmission System

By the study in the previous chapter, the following requirements are imposed on the ECH system

1. RF frequency f = 60 GHz ($\omega = 2\omega_{ce}$)
2. Launch angle $\theta = 80°$ ($n_{/\!/} = 0.17$)
3. Gaussian-like beam profile
4. Pure mode (either X-mode or O-mode) should be launched
   → TE_{11} mode

The output mode of the 60 GHz gyrotron (Varian VGE-8060) is almost (~94 %) polarized in the circular TE_{02} mode. Therefore, to launch the TE_{11} mode, a conversion of the TE_{02} mode is necessary. The mode converters for this use are the key components of the rf transmission system.

From the point of view of the gyrotron operation, the gyrotron should be set apart from the tokamak machine to avoid the effect of the error field. Because a transverse magnetic field at the gyrotron cavity affects the oscillation. The transverse field should be less than ~40 gauss (< 0.02 % of the longitudinal magnetic field) at the cavity. Besides, in our case, there was no room to set the gyrotron tank around the JFT-2M tokamak machine. Therefore the gyrotron is set ~20 m apart from the tokamak machine. And the total length of the transmission line becomes ~33 m from the gyrotron window to the vacuum barrier window of the JFT-2M machine. Then, the loss in the transmission line becomes a severe problem.

To minimize the loss, an oversized waveguide and TE_{01} mode are chosen for the transmission. The oversized waveguide has low joule loss. Fundamental waveguide can not be used for such a high frequency. The loss in 30 m becomes ~85 % at 60 GHz. TE_{01} mode has the smallest joule loss in the circular waveguide, besides it has the lowest peak field which is preferable to avoid the break down in the waveguide.

In conclusion, the successive mode conversion as TE_{02} mode → TE_{01} mode → TE_{11} mode is necessary (Fig. 3-1). This scheme was first proposed in the ECH system of the Doublet III tokamak[10),11)].

Though the large diameter of the circular waveguide is preferable

to minimize the joule loss, a mode conversion loss which arises from a bending of the waveguide and from an imperfection of the waveguide becomes a severe problem as the diameter of the waveguide increases. Therefore, the diameter of the circular waveguide should be small enough to avoid the mode conversion to the modes which have a large joule loss.

(1) Joule Loss in the Circular Waveguide and the Minimization of the Loss

The loss in the waveguide is expressed by an attenuation coefficient α [m^{-1}]. The power of a mode is expressed as,

$$P(Z) = P(0)e^{-2\alpha Z} \quad [W] \ . \tag{3.1}$$

Here Z is a coordinate along the waveguide axis. Then the loss W per unit length is written as

$$W = -dP(Z)/dZ = 2\alpha P(Z) \quad [W \cdot m^{-1}] \ . \tag{3.2}$$

Usually $\alpha \ll 1$. The attenuation coefficient α due to the joule loss of the eigen mode in the straight circular waveguide is expressed as[13]

$$\alpha_{[mn]} = \frac{R}{\eta a}\left[\frac{m^2}{\chi^2_{[mn]} - m^2} + \nu^2_{[mn]}\right]\frac{1}{\sqrt{1-\nu^2_{[mn]}}} \ [m^{-1}] \ (TE_{mn} \text{ mode}) \tag{3.3}$$

$$\alpha_{(mn)} = \frac{R}{\eta a}\frac{1}{\sqrt{1-\nu^2_{(mn)}}} \ [m^{-1}] \ (TM_{mn} \text{ mode}) \ . \tag{3.4}$$

Here,

$R = \sqrt{\pi f \rho \mu_0} \approx 6.383 \times 10^{-2}$ $(f = 60$ GHz)

f : frequency 60×10^9 $[S^{-1}]$

ρ : resistivity of the wall surface 1.72×10^{-8} $[\Omega \cdot m]$

μ_0: permeability of vacuum $4\pi \times 10^{-7}$ $[H \cdot m^{-1}]$

$\eta = \sqrt{\frac{\mu_0}{\varepsilon_0}}$: characteristic impedance of the space 377 $[\Omega]$

a : radius of the circular waveguide [m]

$\chi_{[mn]}$: nth zero of the Bessel function J'_m

$\chi_{(mn)}$: nth zero of the Bessel function J_m

$\chi_{[01]} = \chi_{(11)} = 3.83$

$$\chi_{[02]} = \chi_{(12)} = 7.02$$

$$\chi_{[03]} = \chi_{(13)} = 10.2$$

$$\chi_{[04]} = \chi_{(14)} = 13.3$$

$$\chi_{[05]} = \chi_{(15)} = 16.5$$

$\nu_{mn} = \lambda/\lambda_{c,mn}$

λ_c: cutoff wavelength [m]

$$\lambda_{c[mn]} = \frac{2\pi a}{\chi_{[mn]}}, \quad \lambda_{c(mn)} = \frac{2\pi a}{\chi_{(mn)}} .$$

First, TE_{on} mode is considered (m = 0). Then,

$$\alpha_{[on]} = \frac{R}{\eta a} \nu^2_{[on]} \frac{1}{\sqrt{1 - \nu^2_{[on]}}} . \tag{3.5}$$

In the case of $\lambda^2 \ll a^2$

$$\nu^2_{[on]} = \left(\frac{\lambda}{\lambda_{c[on]}}\right)^2 = \frac{\chi^2_{[on]} \lambda^2}{4\pi^2 a^2} \ll 1 .$$

Then,

$$\alpha_{[on]} = \frac{\chi^2_{[on]} \sqrt{\pi f \rho \mu_0}}{4\pi^2 \eta a^3} \left(\frac{c}{f}\right)^2$$

$$= \frac{\chi^2_{[on]} \sqrt{f\rho \times 1 \times 10^{-7}}}{2\pi \eta a^3} \left(\frac{c}{f}\right)^2 \propto \frac{1}{a^3} \frac{1}{f^{3/2}} \chi^2_{[on]} . \tag{3.6}$$

Thus the attenuation coefficient of the TE_{on} mode scale as $a^{-3} f^{-3/2} \chi^2_{[on]}$, indicating that the loss is small in the case of large radius, high frequency and low mode number n. Therefore the loss is minimum for the TE_{01} mode. The ratio of the attenuation coefficients between TE_{on} modes for fixed radius and frequency, is the same as the ratio of $\chi^2_{[on]}$. The value of χ_{mn} is shown in Table 3-1[13]. For example,

$$\frac{\alpha_{[02]}}{\alpha_{[01]}} = \frac{\chi^2_{[02]}}{\chi^2_{[01]}} = \frac{(7.02)^2}{(3.83)^2} = 3.36.$$

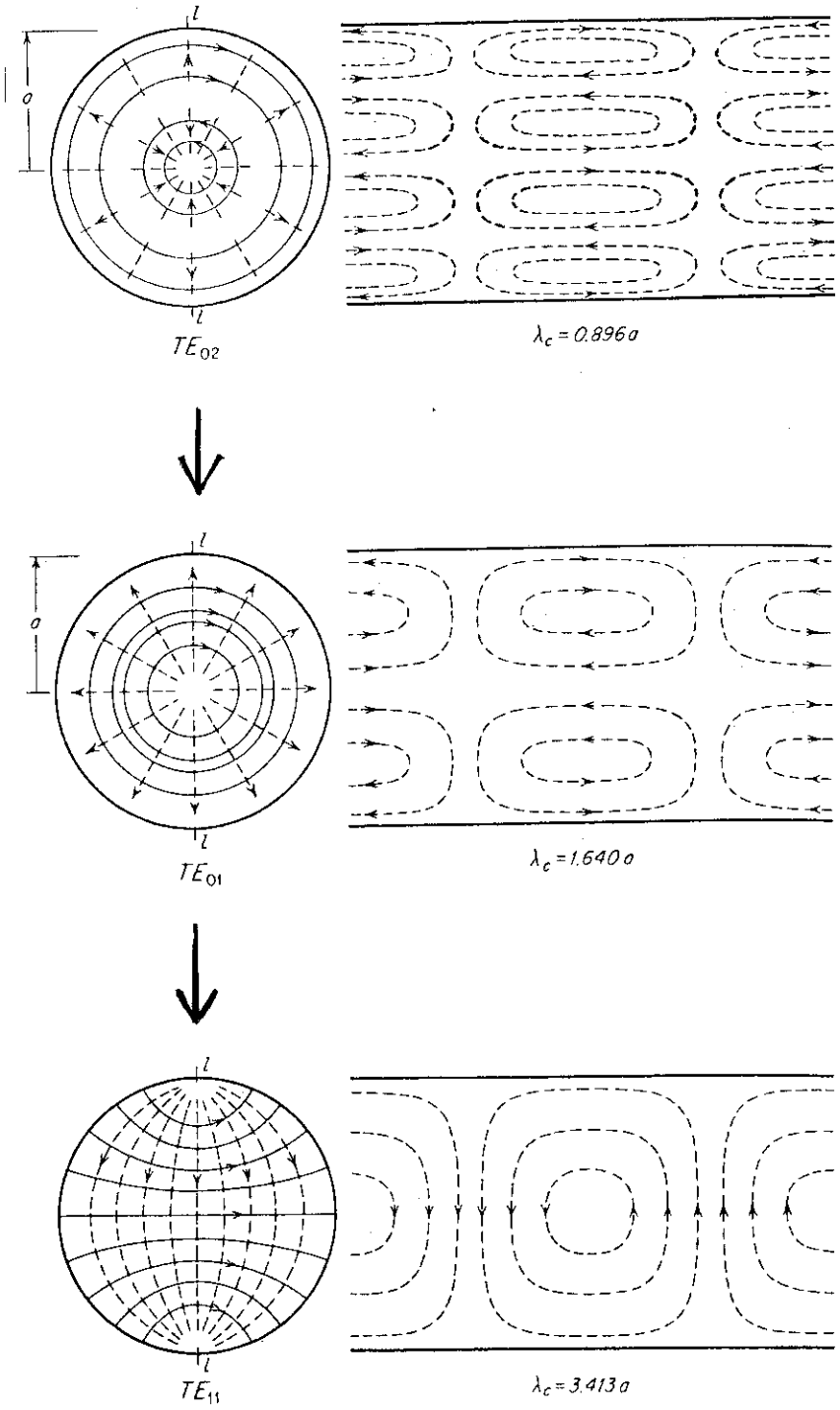

Fig. 3-1 Patterns of TE_{02}, TE_{01} and TE_{11} modes in a circular waveguide of radius a. λ_C is a cutoff wave length. Electric field is represented by solid line and magnetic field is represented by broken line. (Ginzton E.L., "Microwave Measurements", McGraw-Hill Book Co., Inc. (1957))

Table 3-1 χ_{mn} of the modes in the circular waveguide[13]. Eighty modes can propagate in the circular waveguide of radius a = 13.9 mm.

	モード mn	χ(mn) or χ[mn]		モード mn	χ(mn) or χ[mn]
1	TE 1-1	1.841184	(48	TM 1-4	13.323692
2	TM 0-1	2.404826	(49	TE 0-4	13.323692
3	TE 2-1	3.054237	50	TM 9-1	13.354300
(4	TM 1-1	3.831706	51	TM 6-2	13.589290
(5	TE 0-1	3.831706	52	TE 12-1	13.878843
6	TE 3-1	4.201189	53	TE 5-3	13.987189
7	TM 2-1	5.135622	54	TE 8-2	14.115519
8	TE 4-1	5.317553	55	TM 4-3	14.372537
9	TE 1-2	5.331443	56	TM 10-1	14.475501
10	TM 0-2	5.520078	57	TE 3-4	14.585848
11	TM 3-1	6.380162	58	TM 2-4	14.795952
12	TE 5-1	6.415616	59	TM 7-2	14.821269
13	TE 2-2	6.706133	60	TE 1-5	14.863589
(14	TM 1-2	7.015587	61	TE 13-1	14.928374
(15	TE 0-2	7.015587	62	TM 0-5	14.930918
16	TE 6-1	7.501266	63	TE 6-3	15.268181
17	TM 4-1	7.588342	64	TE 9-2	15.286738
18	TE 3-2	8.015237	65	TM 11-1	15.589848
19	TM 2-2	8.417244	66	TM 5-3	15.700174
20	TE 1-3	8.536316	67	TE 4-4	15.964107
21	TE 7-1	8.577836	68	TE 14-1	15.975439
22	TM 0-3	8.653728	69	TM 8-2	16.037774
23	TM 5-1	8.771484	70	TM 3-4	16.223466
24	TE 4-2	9.282396	71	TE 2-5	16.347522
25	TE 8-1	9.647422	72	TE 10-2	16.447853
26	TM 3-2	9.761023	(73	TM 1-5	16.470630
27	TM 6-1	9.936110	(74	TE 0-5	16.470630
28	TE 2-3	9.969468	75	TE 7-3	16.529366
(29	TM 1-3	10.173468	76	TM 12-1	16.698250
(30	TE 0-3	10.173468	77	TM 6-3	17.003820
31	TE 5-2	10.519861	78	TE 15-1	17.020323
32	TE 9-1	10.711434	79	TM 9-2	17.241220
33	TM 4-2	11.064709	80	TE 5-4	17.312842
34	TM 7-1	11.086370	81	TE 11-2	17.600267
35	TE 3-3	11.345924	82	TM 4-4	17.615966
36	TM 2-3	11.619841	83	TE 8-3	17.774012
37	TE 1-4	11.706005	84	TE 3-5	17.788748
38	TM 6-2	11.734936	85	TM 13-1	17.801435
39	TE 10-1	11.770877	86	TM 2-5	17.959819
40	TM 0-4	11.791534	87	TE 1-6	18.015528
41	TM 8-1	12.225092	88	TE 16-1	18.063261
42	TM 5-2	12.338604	89	TM 0-6	18.071064
43	TE 4-3	12.681908	90	TM 7-3	18.287583
44	TE 11-1	12.826491	91	TM 10-2	18.433464
45	TE 7-2	12.932386	92	TE 6-4	18.637443
46	TM 3-3	13.015201	93	TE 12-2	18.745091
47	TE 2-4	13.170371	94	TM 14-1	18.899998

propagate

TE_{01}~ TE_{05} (5 modes)
TE_{11}~ TE_{15} (5 ")
TE_{21}~ TE_{25} (5 ")
TE_{31}~ TE_{34} (4 ")
TE_{41}~ TE_{44} (4 ")
TE_{51}~ TE_{54} (4 ")
TE_{61}~ TE_{63} (3 ")
TE_{71}~ TE_{73} (3 ")
TE_{81}~ TE_{82} (2 ")
TE_{91}~ TE_{92} (2 ")
$TE_{10\,1}$~ $TE_{10\,2}$ (2 ")

$TE_{11\,1}$
$TE_{12\,1}$
$TE_{13\,1}$
$TE_{14\,1}$
$TE_{15\,1}$

number of TE_{mn} modes	44
number of TM_{mn} modes	46
total	80

The attenuation per unit length in dB unit is expressed as

$$10 \log_{10} \frac{P_o e^{-2\alpha}}{P_o} = -20 \alpha \log_{10} e = -8.69 \alpha \ . \qquad (3.7)$$

A fraction of the joule loss is obtained from (3.2) as

$$\frac{P_{loss}}{P_o} = \frac{P_o - P_{(Z)}}{P_o} = 1 - e^{-2\alpha Z} \qquad (3.8)$$

Loss of the TE_{01} mode in the fundamental circular wave guide (WRC243C14) of the radius a = 4.17 mm is calculated from (3.5) and (3.8)

$$\lambda_{c[01]} = \frac{2\pi a}{\chi_{[01]}} = 6.84 \times 10^{-3} \ [m]$$

$$\nu_{[01]} = \frac{\lambda}{\lambda_{c[01]}} = 0.73$$

$$\alpha_{[01]} = 3.17 \times 10^{-2} \ [m^{-1}]$$

$$\frac{P_{loss}}{P_o} = 85 \ [\%] \text{ in } 30 \text{ m.}$$

Thus the fundamental waveguide has a too much loss. For the lager radius of a = 13.9 mm

$$\lambda_{c[01]} = 22.8 \times 10^{-3} \ [m]$$

$$\nu_{[01]} = 0.22$$

$$\alpha_{[01]} = 6.0 \times 10^{-4} \ [m^{-1}]$$

$$\frac{P_{loss}}{P_o} = 3.5 \ [\%] \text{ in } 30 \text{ m.}$$

$TM_{(mn)}$ mode has larger loss than $TE_{[mn]}$ mode. The attenuation coefficient in the large radius scales using (3.4) as

$$\alpha_{(mn)} \approx \frac{R}{\eta a} \propto a^{-1} \sqrt{f} \quad (\text{for } \lambda^2 \ll a^2).$$

The attenuation coefficients of the various modes of 60 GHz in the waveguide of radius a = 13.9 mm obtained using (3.3), (3.4) are given in Table 3-2. The higher modes have even larger losses than these modes. It is seen that the joule loss is suppressed to less than 4 % in the circular waveguide of radius a = 13.9 mm (WRC727D14) by using TE_{01} mode.

Since the TM_{11} mode degenerates with the TE_{01} mode ($\chi_{(11)} = \chi_{[01]}$), the azimuthal perturbation (bending) of the TE_{01} mode causes easily a generation of TM_{11} mode which has a large loss as given in the Table 3-2. Therefore the bending of the straight waveguide should be strictly prohibited.

(2) Field Strength in the Waveguide and Avoidance of the Breakdown

In this section, the maximum electric field strength in the waveguide is calculated. And the critical power at which the field strength exceeds the break down voltage of the air 2.9×10^4 V/cm is obtained.

The azimuthal component of the electric field of the TE_{mn} mode propagating in the circular waveguide is expressed as[13]

$$E_\phi (r,z) = V_{[mn]}(Z) \sqrt{\frac{\varepsilon_m}{\pi}} \frac{\chi_{[mn]}}{\sqrt{\chi^2_{[mn]} - m^2}} \frac{J'_m (u_{[mn]} r)}{a\, J_m (\chi_{[mn]})} \begin{matrix} \cos m\phi \\ \sin m\phi \end{matrix} . \tag{3.9}$$

Only, the forward wave is assumed to exist. Then,

$$V_{[mn]} (Z) = V_{o[mn]}\, e^{-i\beta_{[mn]} Z} . \tag{3.10}$$

Here

$V_{o[mn]}$: Voltage of the TE_{mn} mode

Z: coordinate along the waveguide axis

$$\varepsilon_m = \begin{cases} 1 & (m = o) \\ 2 & (m \neq o) \end{cases}$$

	χ_{mn}	λ_c (mm)	ν_{mn}	α_{mn} (m^{-1})	W/P_0(30m) att. (%)	(dB/m)
TE_{01}	3.83	22.8	.219	6.0×10^{-4}	3.5	-5.2×10^{-3}
TE_{02}	7.02	12.4	.403	2.2×10^{-3}	12	-1.9×10^{-2}
TE_{03}	10.2	8.56	.584	5.1×10^{-3}	26	-4.4×10^{-2}
TE_{11}	1.84	47.5	.105	5.3×10^{-3}	27	-4.6×10^{-2}
TE_{12}	5.33	16.4	.305	1.7×10^{-3}	9.7	-1.5×10^{-2}
TM_{11}	3.83	22.8	.219	1.2×10^{-2}	51	-1.0×10^{-1}

Table 3-2 Joule losses of 60 GHz modes in circular waveguide of radius a = 13.9 mm.

	χ_{mn}	λ_c (mm)	ν_{mn}	$\zeta\sqrt{1-\nu_{mn}^2}$	$\lvert V_{0i}\rvert$ (V)	ε_m	u_{mn}	m, $J_m(\chi)$	$J_{m,max}$	$\lvert E_{\phi max}\rvert$ (kV/cm)
TE_{01}	3.83	22.8	.219	2.59×10^{-3}	1.24×10^{4}	1	276	0 -.403	.582	7.28
TE_{02}	7.02	12.4	.403	2.43×10^{-3}	1.28×10^{4}	1	505	0 .300	.582	10.0
TE_{03}	10.2	8.56	.584	2.15×10^{-3}	1.36×10^{4}	1	734	0 -.244	.582	13.2
TE_{04}	13.3	6.56	.762	1.72×10^{-3}	1.52×10^{4}	1	957	0 .212	.582	17.0
TE_{05}	16.5	5.30	.943	$.883\times10^{-3}$	2.13×10^{4}	1	1190	0 -.173	.582	29.0
TE_{06}	-	-	cutoff	-	-	1	-	-	-	-

Table 3-3 Maximum field $E_{\phi\ max}$ in the circular waveguide of radius a = 13.9 mm. The power is 200 kW.

$$u_{[mn]} = \frac{\chi_{[mn]}}{a}$$

$\beta_{[mn]}$: wave number of the TE_{mn} mode

The power transferred in the z direction is expressed as,

$$P_{[mn]} = \zeta \sqrt{1 - \nu^2_{[mn]}} \, |\bar{V}_{[mn]}|^2 \tag{3.11}$$

Here,

$$\zeta = \sqrt{\frac{\sigma + i\omega\varepsilon}{i\omega\mu}} = \frac{1}{\eta} = \frac{1}{377} \text{ in free space}$$

$$\bar{V}_{[mn]} = \frac{V_{[mn]}}{\sqrt{2}} \quad \text{(average in time)} .$$

From the above two equations (3.10), (3.11), the relation between the maximum field $|E_{\phi,max}|$ and power $P_{[mn]}$ is obtained as

$$|E_{\phi,max}| = \sqrt{\frac{2P_{[mn]}}{\zeta\sqrt{1 - \nu^2_{[mn]}}}} \sqrt{\frac{\varepsilon_m}{\pi}} \frac{\chi_{[mn]}}{\sqrt{\chi^2_{[mn]} - m^2}}$$

$$\frac{|J'_m(u_{[mn]}r)_{max}|}{a|J_m(\chi_{[mn]})|} \propto a^{-1}\sqrt{P} \quad [V/m] \tag{3.12}$$

or

$$P_{[mn]} = \frac{\zeta}{2}\sqrt{1 - \nu^2_{[mn]}} \left(|E_{\phi,max}| \sqrt{\frac{\pi}{\varepsilon_m}} \frac{\sqrt{\chi^2_{[mn]} - m^2}}{\chi_{[mn]}} \right.$$

$$\left. \frac{a|J_m(\chi_{[mn]})|}{J_m(u_{[mn]}r)_{max}} \right)^2 \quad [W] \tag{3.13}$$

The waveguide can transfer the wave which has the smaller wavelength than the cutoff wavelength λ_c.

$$\lambda < \lambda_c = \frac{2\pi a}{\chi_{mn}} \quad (\text{or } \nu_{mn}^2 < 1) \tag{3.14}$$

Thus there is an upper limit of χ_{mn}.

$$\chi_{mn} < \frac{2\pi a}{\lambda} \tag{3.15}$$

For f = 60 GHz, a = 13.9 mm, the maximum value is $\chi_{mn,max} = 17.48$. The values of χ_{mn}, of the various modes are given in Table 3-1. One finds that eightly modes can propagate in the circular waveguide of radius a = 13.9 mm (WRC727D14). Five TE_{on} modes ($TE_{01} \sim TE_{05}$) can propagate. The calculated field intensity of these modes using (3.12), is given in Table 3-3. In the calculation the power is set to 200 kW. The peak field is the lowest (7.28 kV/cm) for the TE_{01} mode of power 200 kW. The peak field becomes larger as the mode number n increases. The peak field of the TE_{05} mode of power 200 kW is equal to the break down voltage of the air (29 kV/cm). Thus the high mn modes are dangerous for the break down. These high TE_{on} modes are generated by the radial perturbation of the TE_{01} or TE_{02} mode. But by carefully designing the $TE_{02} \rightarrow TE_{01}$ mode converter and the transmission line, the generation of the high n mode is suppressed sufficiently.

A critical power transferred in the waveguide of radius a is obtained from (3.13) by setting $E_{\phi,max}$ as the break down electric field of the air (29 kV/cm). For TE_{01} mode in the waveguide of radius a = 13.9 mm, the critical power is 3.1 MW. Therefore, in our case, the maximum transferred power (200 kW) is $\sim \frac{1}{16}$ of the critical power. However, this calculation assumes an ideal condition, but actually the breakdown voltage at the material surface (waveguide surface, window surface) may be lower. Therefore the insulation gas (SF_6 of pressure < 1.3 atm) is used in our system. The critical power is raised by a factor two by this insulation. Actually, without the gas, we couldn't have carried out the experiment in the last year, because the break down occured frequently in the waveguide without the insulation gas.

The power density in the waveguide is 33 kW/cm^2 when 200 kW is transferred. The capability of transmission of the high power density is one of the merits of ECH.

(3) Mode Conversion at the Waveguide Bend

In this section, mode conversion of TE_{on} mode at the bend (the radius of curvature R) waveguide is investigated. The following notation are taken for the amplitudes of each forward modes.

a_0 : TE_{01}

a_1 : TM_{11}

a_s : TE_{1s}

Then the transfer equation is written as,[13]

$$\frac{da_0}{dZ} = -i\,\beta_0\,a_0 - i\,c\,a_1 - i\sum_s c_s\,a_s$$

$$\frac{da_1}{dZ} = -i\,c\,a_0 - i\,\beta_1\,a_1 \qquad (3.16)$$

$$\frac{da_s}{dZ} = -i\,c_s\,a_0 - i\,\beta_s\,a_s\ .$$

Here, β is the propagation constant, c and c_s are the coupling constants expressed as

$$c = c^{+}_{[01](11)} = \frac{ka}{\sqrt{2}\,\chi_{[01]}}\,\frac{1}{R} = 1.16\,\frac{a}{\lambda R}\ ,$$

$$c_s = c^{+}_{[01][1s]}.$$

The boundary conditions are

$$a_0\ (z = 0) = 1,$$
$$a_1\ (z = 0) = 0,$$
$$a_s\ (z = 0) = 0.$$

The (3.16) is solved by the perturbation method. The approximate solution in the first order in $\frac{c_s}{\beta_s - \beta_0}$ is written as,

$$a_0(z) = e^{-i\beta_0 z}\cos cz$$
$$a_1(z) = -i\,e^{-i\beta_0 z}\sin cz$$

$$a_s(z) = \frac{c_s}{\beta_s - \beta_0} \{e^{-i\beta_s z} - e^{-i\beta_0 z} \cos cz\} \tag{3.17}$$

The amplitude of TE_{01} mode becomes zero at

$$cz = \frac{\pi}{2} + n\pi \ .$$

Therefore the complete mode conversion of TE_{01} mode to TM_{11} mode occurs at

$$z_c = 1.35 \frac{\lambda R}{a} (1 + 2n) \quad (n = 0,1,2,\cdots) \ . \tag{3.18}$$

A critical angle θ_c is defined by

$$\theta_c = 1.35 \frac{\lambda}{a} \quad (1 + 2n). \tag{3.19}$$

For the 60 GHz wave propagating in the circular waveguide of radius a = 13.9 mm, the critical angle θ_c is calculated as follows.

n = 0	θ_c = 0.486	[rad.]	= 27.8	[deg.]
n = 1	θ_c = 1.46	[rad.]	= 83.4	[deg.]
n = 2	θ_c = 2.43	[rad.]	= 139	[deg.]

For a 90° bend $z = \frac{\pi}{2} R$ and the amplitude of the TE_{01} mode a_0 is calculated as

$$|a_0(z)| = \cos \frac{\pi}{2} \ RC = \cos \frac{\pi}{2} \times 1.16 \frac{a}{\lambda} = 0.35 \ .$$

Therefore ~88 % of the TE_{01} mode is converted to the other modes in the 90° bend. To decrease the mode conversion, the degeneration of the TE_{01} mode and TM_{11} mode has to be resolved. For that purpose, the corrugated bends are used in our system. The corrugated bends are described in Sec. 3.1.3 (2).

3.1.2 Constitution of the RF Transmission System

A schematic diagram of the rf transmission system of the JEF-2M tokamak is shown in Fig. 3-2. A 60 GHz gyrotorn produces TE_{02} mode in circular waveguide of diameter 63.5 mm (2.5 inch). The rf frequency and general power is detected at the sampler just above the gyrotron. The break down in the gyrotron is detected by the arc detecter in the sampler. The unintensional modes trapped between the raised cosine taper (63.5 mm - 27.8 mm) and the up-taper in the gyrotron are filtered out by a mode filter which is water cooled. The forward power and reflected power are measured by a TE_{02} mode directional coupler.

$TE_{02} \rightarrow TE_{01}$ mode conversion occurs at a TE_{02} - TE_{01} mode converter. TE_{01} mode is transmitted to the tokamak machine through corrugated 90° bends and straight waveguides. Arc detecters are placed in between. Going through the DC break and a raised cosine taper (27.8 mm → 63.5 mm), the TE_{01} mode enters in the vacuum duct through a vacuum window. Then the waveguide is tapered down to 19.1 mm. Finally, by a TE_{01} - TE_{11} mode converter the TE_{01} mode is converted into TE_{11} mode and launched from a conical horn antenna.

Water load with an up taper to measure the rf power can be connected either before the vacuum window of the machine (point E) or after the directional coupler above the gyrotron (point D).

The various diameter changes are introduced because the mode converters and the corrugated waveguide bends can be made short only at small diameter. Whereas it is desirable to increase the diameter at the vacuum window to keep the power density and field low (3.2 kV/cm).

SF_6 gas is used for the insulation to avoid the breakdown in the transmission system. It was found that SF_6 gas is indispensable to avoid the breakdown in the waveguide.

3.1.3 High Power Overmoded Microwave Transmission Components

(1) Two Kinds of the Mode Converters ($TE_{02} \rightarrow TE_{01}$, $TE_{01} \rightarrow TE_{11}$)

The mode converters are the most important components in the transmission system. We use the mode converters which have periodical perturbations in the guide wall[10)~12),14)]. The wave number of the perturbation is equal to the difference of the wave number of the input mode and desired output mode. Thus the wave number k of the perturbation is written as

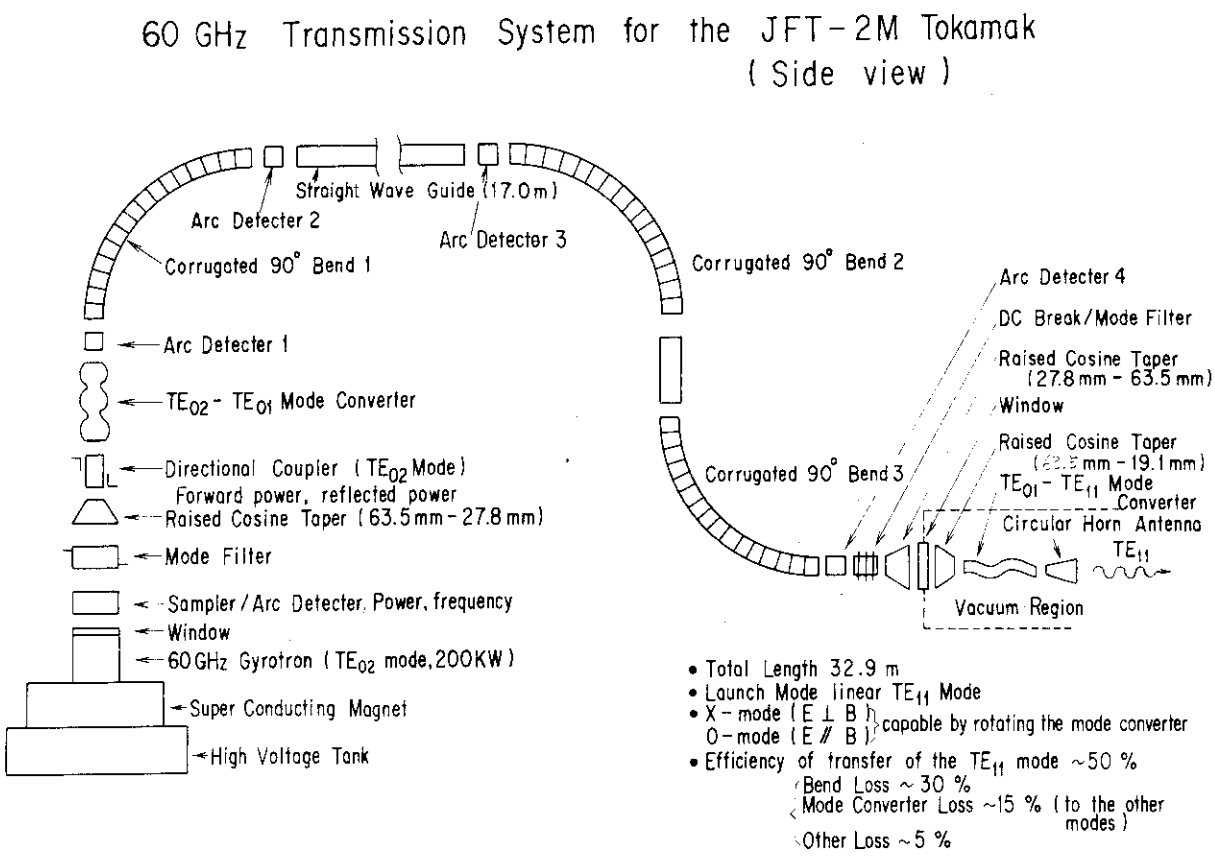

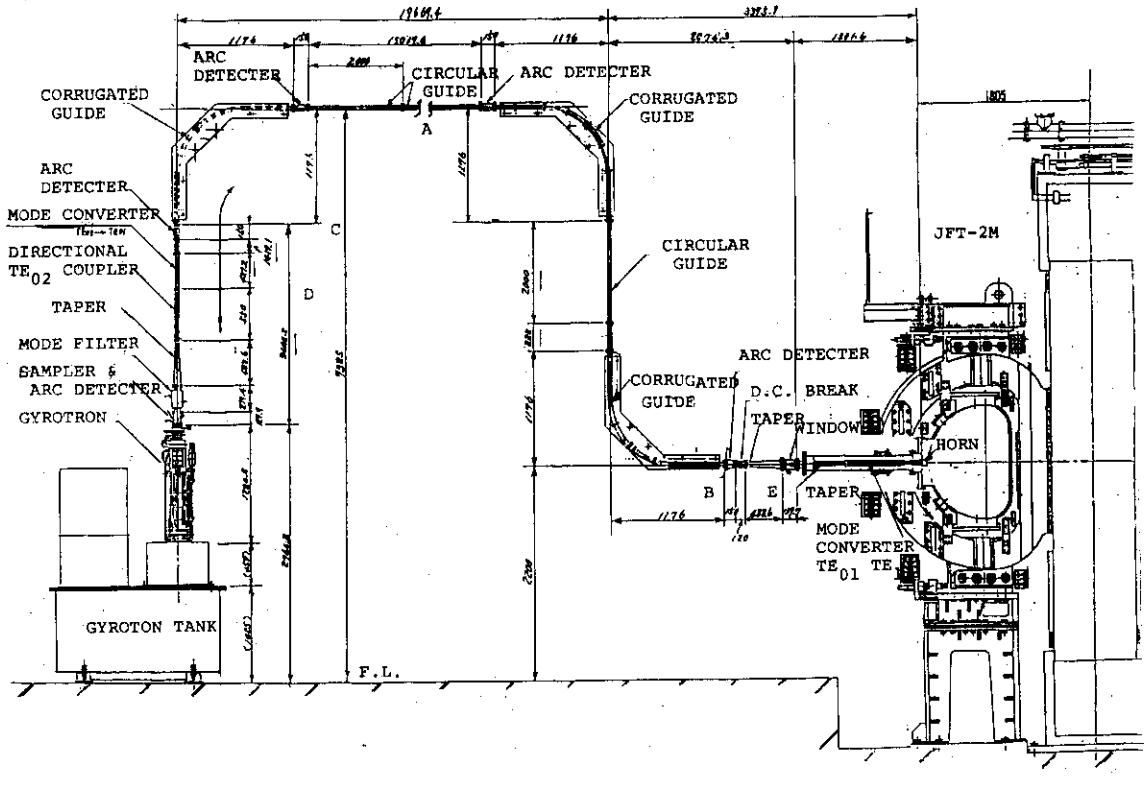

Fig. 3-2 60 GHz gyrotron and rf transmission system of the JFT-2M ECH system.

$$k = \frac{2\pi}{\lambda} = |k_{mn} - k_{m'n'}| \tag{3.20}$$

where

λ : wave length of the perturbation

k_{mn} : wave number of the input mode [mn]

$k_{m'n'}$: wave number of the output mode [m'n'].

The forward wave complex amplitude A_{mn} and backward wave complex amplitude B_{mn} at the coordinate Z are obtained from the "generalized telegraphist's equations" which are the ordinary simultaneous complex equations such as

$$\begin{aligned} \frac{dA_{mn}}{dZ} &= -i \sum_{\substack{mn \\ m'n'}} \left[K_{mn}^{+m'n'} A_{m'n'} + K_{mn}^{-m'n'} B_{m'n'} \right] \\ \frac{dB_{mn}}{dZ} &= i \sum_{\substack{mn \\ m'n'}} \left[K_{mn}^{-m'n'} A_{m'n'} + K_{mn}^{+m'n'} B_{m'n'} \right] \end{aligned} \tag{3.21}$$

where $K^{\pm}$ represent the coupling coefficients. We developed a computer code to solve (3.21) and optimized the shape (period and depth of the perturbation) of the mode converters[14]. We found that the backward power ($\propto B_{mn}^2$) is negligibly smaller (a several orders) than the forward power. The results of the calculations are shown in Fig. 3-3, 4. Fig. 3-3 shows the length dependence of the conversion fraction f(%). The mode conversion and reconversion appears one after another. And the power to the parasitic modes changes as the length. Therefore, an optimum length of the converter exists. TE_{12} mode is strongly excited in the $TE_{01} \rightarrow TE_{11}$ mode converter, and at the optimum length, the power of the TE_{12} mode is almost equal to the power of the unconverted TE_{01} mode (~ 4 %). Figure 3-4(a), (b) shows the λ dependence of the conversion fraction f. Around the optimum λ, f does not change much by the change within one wavelevgth (5 mm for 60 GHz) of the wave. Figure 3-4(c) (d) shows the dependence of the perturbation amplitude δ ($\delta \equiv \frac{\Delta a}{a}$, a: unperturbed radius) to f and the optimum length Z_{max}. As δ becomes large, the optimum length becomes short, but the conversion to the desired mode decreases and conversion to the undesired parasitic modes increases. Therefore, the length of the converters can not be made too short by increasing δ. Figure

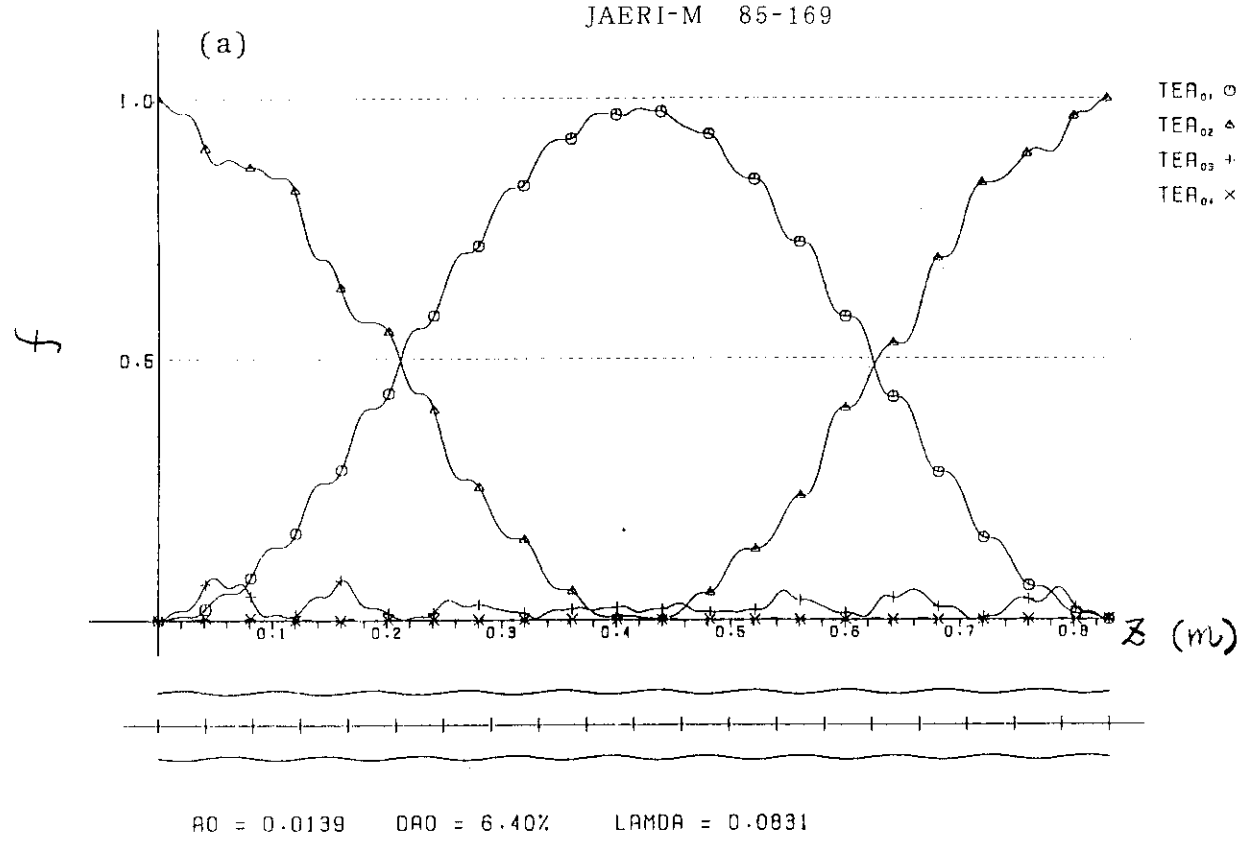

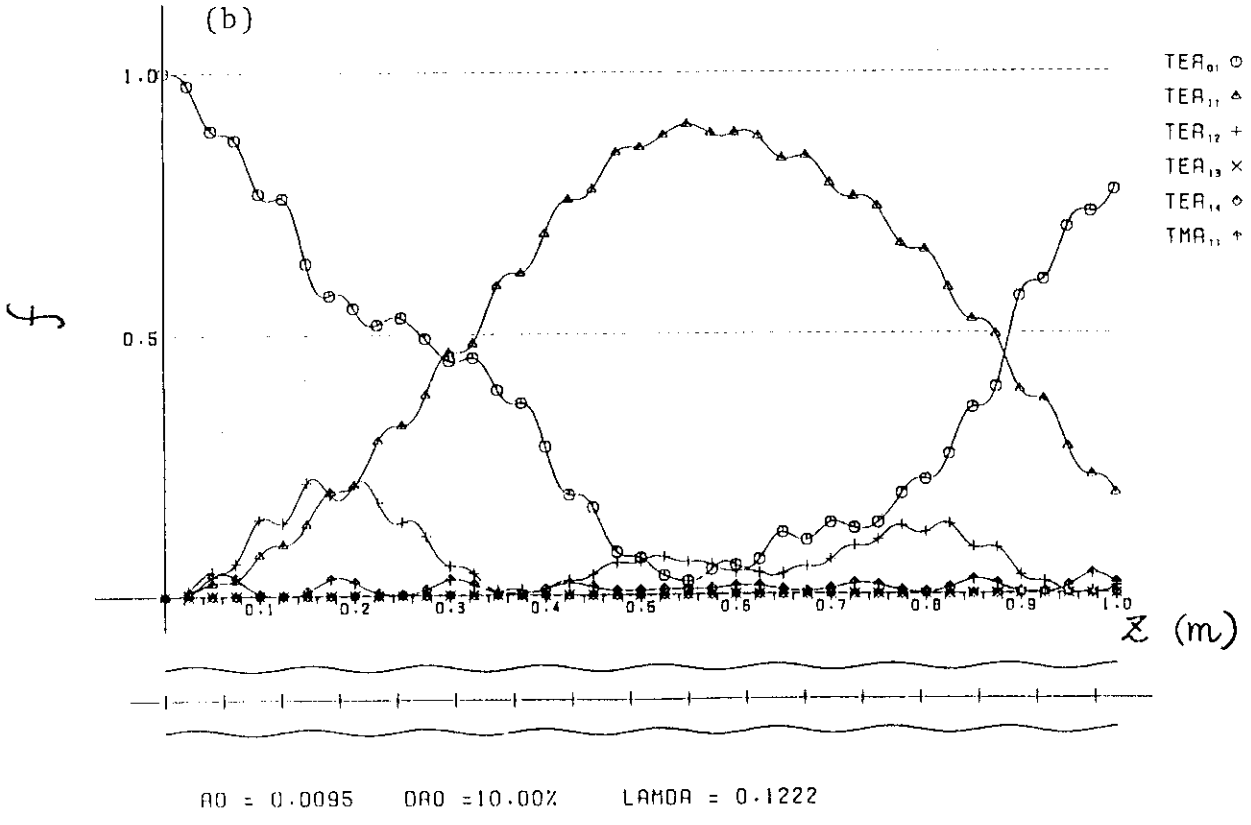

Fig. 3-3 Conversion fraction (normalized wave power) f as a function of the length Z.

(a) $TE_{02} \rightarrow TE_{01}$ mode converter

(b) $TE_{01} \rightarrow TE_{11}$ mode converter

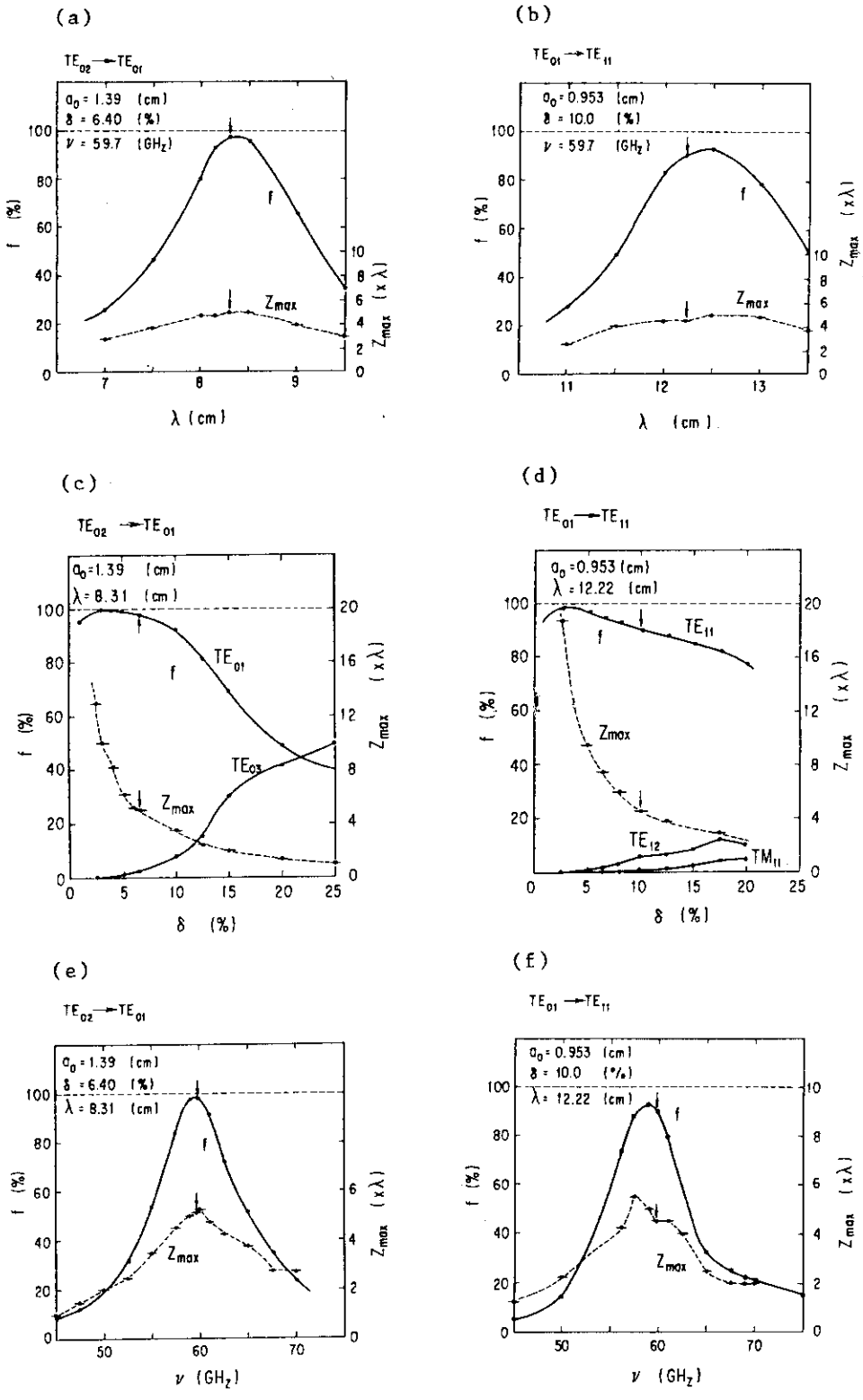

Fig. 3-4 λ dependence of the conversion fraction f of the
(a) $TE_{02} \rightarrow TE_{01}$ mode converter and
(b) $TE_{01} \rightarrow TE_{11}$ mode converter.
Conversion fraction f and optimum length as functions of the perturbation amplitude δ of the
(c) $TE_{02} \rightarrow TE_{01}$ mode converter and
(d) $TE_{01} \rightarrow TE_{11}$ mode converter.
Frequency characteristics of f of the
(e) $TE_{02} \rightarrow TE_{01}$ mode converter and
(f) $TE_{01} \rightarrow TE_{11}$ mode converter

(a) $TE_{02} \rightarrow TE_{01}$ Mode Converter

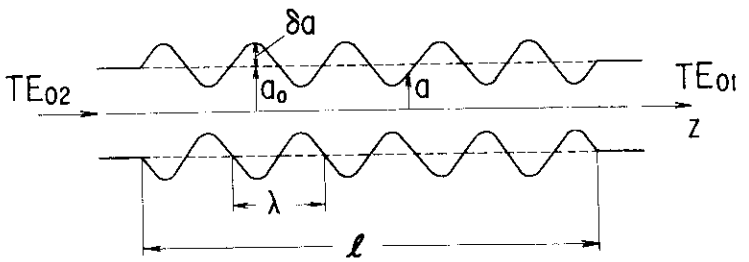

Perturbation Function :

$$a(z) = a_0(1+\delta \sin(\frac{2\pi z}{\lambda})),\ \delta = \delta a/a_0$$

Dimension :

$a_0 = 13.9$ mm, $\delta = 6.4\%$, $\lambda = 85$ mm,

$\ell = 5\lambda$. $\left(k = \frac{2\pi}{\lambda} \approx \left|\frac{2\pi}{\lambda_{02}} - \frac{2\pi}{\lambda_{01}}\right|\right)$

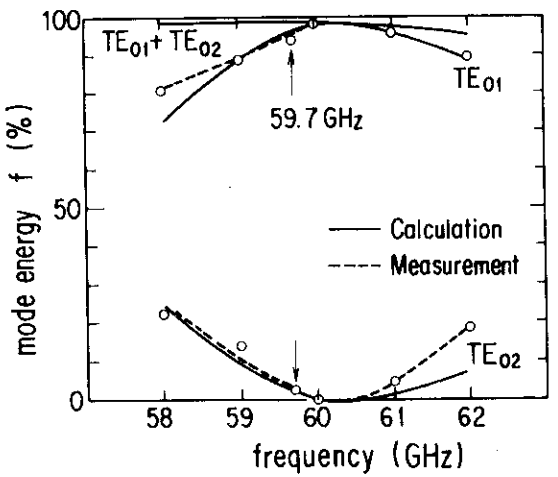

$f_{meas.} = 96\%$ (59.7 GHz)

$f_{calc.} = 98\%$ (59.7 GHz)

Reflection < -47 dB

(b) $TE_{01} \rightarrow TE_{11}$ Mode Converter

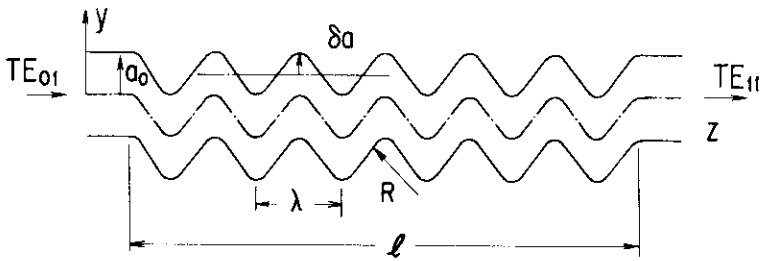

Perturbation Function :

$$y(z) = a_0(-1/2 + \delta \cos(\frac{2\pi z}{\lambda})),\ \delta = \delta a/a_0,$$

$$R(z) = \left|\frac{(1+y'^2)^{1.5}}{y''}\right|$$

Dimension :

$a_0 = 9.53$mm, $\delta = 8.6\%$, $\lambda = 125$ mm,

$\ell = 6\lambda$ $\left(k = \frac{2\pi}{\lambda} \approx \left|\frac{2\pi}{\lambda_{01}} - \frac{2\pi}{\lambda_{11}}\right|\right)$

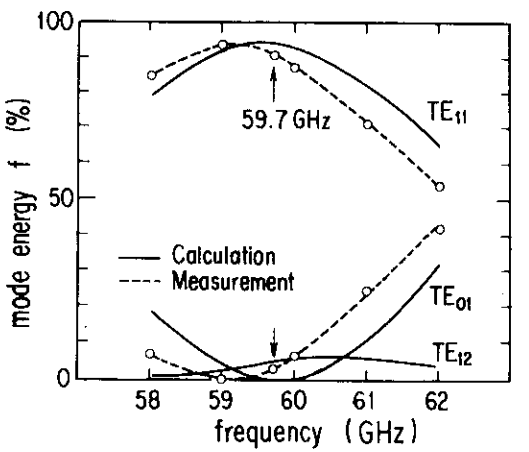

$f_{meas.} = 91\%$ (59.7 GHz)

$f_{calc.} = 94\%$ (59.7 GHz)

Refletion < -47 dB

Fig. 3-5 Shape of the mode converters, perturbation function and comparison of the calculation and measurement.

3-4(e)(f) shows the frequency dependence of f. These mode converters have a frequency band width of a few GHz.

The shape and dimension of the converters used in our system are given in Fig. 3-5(a)(b). The $TE_{02} \rightarrow TE_{01}$ converter has a dumbbell shape, and has a radial perturbation of a sine curve which decreases the radial mode number from 2 to 1. Whereas the $TE_{01} \rightarrow TE_{11}$ converter has a meander shape, and has an azimuthal perturbation of a cosine curve which increases the azimuthal mode number from 0 to 1.

The conversion rate f of the converters was measured (the circuit is shown in Fig. 3-6). The results are shown in Fig. 3-5(a)(b). We found that the measured conversion fraction f is in a good agreement with the calculation. The obtained results are summerized in Table 3-4.

(2) Corrugated 90° Bends

The bends which have periodic annular corrugation in the wall of the guides are used to avoid the undesired mode conversion of TE_{01} mode to TM_{11} mode. These corrugations affect the TM_{1n} modes which have degeneracy with TE_{on} modes, and resolve the degenracy. Therefore the mode conversion loss is reduced.

Dimendion of the bend is given in Fig. 3-7. Three bends are used. The total loss is quite large as 31.6 %. Improvement is now underway.

(3) Raised Casine Tapers

An overmoded linear taper needs a long length to suppress an unitentional mode conversion for the transmission of the rf wave. Therefore the raised cosine tapers are used. For the transmission of the TE_{01} mode, TE_{on} modes (especially TE_{02} mode) have to be suppressed. The shape of the taper is obtained from the following equations[13].

$$\ell n \frac{R}{R_1} = \left(\frac{\rho}{\rho_1} - \frac{1}{2\pi} \sin 2\pi \frac{\rho}{\rho_1} \right) \ell n \frac{R_2}{R_1}$$

R : radius of a taper at the axial coordinate Z.

R_1 : radius of one end of a taper

R_2 : radius of the another end of a taper

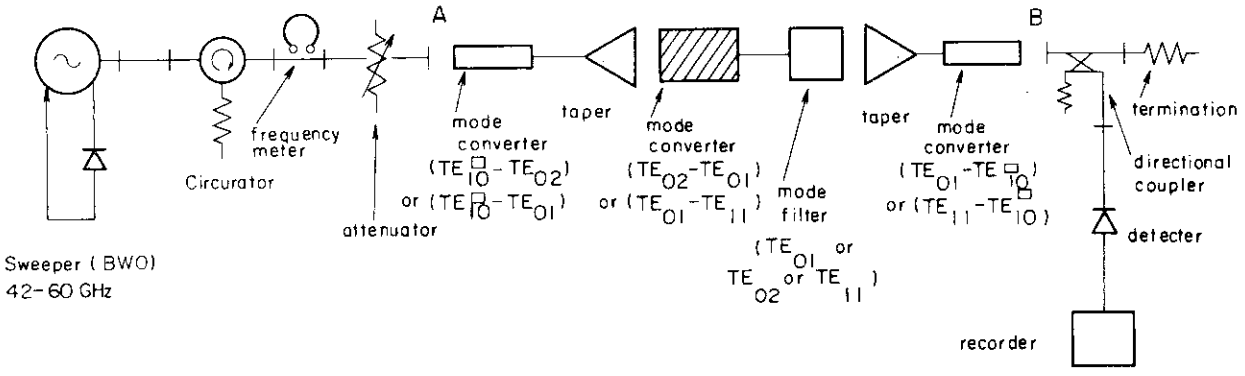

Fig. 3-6 Microwave circuits for the measurement of conversion fraction and loss of the mode converters.

Table 3-4 Results of the measurements of the characteristics of the mode converters.

	conversion fraction f	reflected power
$TE_{02} \rightarrow TE_{01}$	TE_{01} 96.2 % ± 3 % (59.7 GHz)	<-47dB (VSWR < 1.01)
$TE_{01} \rightarrow TE_{11}$	TE_{11} 90.5 % ± 3 % (59.7 GHz) TE_{01} 3.2 %	<-47dB (VSWR < 1.01)

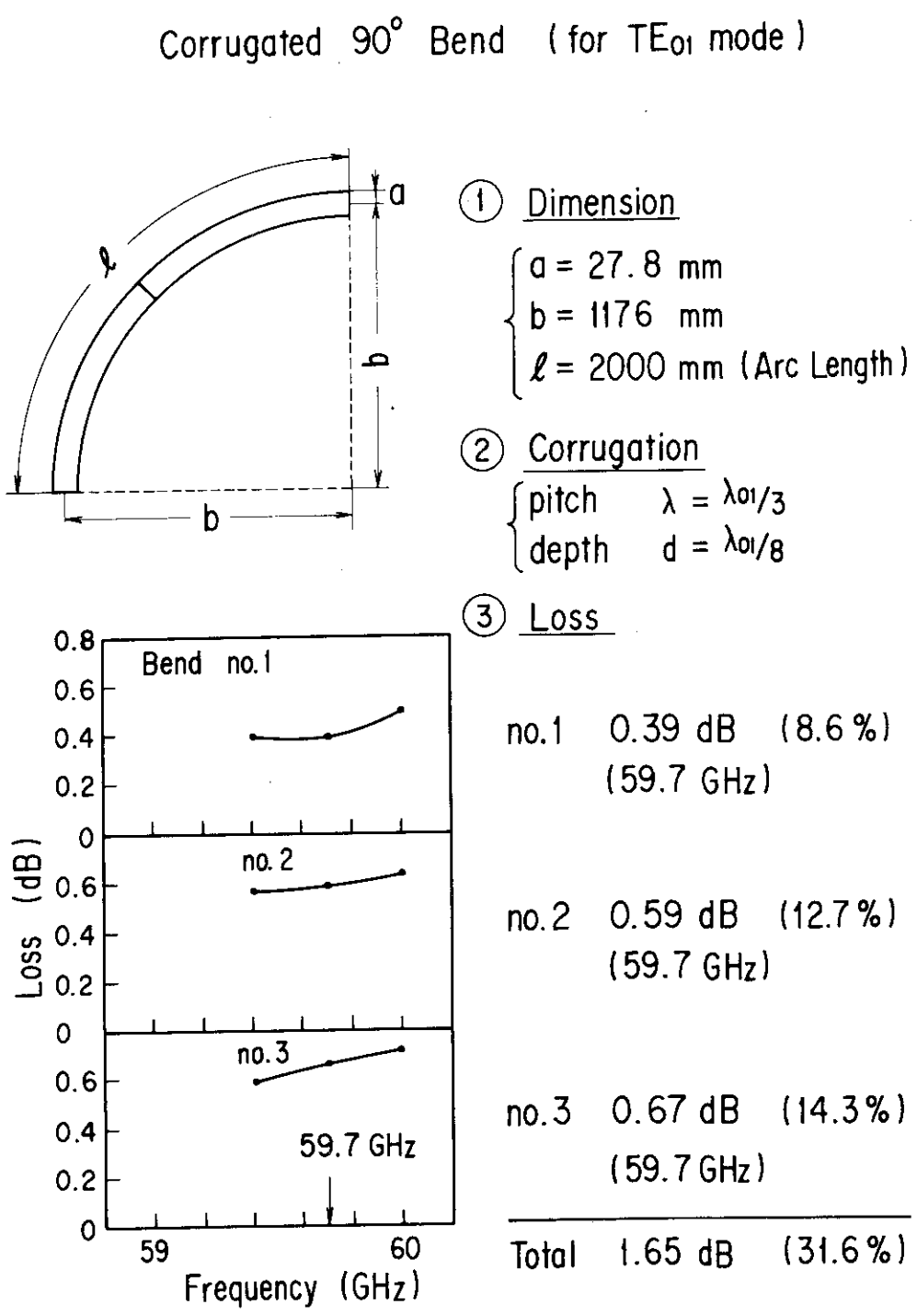

Fig. 3-7 Dimension of the corrugated 90° bend and measured loss in the three bends.

$$\rho(z) \equiv \int_0^Z \frac{1}{2}\,\Gamma\,(Z')dZ'$$

$$\Gamma(z) \equiv \sqrt{(\beta_1 - \beta_2)^2 + 4C^2} \qquad (3.22)$$

β_1 : phase constant of mode 1

β_2 : phase constant of mode 2

C : coupling constant of mode 1 and 2

$$Z \simeq \frac{2kR_1^2\rho_1}{\pi(\chi_{[02]}^2 - \chi_{[01]}^2)} \left[\frac{1}{\alpha}\,(1+\frac{\alpha^2}{4})(e^{\alpha x} - 1) - \right.$$

$$\frac{\alpha}{\alpha^2+1}\,[e^{\alpha x}(\alpha\sin x - \cos x) + 1] -$$

$$\left. \frac{\alpha^2}{4(\alpha^2+4)}\,[e^{\alpha x}(\alpha\cos x + 2\sin 2x) - \alpha] \right]$$

$$\alpha \equiv \frac{1}{\pi}\,\ell n\, R_2/R_1 \ , \quad R(\rho = 0) = R_1 \ , \quad R(\rho_1) = R_2 \ ,$$

$$x \equiv 2\pi\,\rho/\rho_1 \ .$$

The length of taper is obtained from

$$\ell \simeq \frac{2k\rho_1}{\ell n(R_2/R_1)}\,\frac{R_2^2 - R_1^2}{\chi_{[02]}^2 - \chi_{[01]}^2}\left[1 + \frac{\ell n^2(R_2/R_1)}{\pi^2+\ell n^2(R_2/R_2)} + \frac{\ell n^2(R_2/R_1)}{4\pi^2+\ell n^2(R_2/R_1)}\right]$$

$$k(R) = \frac{2\chi_{[01]}\chi_{[02]}}{\chi_{[02]}^2 - \chi_{[01]}^2}\,\frac{1}{R} \ .$$

From the above equations and the relations between mode conversion rate and ρ, the shape and length of the raised cosine tapers are obtained.

We use two kinds of tapers (Fig. 3-8)

Type 1 : R_1 = 27.79 mm, R_2 = 63.5 mm, ℓ = 488.6 mm

Type 2 : R_1 = 19.05 mm, R_2 = 63.5 mm, ℓ = 407.1 mm.

The raised cosine tapers of type I (3 tapers) are used before the TE_{02} directional coupler, before the water load and before the barrier window. The type II is used in the vacuum duct to connect the barrier window and the $TE_{01} \rightarrow TE_{11}$ mode converter.

The measured insertion loss is less than 0.05dB (58.2 ~ 61.2 GHz) and reflection is less than -47dB (VSWR < 1.01, 58.2 ~ 61.2 GHz).

(4) Straight Waveguides

The straight waveguides of radius 27.79 mm (Fig. 3-9) with Shively type flange with copper gasket for SF_6 gas insulation are used. The insertion loss is less than 0.05dB. The measured total loss in ~21 m is ~-0.7dB. The deflection of the setting of the straight waveguide is within 2 mm.

The calculation of the loss of the straight waveguide is given in sec. 3.1.1(1).

(5) Vacuum Window

The vacuum barrier window (Fig. 3-10 and Table 3-5) is made of BeO ceramic which is the same as the gyrotron output window. BeO dust and fumes are highly toxic, and one has to take care not to break it when one handles it.

(6) DC Break/Mode Filter

This component has the following two functions.

1. Insulation of the vessel potential.
2. Filter of the non-circular mode.

The specifications are given in Table 3-6. It is composed of teflon insulation with 4 conducting plates (Fig. 3-11). An rf power absorber is wound around the plates. But this absorber was found to be burnt after the one month experiment. A new DC Break/Mode Filter which uses cooling water as the absorber is under testing.

(7) Horn Antenna

The rf wave in TE_{11} mode is launched from a conical horn antenna (Fig. 3-12). The measured full half width at 3dB point is 8.8° in E-plane and 7.7° in H-plane. The narrow beam divergence was obtained by putting a spacer between the $TE_{01} \rightarrow TE_{11}$ mode converter and the horn antenna. The spacer was put in to optimize the phase of TE_{12} mode which is generated from TE_{01} mode in the mode converter. Without the spacer, measured pattern was 11° in E-plane and 20° in H-plane. Thus the radiation pattern is a sum of the radiation patterns of TE_{11}, TE_{12}, TE_{01} and TM_{11} modes. The measured ratio of the electric field of these modes at the output of the $TE_{01} \rightarrow TE_{11}$ mode converter

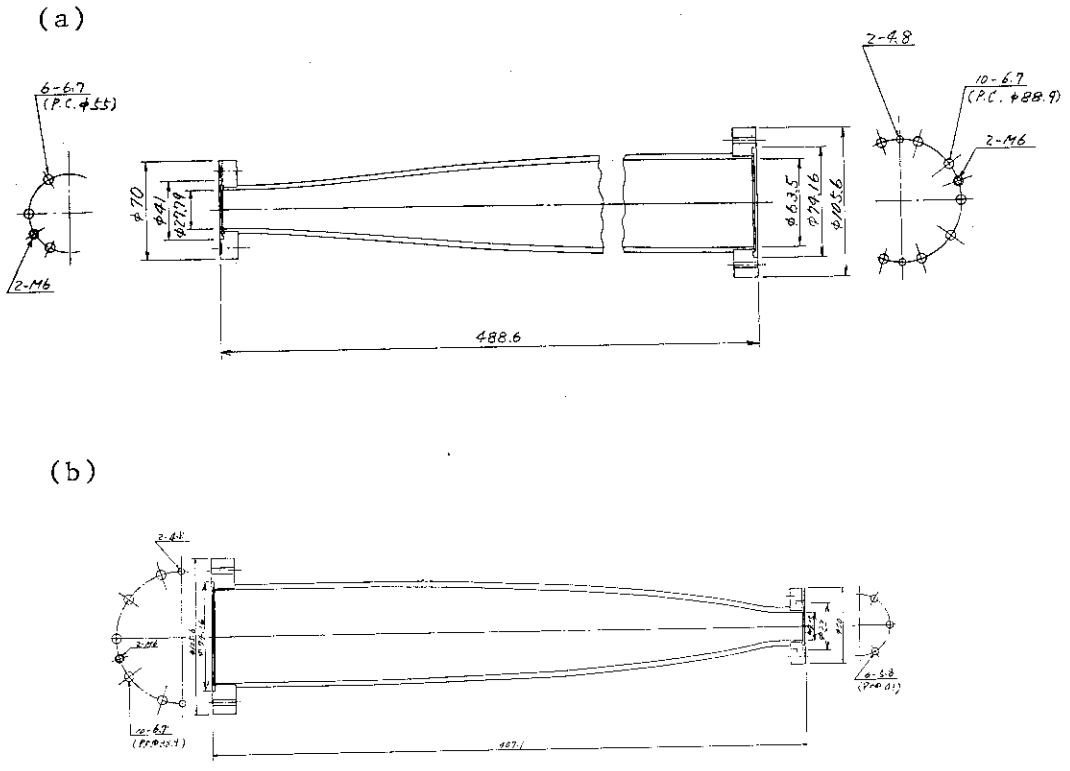

Fig. 3-8 Raised cosine tapers.

(a) Type 1 ℓ = 488.6 mm, R_1 = 27.79 mm, R_2 = 63.5 mm

(b) Type 2 ℓ = 407.1 mm, R_1 = 19.05 mm, R_2 = 63.5 mm

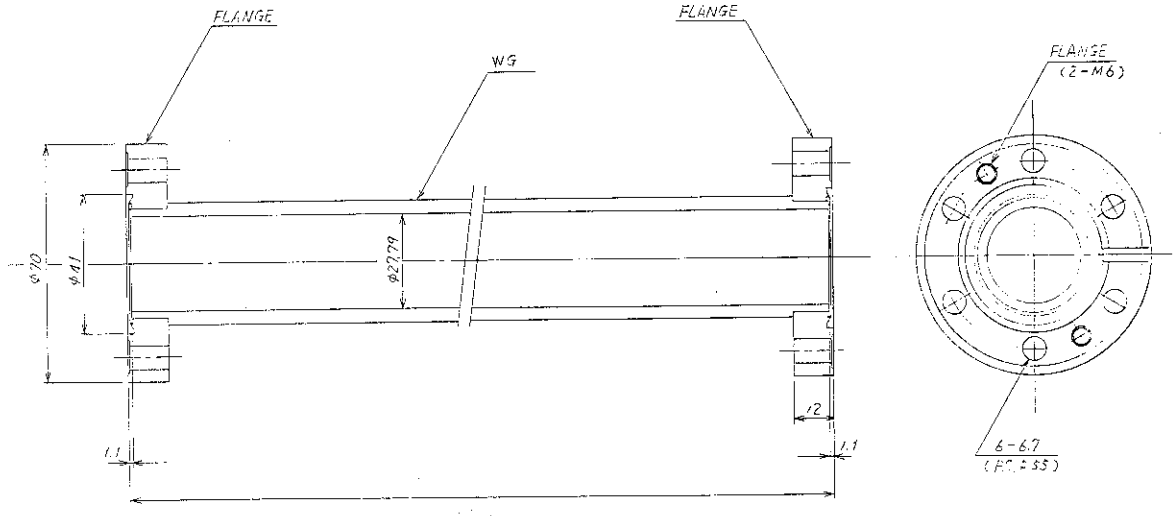

Fig. 3-9 Straight waveguide.

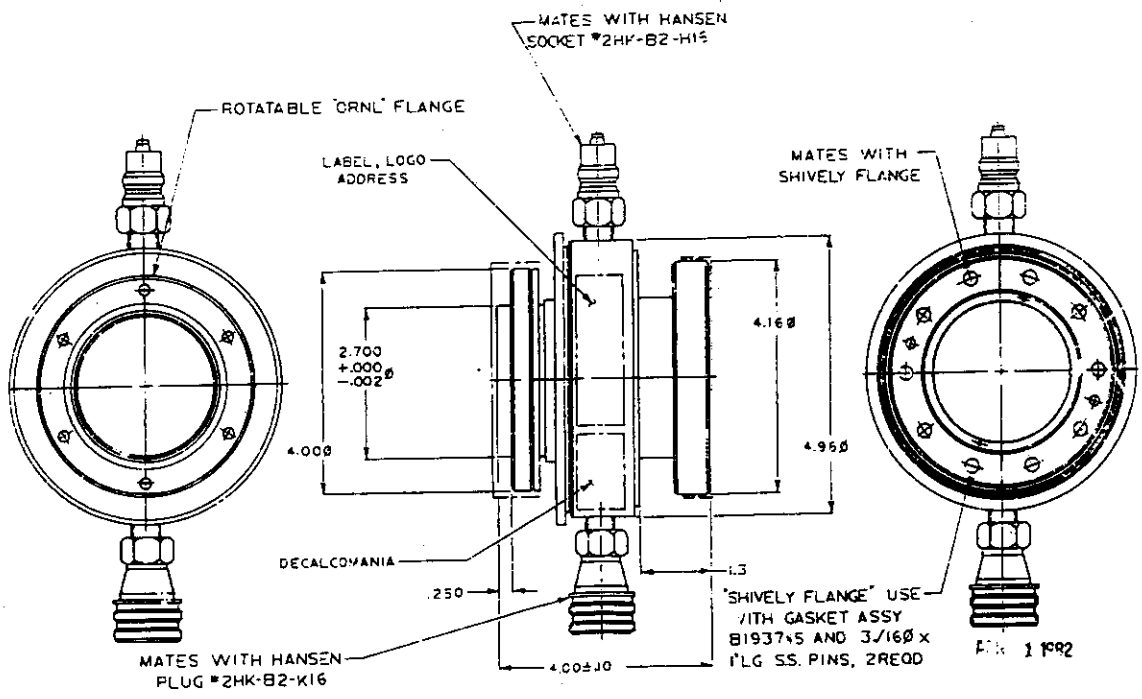

mode	Varian VWE8060-A2
frequency	59.4 - 60.0 GHz
diameter	2.5 inch(63.5 mm)
material	single disc of BeO, bakable
thickness	1.5 guide wavelength
max. power	
pulse	250 kW peak
	1 % duty
	100 msec
cw	10kW
cooling	water 3 gpm, max. 4.4 gpm
max. pressure	40 psig

Fig.3-10, Table 3-5 Vacuum Window

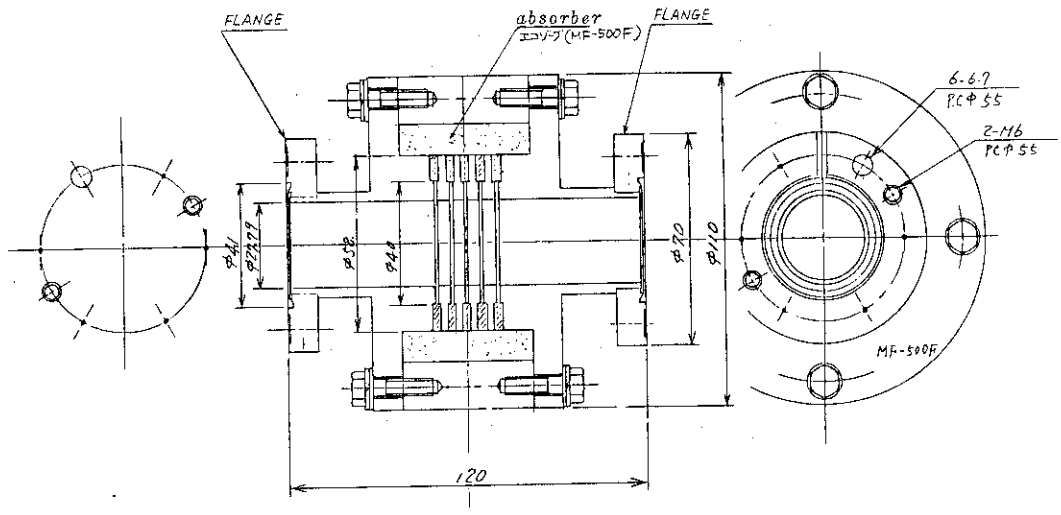

Fig.3-11 DC Break/Mode Filter

Table 3-6 Specifications of DC Break/Mode Filter

loss of TE_{01} mode	0.05 dB(2.3 kW)
TE_{11} mode	0.5 - 1.0 dB(11 % - 21 %)
TM_{11} mode	2.2 dB(40 %)
spacer	teflon, thickness 1 mm × 6
conductor	copper ring of thickness 4 mm × 5
inner diameter	27.79 mm
outer diameter	38.40 mm
absorber	ECCOSORB, water

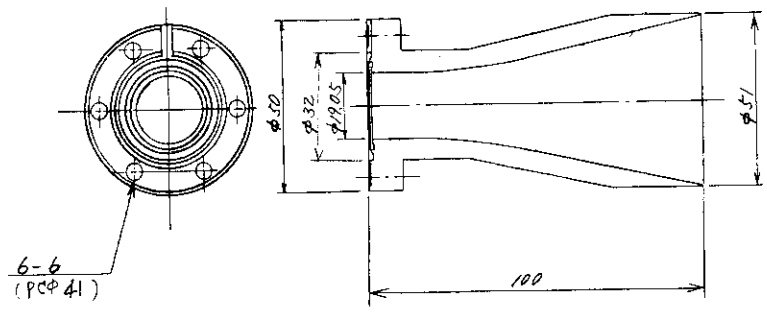

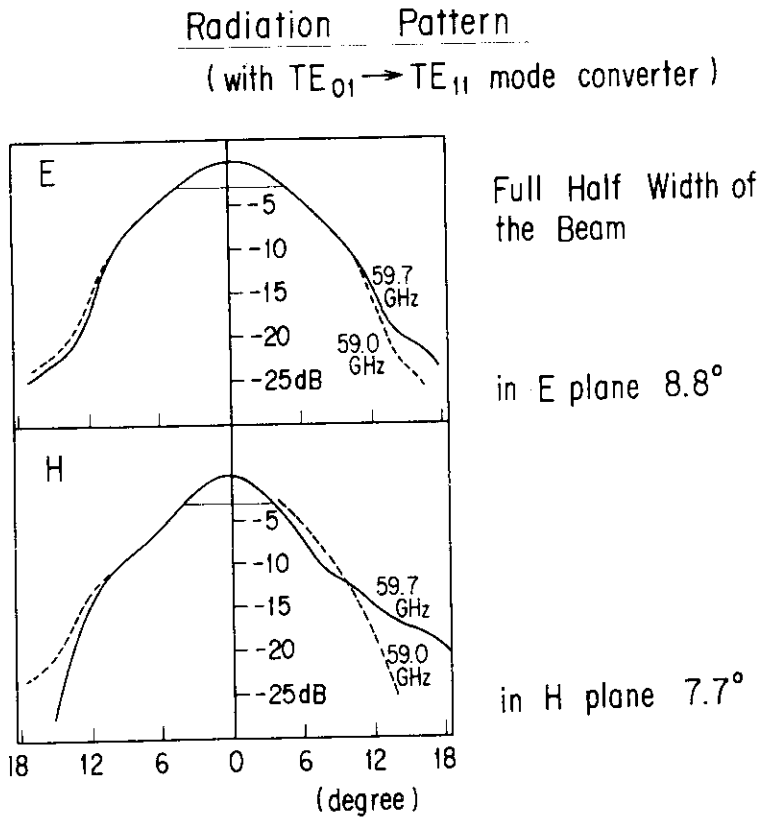

Fig. 3-12 Conical horn antenna and measured radiation pattern

is $E(TE_{11}) : E(TE_{02}) : E(TE_{12}) = 1 : 0.20 : 0.26$.
In considering the TE_{12} mode generated from TE_{11} mode at the circular taper of the conical horn antenna, the ratio of the TE_{12} mode becomes 0.36. By assuming $E(TM_{11}) = 0.14$, and by changing the phase of the TE_{12} mode, one can calculate the radiation pattern of the conical horn antenna. By changing the phase of the TE_{12} mode, the calculated beam width changes from 8° to 20° in H-plane and 9° to 13° in E-plane. These values are consistent with the measured values.

(8) Arc Detecters

Four arc detecters are used (Fig. 3-2) for the detection of the breakdown in the waveguide or in the vacuum-barrier window. Sensor is a photo diode and an optical fiber. A check lamp is installed for a test.

Usually, waveguide arc causes a burst in the reflected power monitored at the TE_{02} mode directional coupler and interlock of the excessive reflected power works also.

The occurence of arc fast-swiches off the beam current of the gyrotron by the regulator tube (X-2062 K).

3.2 RF Monitor System

RF monitor system monitors the parameters of the rf wave.
The functions of the system are,

1. monitor the power of the forward TE_{02} wave,
2. monitor the reflected power, and generate a stop pulse of the power supply when the excessive reflected power is detected,
3. monitor the general rf power and frequency of the output wave,
4. monitor the arc in the gyrotron,
5. filter out the non-circular modes.

The rf monitor system consists of the following components,

(1) Sampler/Arc Detector
(2) Mode Filter
(3) Raised Cosine Tapers
(4) TE_{02} mode Directional Coupler
(5) Microwave Circuits for the Power Detection
(6) Water Load and Equipments for the Measurement of the Temperature of the Cooling Water.

The schematic of the system is shown in Fig. 3-13(a)(b).

(b)

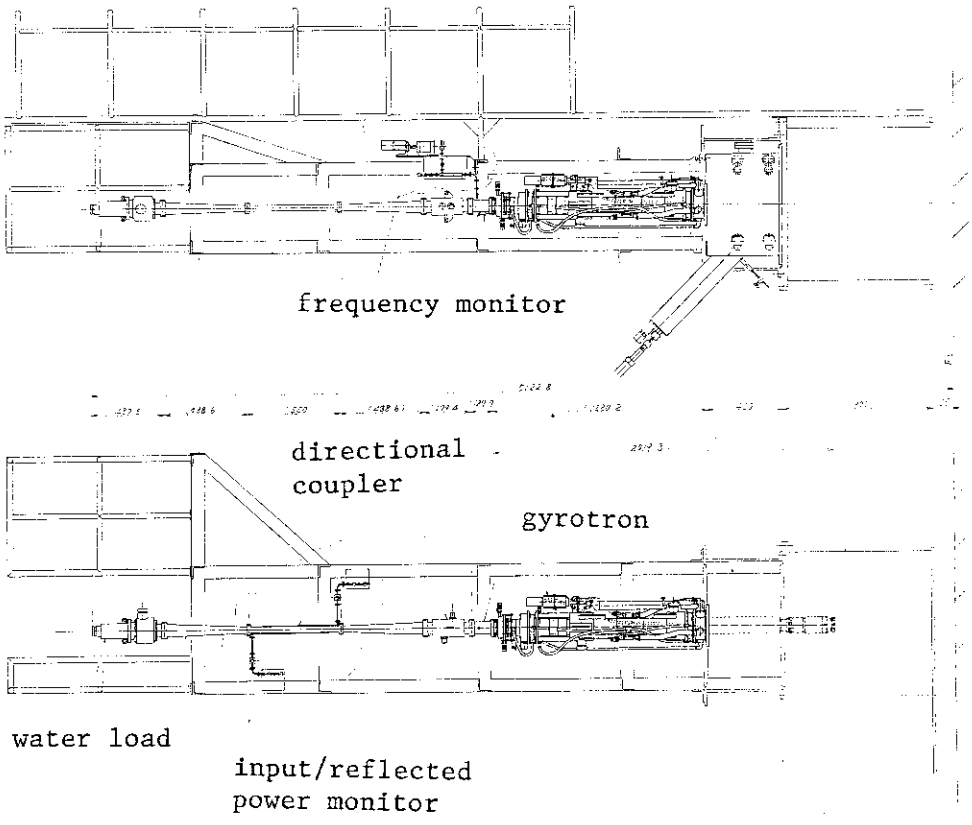

(a)

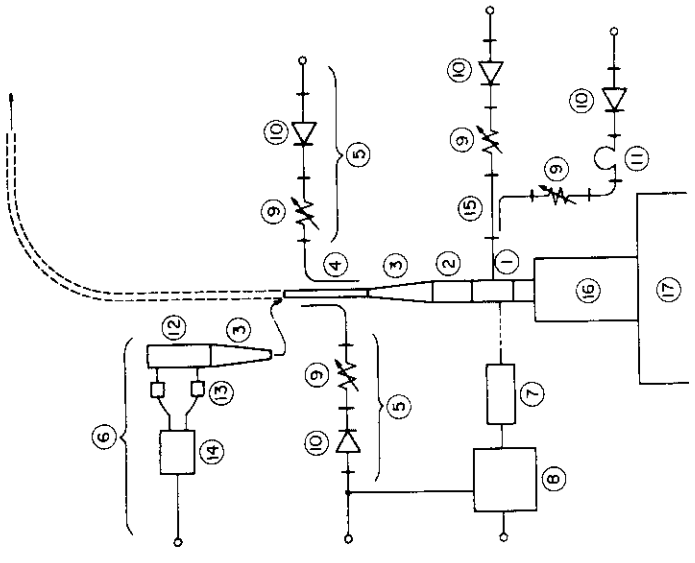

1 Sampler/Arc Detector
2 Mode Filter
3 Raised Cosine Taper
4 TE_{02} mode Directional Coupler
5 Microwave Circuits for the Power and Frequency Detection
6 Water Load and Equipments for the Water Temperature Measurement
7 Arc Detector Head
8 Main Chassis Assy.
9 Variable Attenuator
10 Detector
11 Frequency Meter
12 Water Load
13 Thermistor
14 Calorimeter
15 Coupler
(16) Gyrotron
(17) Gyrotron Tank

Fig. 3-13 RF Monitor System

(1) Sampler/Arc detector and monitor circuit of the general power and frequensy

The sampler has a sensitivity to not only TE_{02} mode but also to the other modes due to a hole coupling. Therefore the exact power of the TE_{02} mode is detected by a TE_{02} mode directional coupler ((4) in Fig. 3-13). The frequency meter ((11) in Fig. 3-13) is remote controlled at the main control panel in the control room. The rf power in the circuit is measured by the flat broad band detectors (Hyghes 47324H-1211, (10)).

A dip of the rf signal through the frequency meter is also monitored at the main control panel. The frequency meter is a two-port device with a tunable cavity. Tuning is done by a robust which is controlled by a pulse motor which is controlled at the main control panel.

(2) Mode Filter

The mode filter eliminates the non-circular mode and the higher circular modes which are trapped between the taper and gyrotron. These modes are dangeraous not only for the break down at the gyrotron window but also for the gyrotron operation. The gyrotron operation is very sensitive to the reflected power.

(3) Raised Cosine Tapers

See sec. 3.1.3(3).

(4) TE_{02} mode Directional Coupler

The power of the forward TE_{02} wave and the reflected TE_{02} wave are detected by a TE_{02} mode directional coupler. The coupling is ~60 dB. That means that 200 mW out of 200 kW is coupled to each arms. The specifications are given in Table 3-9 and outline is given in Fig. 3-16.

The directionality is important to distinguish between the forward power and reflected power. The mode selectivity is also an important factor for the selective detection of the TE_{02} mode. The selectivity of the TE_{02} mode against the TE_{22} mode which most affects the output from the arm, is 12 dB in a calculation. The TE_{02} selectivity to the other mode is higher as shown in Fig. 3-17.

(5) Microwave Circuits for the Power and Frequency Detection

The diagrams of the microwave circuits for the power and frequency

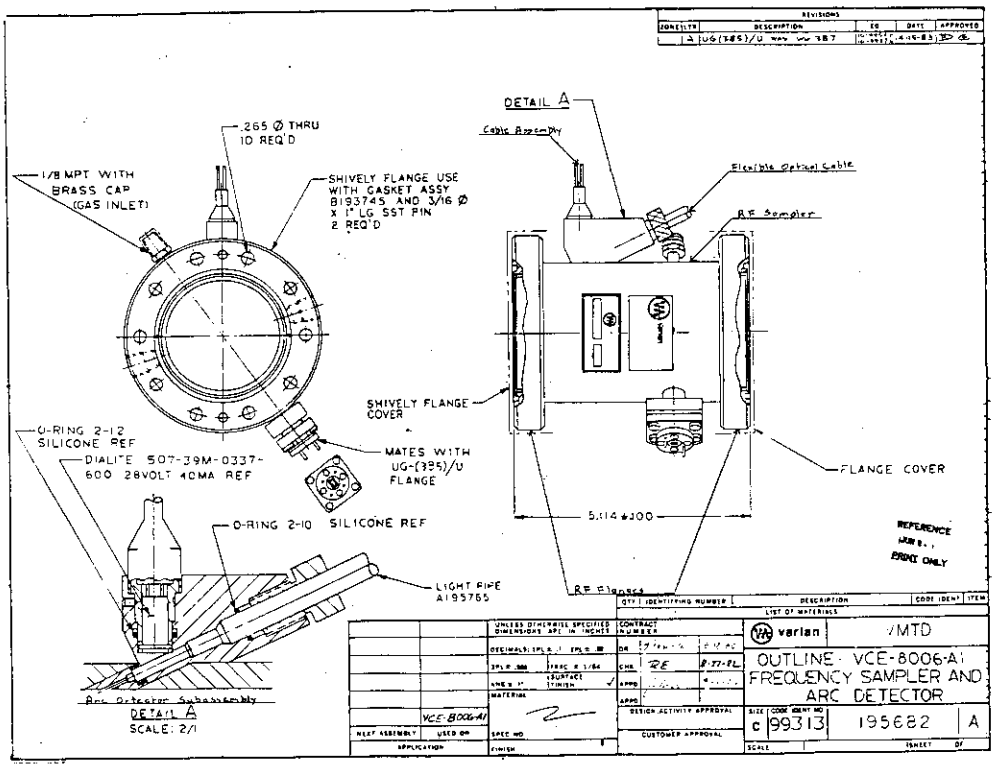

Fig.3-14 Sampler/Arc Detecter

Table 3-7 Specifications of the Sampler/Arc detecter ((1))

model	Sampler Varian VCE-8006-A2	
	Arc detector Varian V9020	
frequency	52 - 60 GHz	
sensitivity	0.1 μW (Tangsten light 2870°K)	
output voltage	+12 V(normal)	
	-48 V(arc)	
time response	< 5 μs	
insertion loss	< 0.05 dB(58.2 - 61.2 GHz)	
VSWR	1.12 (-25.3 dB)	58.2 GHz
	1.07 (-30.0 dB)	59.7 GHz
	1.05 (-32.4 dB)	61.2 GHz

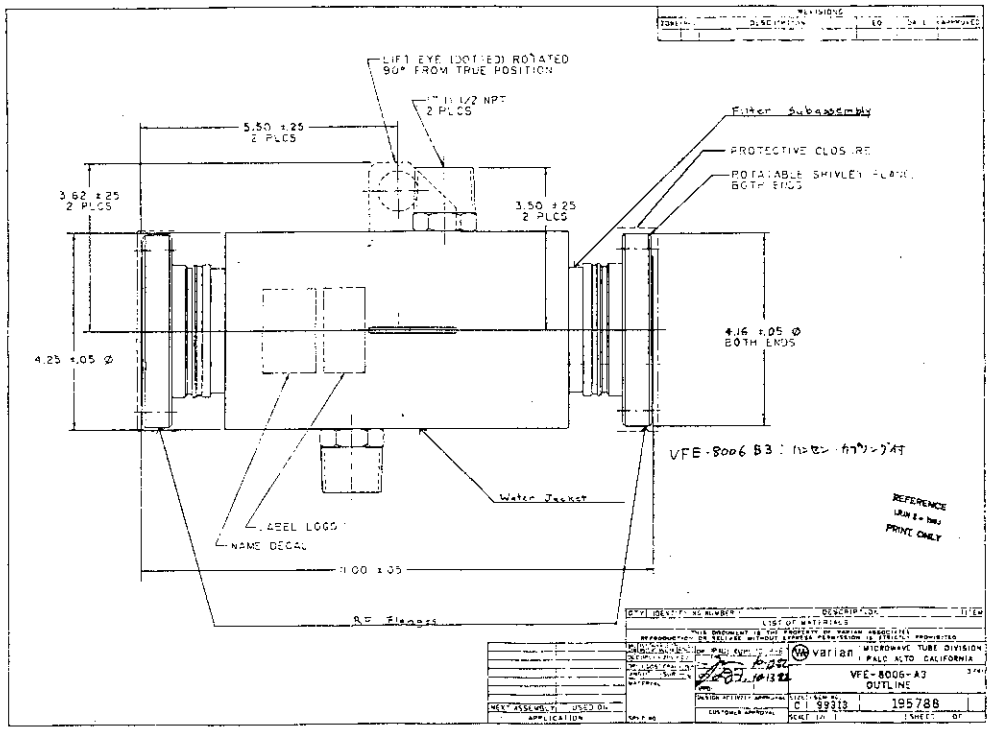

model	Varian VFE-8006-A3	
cooling	water	95 ℓ/min
insertion loss	0.3 - 0.4 dB(TE_{0n} modes)	
	4.0 - 4.5 dB(other modes)	
VSWR	1.12 (58.2 - 61.2 GHz)	

Fig.3-15, Table 3-8 Mode Filter

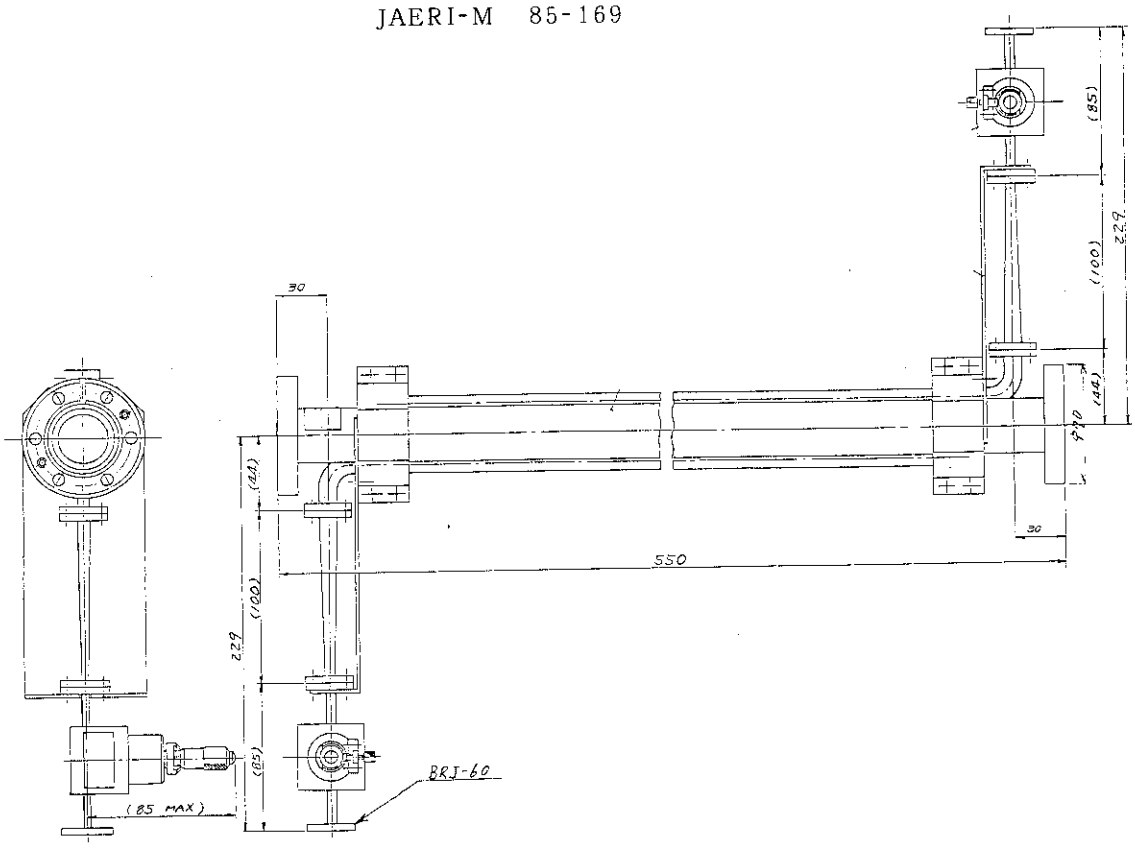

length	550 mm	
inner diameter	27.79 mm	
coupling		
frequency(GHz)	arm 1(forward power)	arm 2(reflected power)
59.4	60.0 dB	59.1 dB
59.7	58.8	58.6
60.0	57.6	58.0
(<±1 dB for the rotation of the directional coupler)		
directionality	15 - 20 dB	
mode selectivity	at 59.7 GHz	
measurement	arm 1	arm 2
TE_{01}	18 dB	20 dB
TE_{11}	19.5	23
TM_{11}	17.0	19
calculation		
TE_{22}	12	12
TE_{03}	>35	>35

Fig.3-16, Table 3-9 TE_{02} mode Directional Coupler

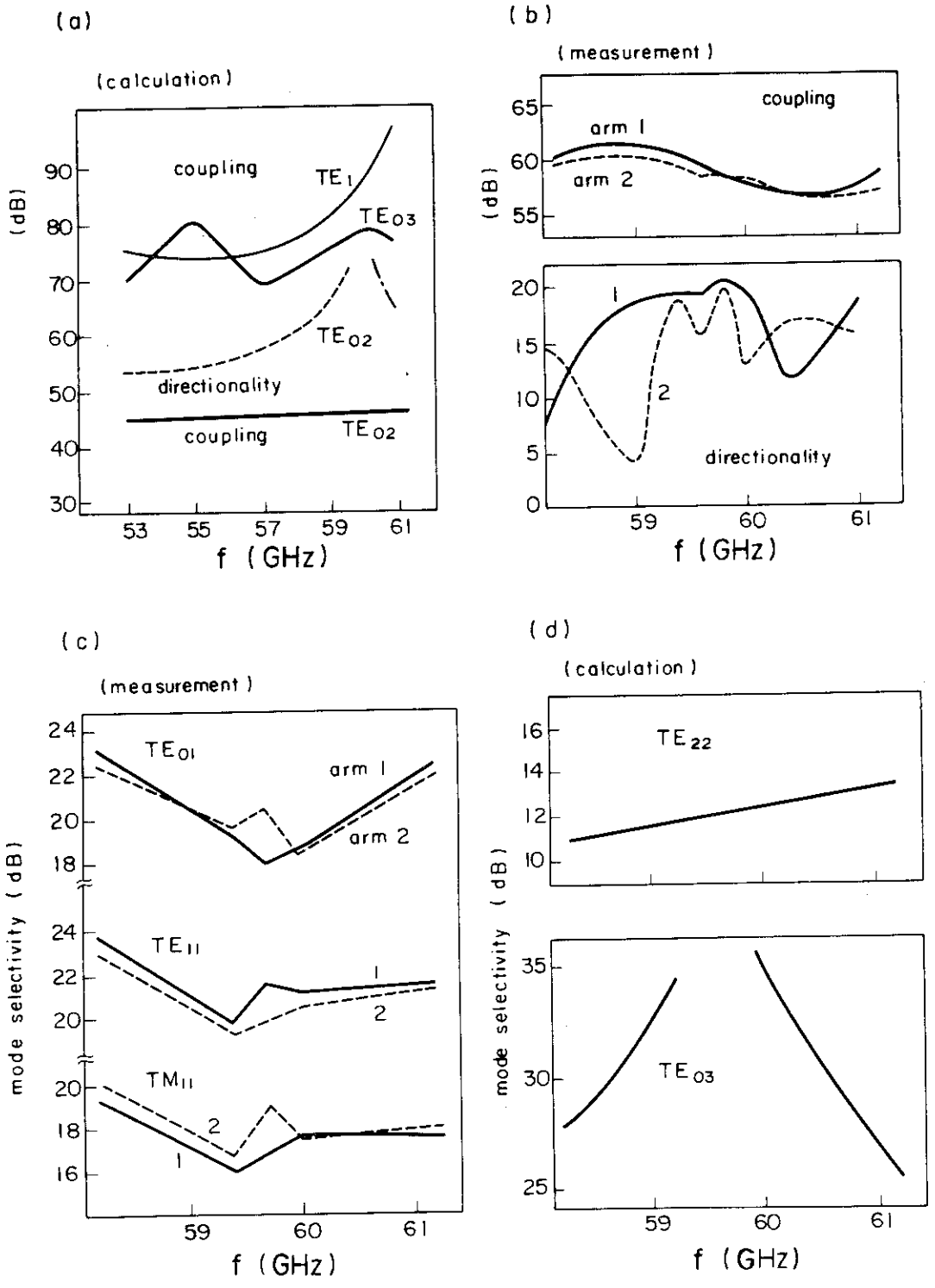

Fig. 3-17 (a) Coupling coefficient to the TE_{02} modes (calculation)
(b) Coupling coefficient to the TE_{02} modes (measurement)
(c) Mode selectivity to TE_{01}, TE_{11}, TM_{11} modes (measurement)
(d) Mode selectivity to TE_{22}, TE_{03} modes (calculation)

detection are shown in Fig. 3-13(a) and Fig. 3-18(a),(b). These are very simple circuits using a few microwave components such as tapers, attenuators, bends and detectors.

The attenuation of the rf signal between the output flange of the arm of the TE_{02} mode directional coupler to the input flange of the detector is mainly due to the attenuator and partly due to the waveguides connecting these components as seen in Fig. 3-18(a). The attenuation was measured and the results are shown in Fig. 3-20(a)(b). Abscissa is the reading of the attenuator. The attenuation includes that by the intervening waveguides. The measured characteristic of the detector is shown in Fig. 3-19. We use the detectors with 50Ω terminations. The characteristics of the detectors used in each arms are given in Fig. 3-20(c)(d).

The total attenuation is the sum of the attenuation (coupling) at the arm of the TE_{02} mode directional coupler (as given in Table 3-9) and the attenuation by the attenuator and the waveguide. One obtains the forward or reflected rf power from the output voltage of the detector using these curves in Fig. 3-20 and the measured attenuation (coupling) at the directional coupler given in Table 3-9.

The frequency measurement circuit is shown in Fig. 3-18(b). The frequency is measured at the Sampler/Arc Detector above the gyrotron. The reading of the frequency meter appears as a voltage at the main control panel. The calibration curve is given in Fig. 3-21(a). By the measurement of the maximum dip of the detector output, one can obtain the correct frequency of the rf wave. An example is shown in Fig. 3-21(b). One can obtain the accurate frequency with this system.

(6) Water Load and Calorimeter

The total rf power (TE_{02} mode and other modes) is measured by a water load (Fig. 3-22) and calorimeter. There are two methods to measure the rf power. First method is that to continue to pulse the short rf pulses by the internal mode operation (sec. 3.5), and measure the saturated steady-state temperature increase ΔT_w (deg.) with the constant water flow rate F (g/sec). The rf power is calculated using ΔT_w, F and duty (pulse length/pulse period) η from the following equation.

$$P_{rf}[W] = \frac{T_w[\mathrm{deg.}] \cdot F[\mathrm{g/sec}] \cdot 4.2[\mathrm{j/deg./g}]}{\eta}$$

attenuator	TRG V520
detector	Hughes 47324H1211
frequency meter	Shimada 2A601A
directional coupler	Hughes 45324H1103

Table 3-10 Power and Frequency Detection Circuits

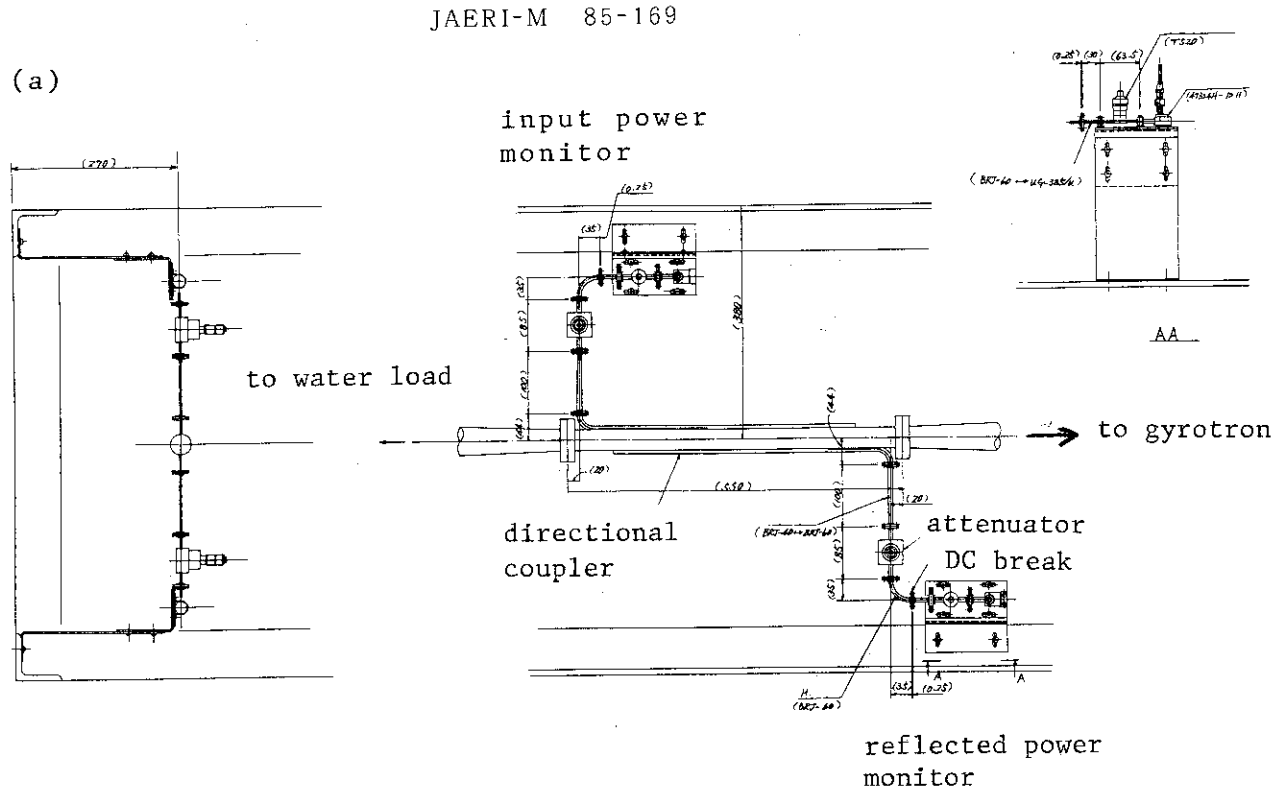

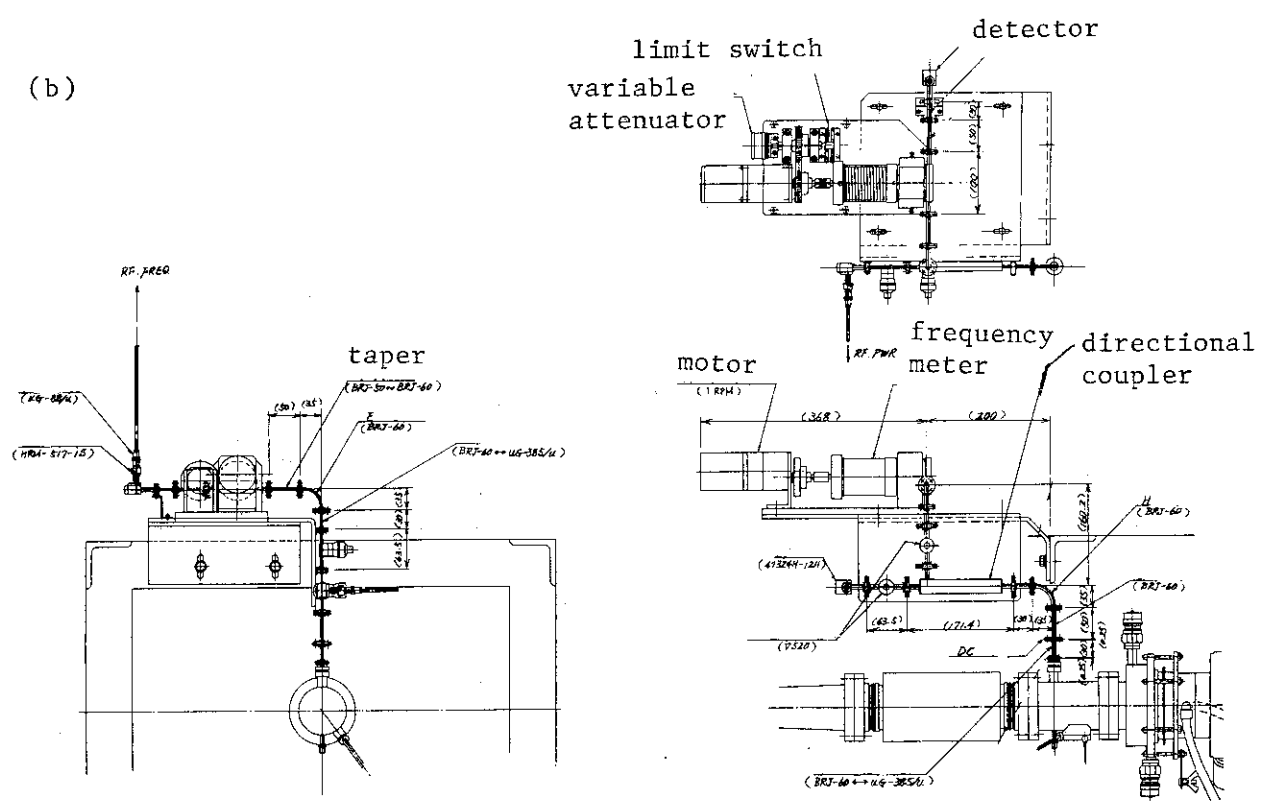

Fig. 3-18 (a) A circuit for rf power detection
(b) A circuit for rf frequency detection

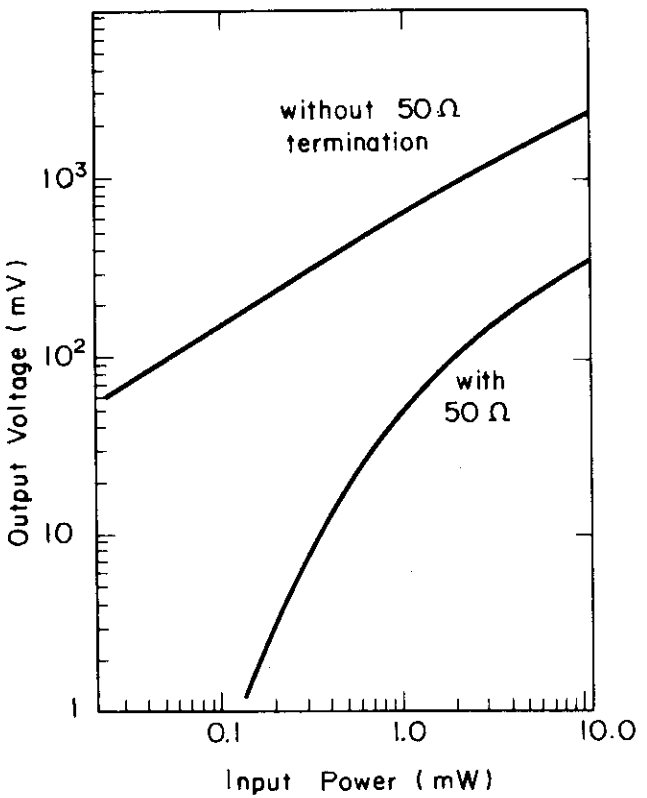

Fig. 3-19 Characteristic of the detector

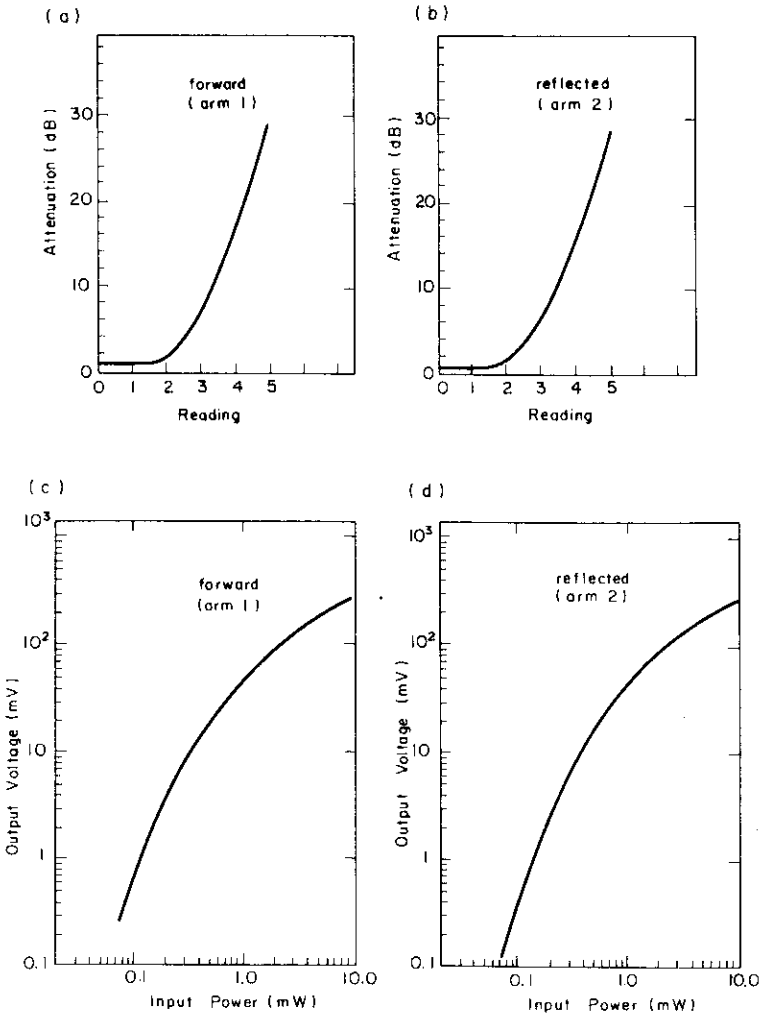

Fig. 3-20 Measured attenuation of the attenuator and waveguides as a function of the reading of the attenuator dial.

(a) arm 1. forward power.

(b) arm 2. reflected power.

Characteristics of the detector

(c) arm 1. forward power.

(d) arm 2. reflected power.

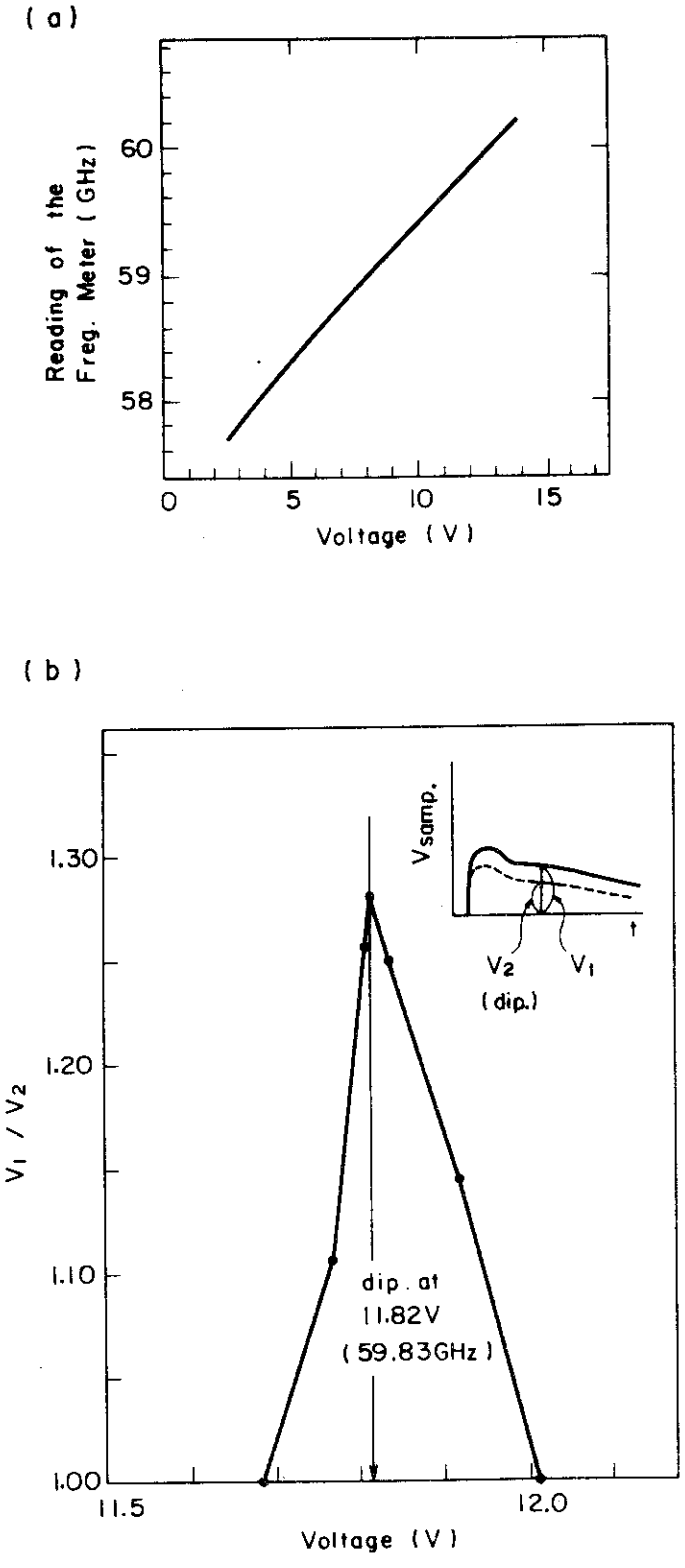

Fig.3-21(a) Calibration curve of the frequency measurement circuit
(b) A result of the frequency measurement

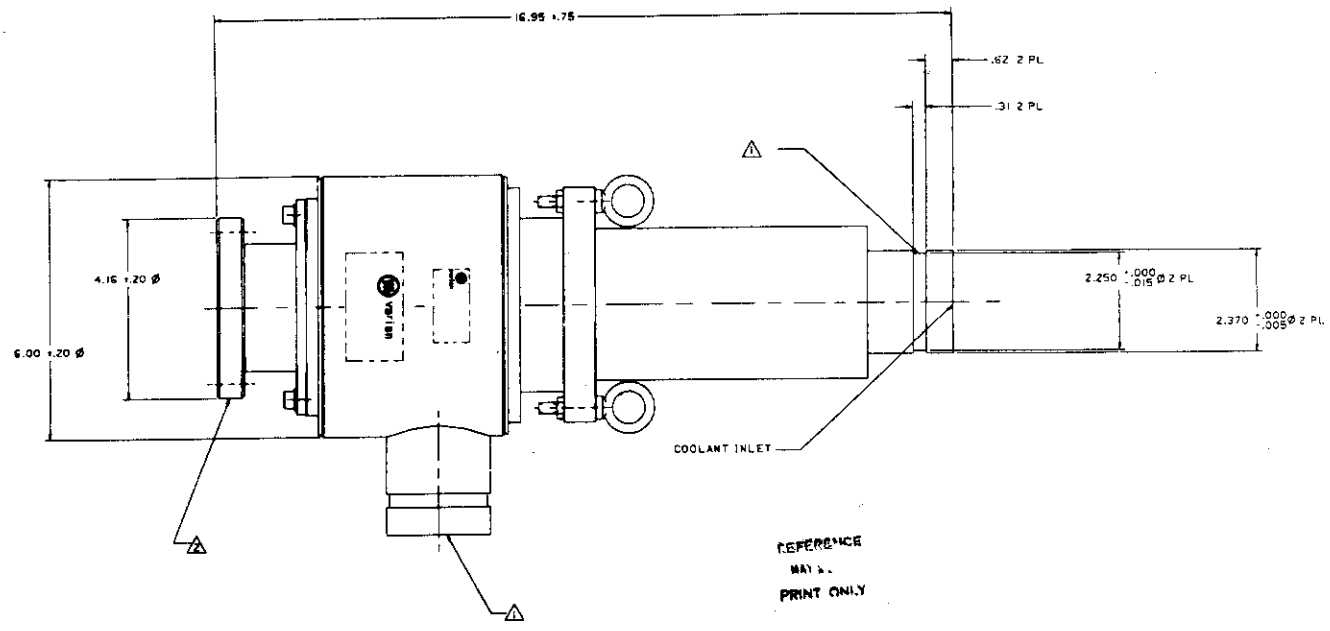

Water Load	
model	Varian VLE8006A8
Calorimeter	
model	Takara Thermister D641
accuracy	±0.01 °C
sampling speed	700 msec

Fig.3-22, Table 3-11 Water Load and Calorimeter

The second method is that to shoot a single pulse and time-integrate the temperature increase of the cooling water. The rf power is obtained from

$$P_{rf} = \frac{4.2\ F \int_0^{\infty} \Delta T_w(t)\ dt}{\Delta t},$$

here Δt is the rf pulse length.

3.3 Gyrotron

A gyrotron is used as the high power source of millimeter waves in our system. 60 GHz is the maximum frequency available commercially. The specifications of the gyrotron is given in Table 3-12. The gyrotron consists of (1) magnetron injection gun, (heater, cathode, gun anode), (2) cavity, (3) collector, (4) output window and (5) ion pumps (gun, collector). The high energy (80 keV) hollow electron beam in a strong axial magnetic field interacts with the cavity field and rf wave is produced by an electron cyclotron wave-particle interaction. The magnetron injection gun produces an 80 kV, 8A hollow electron beam with transverse velocity spread of 1.3 %. TE_{011}/TE_{021} complex cairty is used and perpendicular to parallel verocity ratio $V_\perp/V_{/\!/}$ is ~2 with a d.c. magnetic field of 24 kG.

The output wave is almost polarized in TE_{02} mode (~94 %), but parasitic higher modes are contained by a few percent.

Oscillation mode and power output can be controlled by gun anode voltage V_{GA}, main magnet current $I_{\#1}$, $I_{\#2}$, gun magnet current $I_{\#3}$, heater voltage V_h (beam current I_B) and beam voltage V_B.

Cooling water for body, collecter and window is needed. Especially the large flow rate of 150 GPM (570 ℓ/min) for the collecter makes the cost of the system expensive.

The super conducting magnet and high voltage power supply are described in the subsequent sections.

The typical mode map of the 60 GHz gyrotron is given in Fig. 3-23. The correct region of TE_{02} mode (59.7 GHz ~ 60.0 GHz) oscillation lies in the parameter region of the magnetic field = 22 ~ 24 kG and V_{GA} = 18 ~ 20 kV. But this region becomes smaller by the existence of error transverse magnetic field which must be strictly

Table 3-12 Specifications of the 60 GHz Gyrotron

Model		Varian VGE8060 SN10	
Type	Cyclotron Resonance Interaction Oscillator	(gyromonotron)	
Operating Conditions			
Beam Voltage	V_B	80.0 kV	(Min. 70 ~ Max. 85 kV)
Beam Current		8.0 A	(6 ~ 10 A)
Gun Anode Voltage	V_{GA}	18.57 kV	(15 ~ 25 kV)
Heater Voltage		6.2 V	(5 ~ 14 V)
Heater Current		2.85 A	(2 ~ 5 A)
Solenoid #1 Current		303,899 A-T	
Solenoid #2 Current		229,728 A-T	
Solenoid #3 Current		5,409 A-T	
Body Current		< 10 mA	(0 ~ 200 mA)
Gun Anode Current		< 2 mA	(0 ~ 20 mA)
RF Wave			
Power Output		200 kW	(150 ~ 250 kW)
Pulse Length		100 ms	
Frequency		59.81 GHz	
Efficiency		30 %	
Duty		1.17 %	
Mode Content	TE_{02}	94 % ± 1 %	
	TE_{01}	4 %	
	TE_{03}	2 %	
	TE_{04}	< 1 %	

Cooling Water Flow		pressure drop
Body	Min. 15 GPM(57 l/min.)	100 psi
Collecter	Min.150 GPM(570 l/min.)	115 psi
Window	4 GPM	
Maximum Outlet Temperature	40 °C	

Power Output sensitivities	
Gun Anode Voltage	0.6 dB/%
Main Magnet Current	1.5 dB/%
Gun Magnet Current	0.3 dB/%
Heater Voltage	0.6 dB/%
Beam Voltage	0.6 dB/%

Load Mismatch

VSWR	power reduction
1.5:1	10 %
2.0:1	30 %

Output Guide 2.5 inch I.D.

Pulse Rise Reguirement $\frac{V_{GA}}{V_B} < \sim 75$ %

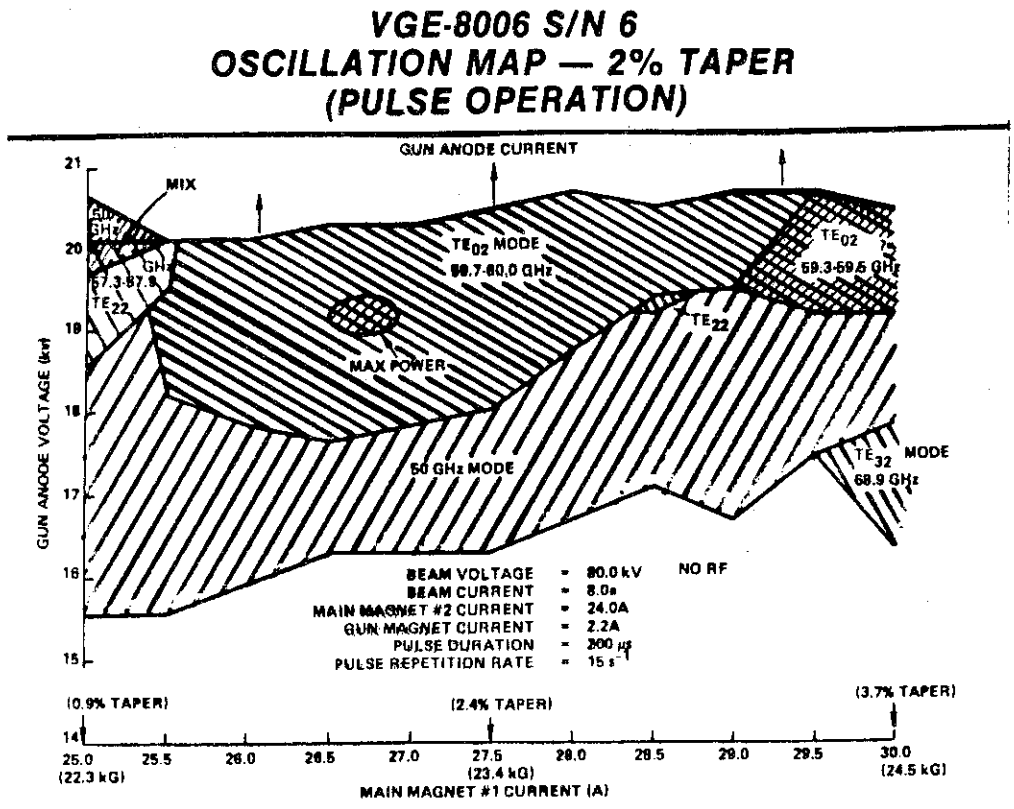

Fig.3-23 Mode map of the gyrotron

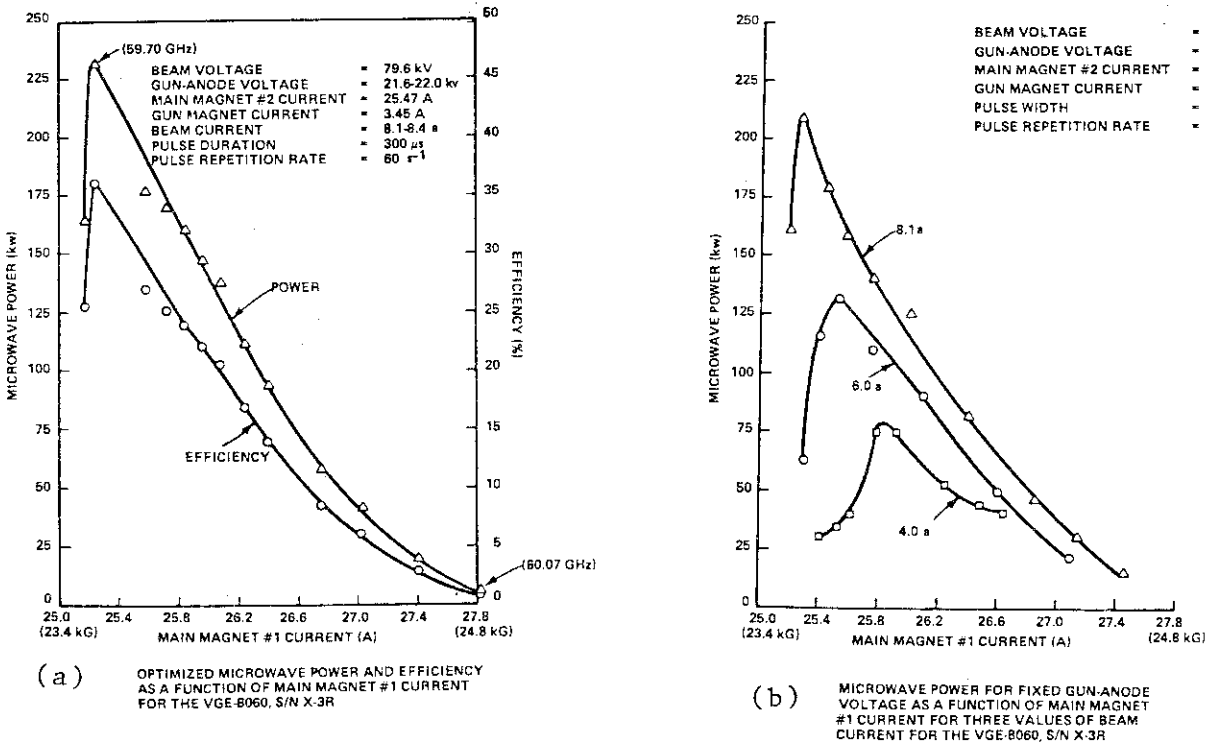

Fig.3-24 parameter dependences

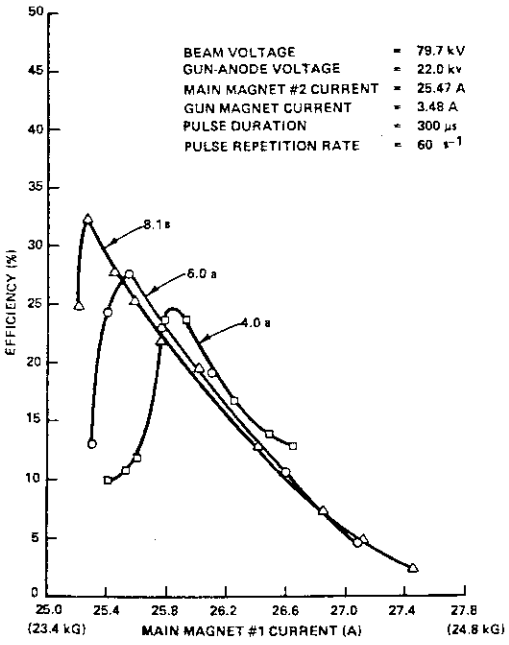

(c) MICROWAVE EFFICIENCY FOR FIXED GUN-ANODE VOLTAGE AS A FUNCTION OF MAIN MAGNET #1 CURRENT FOR THREE VALUES OF BEAM CURRENT FOR THE VGE-8060, S/N X-3R

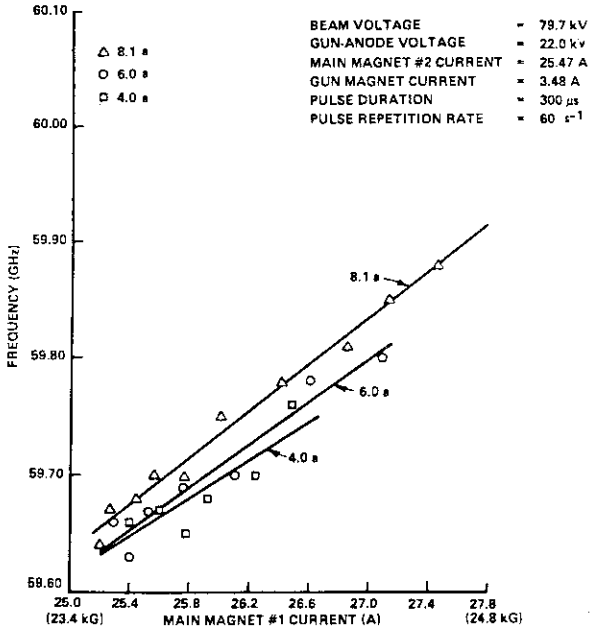

(d) OPERATING FREQUENCY FOR FIXED GUN-ANODE VOLTAGE AS A FUNCTION OF MAIN MAGNET #1 CURRENT FOR THREE VALUES OF BEAM CURRENT FOR THE VGE-8060, S/N X-3R

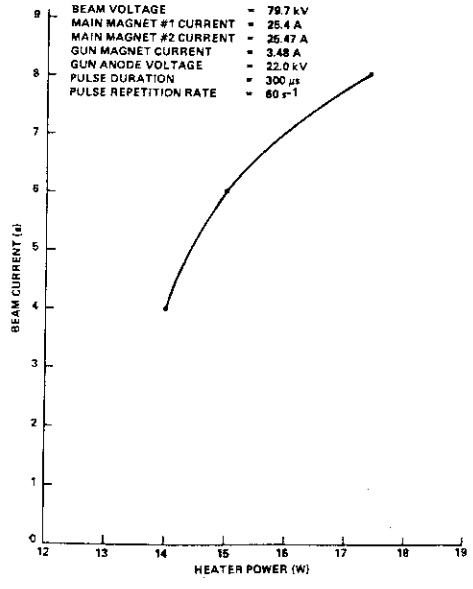

(e) BEAM CURRENT AS A FUNCTION OF INPUT HEATER POWER FOR THE VGE-8060, S/N X-3R

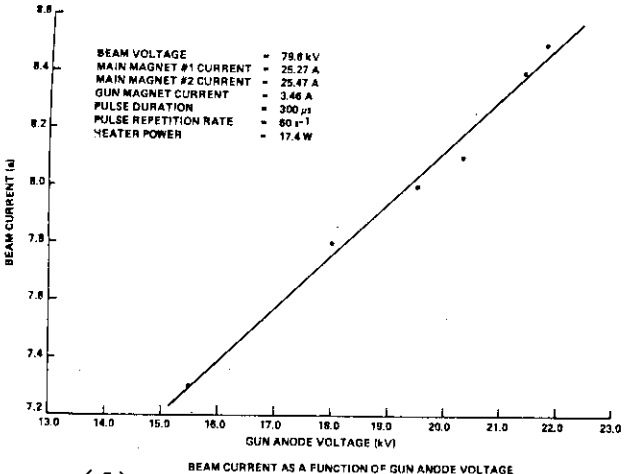

(f) BEAM CURRENT AS A FUNCTION OF GUN ANODE VOLTAGE FOR THE VGE-8060, S/N X-3R

Fig.3-24 parameter dependences (continued)

from "Design and Performance of the VGE-8060 Gyrotron,April 1982, Varian Associates,INC."

reduced to less than 0.2 %.

The typical parameter dependences are shown is Fig. 3-24(a)~(f).

(a) The optimized microwave power and efficiency increases as decreasing current $I_{\#1}$ of the main magnet #1.

(b) Microwave power increases as the beam current I_B.

(c) Efficiency increases as beam current for fixed V_{GA}.

(d) Frequency increases as the magnetic field becomes higher.

(e) Beam current I_B as a function of heater power.

(f) Beam current as a function of gun anode voltage V_{GA}.

The gyrotron is set vertically on a gyrotron tank in which oil for insulation and cooling is filled.

3.4 Super Conducting Magnet System

Super conducting magnet is used for the production of the longitudinal field in the gyrotron (Fig. 3-25). The cavity locates between the two main coils. In the operation of the gyrotron, #1 coil current $I_{\#1}$ is set larger than $I_{\#2}$ and the magnetic field in the cavity has a resulting taper profile. The electron beam at the magnetron injection gun is controlled by the bucking coil (#3). The electron beam is quite sensitive to $I_{\#3}$ and a slight change in $I_{\#3}$ leads to the over current of the body current.

The results of the measurements of the transverse magnetic field in the magnet are given in Fig. 3-26. The fraction of the transverse field with respect to the longitudinal field is less than 0.2 % (Fig. 3-26(a)). The direction of the transverse field is shown in Fig. 3-26(b).

3.5 Power Supply/Cooling System

The constitution of the ECH power supply/cooling system is given in Table 3-14(a). The power supply uses a capacitor bank. A modulator tube (EIMAC X2062K) is used for the beam pulse modulation. The tube has a capacity to operate a few gyrotrons. A gun anode pulse modulator is employed instead of a divider to extend the freedom of the operation (Fig. 3-27). The requirements on the stability of the beam pulse and gun anode pulse are strict (Table 3-14(b)), because the power output is sensitive to these parameters as was shown in Table 3-12. The requirements on the rise/decay time of the beam pulse

Table 3-13 Supper Conducting Magnet System

Super Conducting Magnet

nominal field	2.5 T								
transverse component of the field	< 0.2 %								
magnets									
	I.D.	height	inductance	curren nominal	curren max.	coil resistance 20 °C	coil resistance 77 °K(Liq.N_2)	turns	
main coil #1 (cylindrical)	152.4 mm	76.2 mm	155 H	9.8 A	11 A	6.66 kΩ	0.810 kΩ	320,000 AT.	
main coil #2 (cylindrical)	152.4	76.2	155	9.8	11	6.53	0.799	320,000	
bucking coil #3 (cylindrical)	203.2	25.4	32	-2.1	-2.5	2.66	0.328	- 21,430	
steering coil #4	250	187.5	0.1	10	10	4+6 0.251	0.031		
" #5	"	"	"	"	"	5+7 0.251	0.030		
" #6	"	"	"	"	"				
" #7	"	"	"	"	"				
(saddle coils)									
max. flux	320,000 AT								
energy	14.9 kJ								
material	NbTi (FM)								
Cryostat									
Liq. He	45 ℓ								
Liq. He loss	0.68 ℓ/hr								
Vacuum leak	< 10^{-8} torr ℓ/s								
DC Power Supply									
voltage	10 V								
current	0 ~ 15 A								
current stability	10^{-4} P-P/3hr								
current ripple	10^{-4} rms								
voltage ripple	10^{-3} rms								
current accuracy	0.1 %								
current rise	1.0 ~ 10.0 A/min.(variable)								

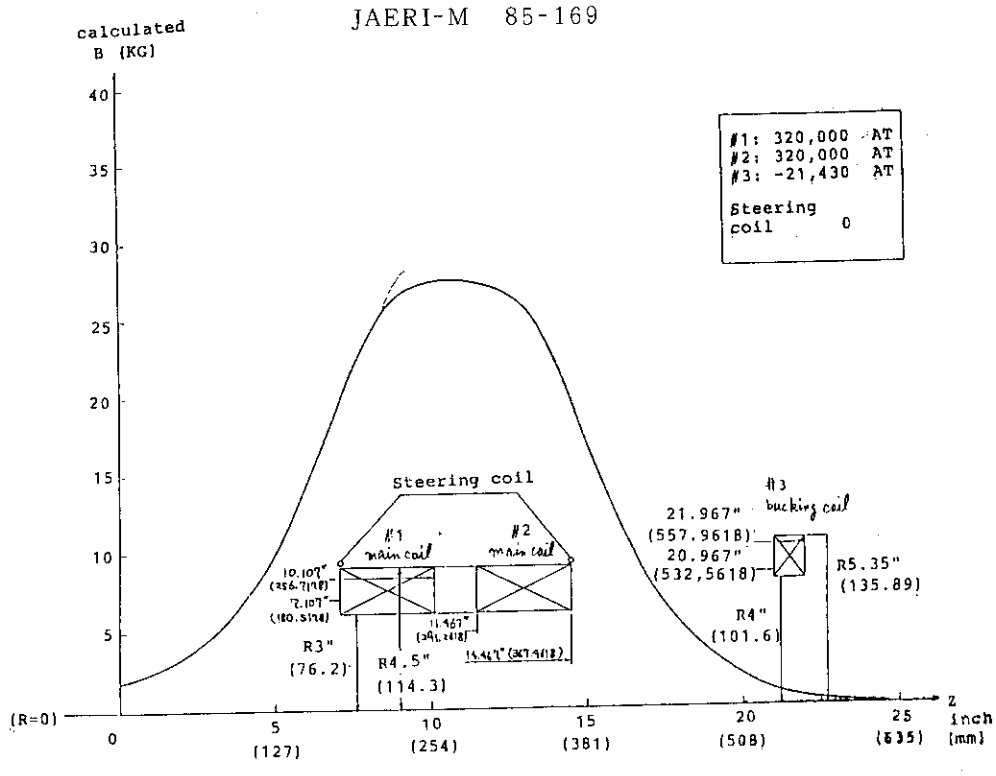

Fig.3-25 Longitudinal field in the gyrotron

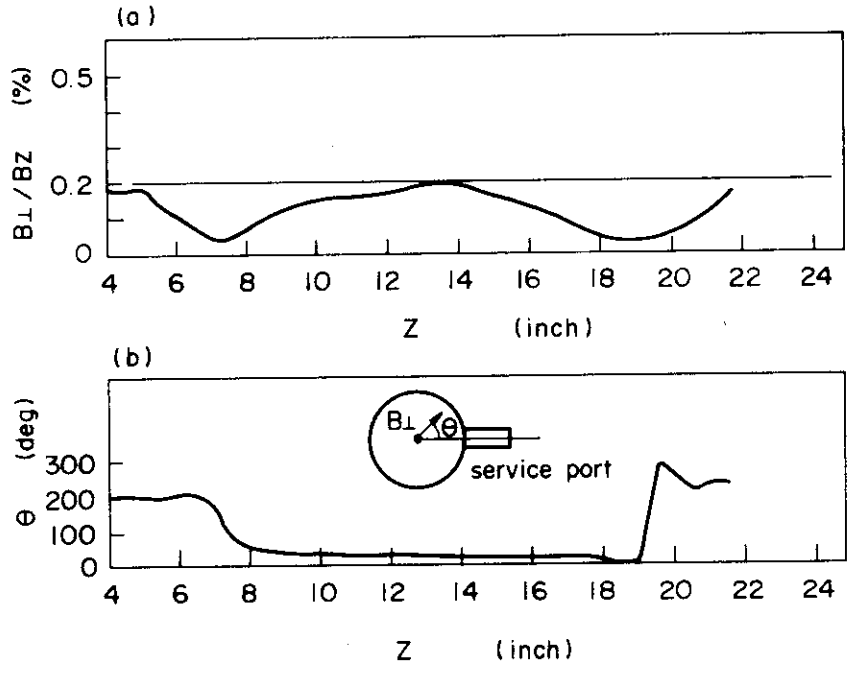

Fig.3-26 (a) magnitude of the error transverse field

(b) direction of the erroe transverse field

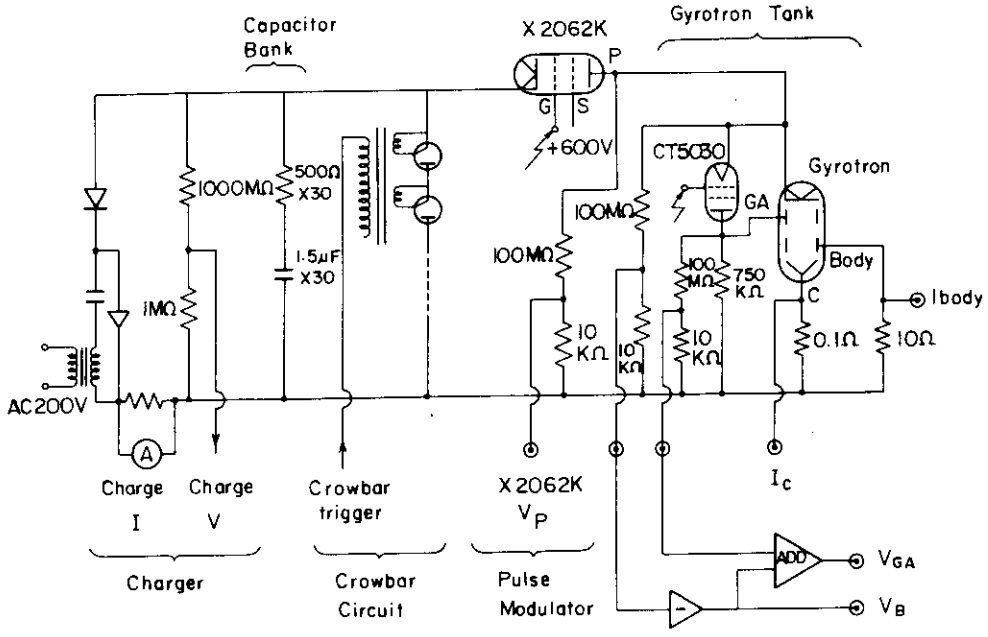

Fig.3-27 Power Supply

Table 3-14(a) Constitution of ECH power supply/cooling system.

1. Charger unit	2. Capacitor bank
3. Crowbar circuit	4. Beam modulator
5. Gun anode modulator	6. Gyrotron tank
7. Gyrotron heater power supply	
8. Gyrotron ion pump power supply	
9. Main control circuit	10. Safety and interlock system
11. Monitor system	12. Water cooling system
13. Oil cooling system	14. SF_6 gas supply system

Beam pulse		
Beam voltage V_B	-20.0 ~ -90.0	kV
Beam current I_B	10	A
Pulse width	0.1 ~ 99.9	ms
Duty	1/300	
Stability of V_B	±0.2	%
Rise/decay time	<300	μs
Overshoot	<±100	v
Gun anode pulse		
Gun anode voltage V_{GA}	15 ~ 30	kV
Stability of V_{GA}	<±0.2	%
Rise/decay time	<500	μs
Overshoot	<±100	V
Heater power supply		
Voltage	0 ~ 16	V
Max. current	6	A
Stability	0.5	%
Crowbar circuit		
response	<5	μs
charge through the gyrotron	<2	mC
Capacitor bank		
capacitance	45	μF
Max. voltage	115	kV
Water cooling system		
ability	10,000	kcal/hr
pressure	9.5 ~ 10.3	kg/cm^2
flow rate	1000	l/min.
water purity	>0.5	MΩ•cm
oxigen concentration	<0.5	mg/l

Table 3-14(b) Specifications of the power supply/cooling system

1. External mode operation (shot by the external trigger pulse. used in case of the injection into plasma)
2. Internal mode operation (shots in the repeated manner by its own clock)
3. Single shot operation (manual)

Table 3-14(c) Operation modes

and gun anode pulse are strict also, to suppress the oscillation in the unwanted modes which are subject to arcs, excessive body current or excessive reflected power. A crowbar circuit is installed for the protection of the gyrotron and the modulator tube.

The power supply has three kinds of the operation modes as given in Table 3-14(c). Among these modes, internal mode operation in which the repeated pulses are obtained within a limitation of the duty cycle (ex. two 1ms pulses per second), is convenient for the optimization of the control parameters of the gyrotron during the power up of the rf output.

The monitor items are given in Table 3-15.

A fast shut down of the beam pulse is required for the protection of the gyrotron in the case of various accidents. The fast protection of the gyrotron during the oscillation is done by the crowbar circuit (time constant < 2 μs) and the regulator tube (time constant < 300 μs) as given in Table 3-16. The most frequent interception of the pulse that occurs during the operations are body over current, rf relection and waveguide arc. A part of these accidents occur due to the gyrotron oscillation in the wrong mode. After the fireing of the crowbar, we have to wait three minutes before the next oscillation can be set. That time looses much of the time economy during the optimization of the operation or during the ECH experiment, because it needs a several shots to find the origin of the trouble, and in each miss shot one has to wait three minuits.

3.6 Gas Supply

The gas supply (Fig. 3-28) pressurizes the rf transmission system with SF_6 gas to prohibit the breakdown in the waveguide. Gas inlet is equipped in the Sampler/Arc Detecter and outlet in the arc detecter near the vacuum window. A rotary vacuum pump pumps out the air in the waveguide and the SF_6 gas is filled in. A safety release bulb is equipped which works at the pressure of 1.3 atm for the protection of the vacuum windows.

Without the SF_6 gas, arc in the waveguide was frequently occured.

Table 3-15 Monitor items at the main control panel

Power supply monitor

(1) charge voltage
(2) charge current
(3) X2062K control grid voltage
(4) X2062K cathode current

Gyrotron monitor

(1) heater voltage
(2) heater current
(3) body current I_B
(4) collector current I_C
(5) gun anode voltage V_{GA}
(6) beam voltage V_B

RF wave monitor

(1) incident power P_{rf}
(2) reflected power P_{ref}
(3) sampler power P_{samp}
(4) rf frequency
(5) water load temperature

Table 3-16 Interlocks (fast interruption of the power supply)

	trip level	HV Off	X2062K Off	Crowbar On
Power Supply				
door	open	@		@
charge current	100 A	@		
charge voltage	110 kV	@		
capacitor curr.	5 A	@		@
crowbar				
thyratron a.V	< 4 kV	@		@
heater I	< 9 A	@		@
dr.unit plate V	<400 V	@		
dr.unit short	> 12 mA	@		
Regulator Tube				
heater	<35, >45A	@	@(heater)	
GS control grid	500 V	@		@
screen grid		@		@
ionpump V	< 3 kV	@	@(heater)	@
" I	> 20 μA	@	@(heater)	@
water flow rate			@(heater)	
" temperature				@
" resistivity				@
I_k	40 A	@		@
I_k off	50 mA	@		@
gas				@
Gyrotron				
heater I	0.5 A	@		@
tube arc		@		@
ion pump V	< 3 kV	@		@
" I	> 5 μA	@		@
Cooling				
gyrotron		@		
magnet				@
oil flow	<2 1/min.	@		
V_B	90 kV	@		@
I_B	10 A	@		@
I_{body}	>200 mA	@		@
gyrotron anode	open	@		@
Wave Monitor				
rf reflection			@	
waveguide arc			@	

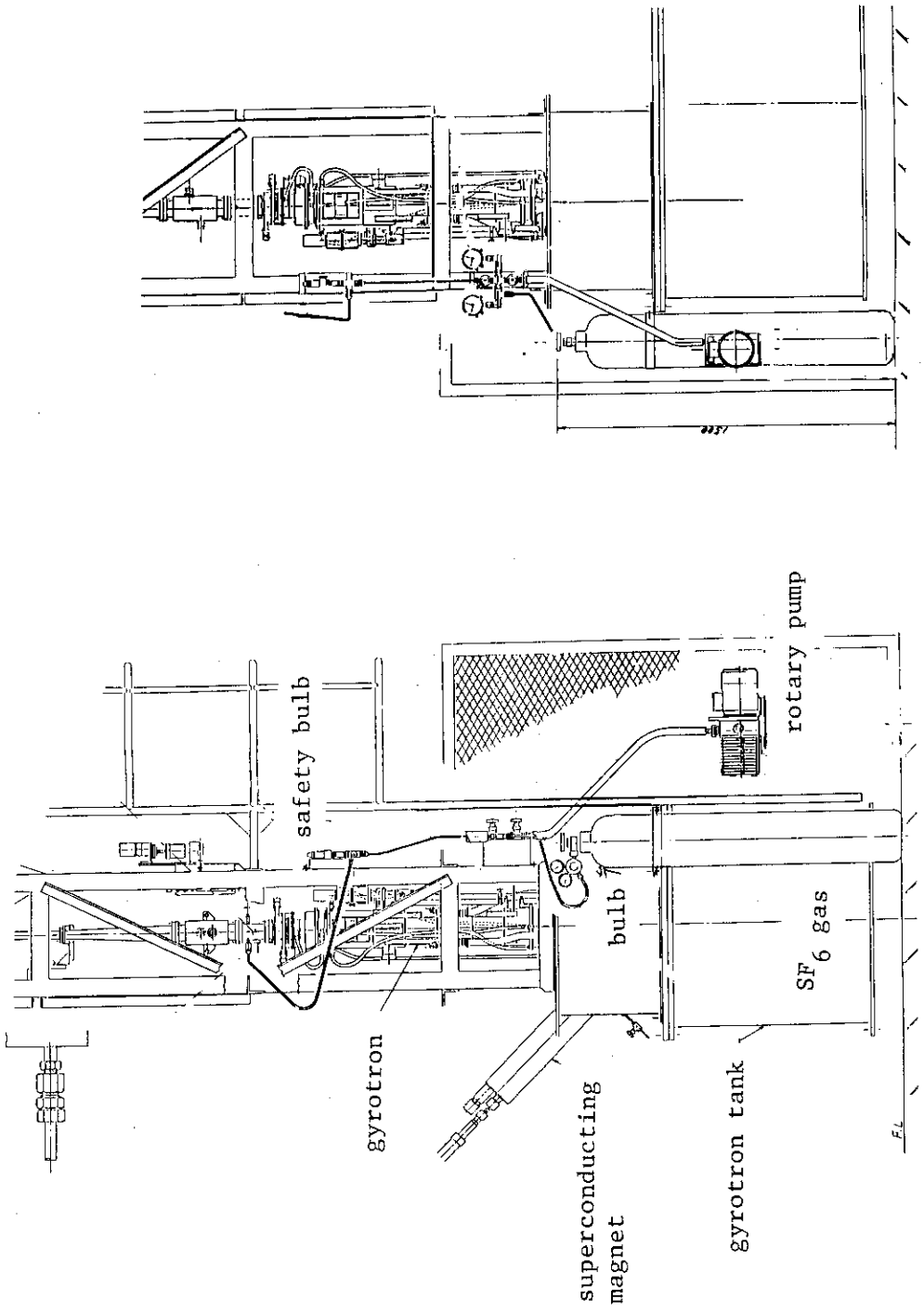

Fig.3-28 Gas Supply

4. Power Tests of the ECH System

4.1 Operation Region of the Gyrotron

The operation region of our gyrotron (Varian VGE-8060 A1 SN10) is shown in Fig. 4-1 (a)~(f). The output power of up to 240 kW can be controlled by several parameters, namely,

main magnet current	$I_{\#1}$	(Fig. 4-1(a)),
gun magnet current	$I_{\#3}$	(Fig. 4-1(b)),
gun anode voltage	V_{MA}	(Fig. 4-1(c)),
beam voltage	V_B	(Fig. 4-1(d)),
and beam current	I_B	(Fig. 4-1(e)).

The mode map is given in Fig. 4-1(f). As shown, in the high $I_{\#1}$ operation, no rf power comes out. The standard way of the initial gyrotron operation is as follows,

1. Raise the gyrotron heater current gradually till the standard value.
2. Set the gun anode pulse width which should be as small as possible in the first operation.
3. Set the beam valtage V_B, main magnet current $I_{\#2}$, and gun magnet current $I_{\#3}$.
4. Set $I_{\#1}$ to high current (~ 11.0 A). Thus we get no rf power.
5. Then set the gun anode voltage V_{MA} around 18.1 ~ 18.5 kV. (C.f. Fig. 4-1(f))
6. Shoot a single pulse, and check I_B, V_B, V_{GA}, I_{body} etc.
7. Begin to pulse periodically in the internal mode operation ~ 2 pulse/sec. After the increase of I_B stopped at the nominal value, lower the $I_{\#1}$, watching the rf power monitor (forward power P_{rf}, reflected power P_{ref}, sampler power Psamp.).
8. If some power is obtained, check the frequency to ascertain that it is the correct TE_{02} mode oscillation.
9. Optimize the main magnet current $I_{\#1}$.
10. Optimize V_{MA}. The maximum power is obtained by the iteration of 9 and 10. Check the power P_{rf}.
11. After that, increase the rf pulse length gradually for the aging, taking care of the ion pump current of the gyrotron for the check of the out gas in the gyrotron.

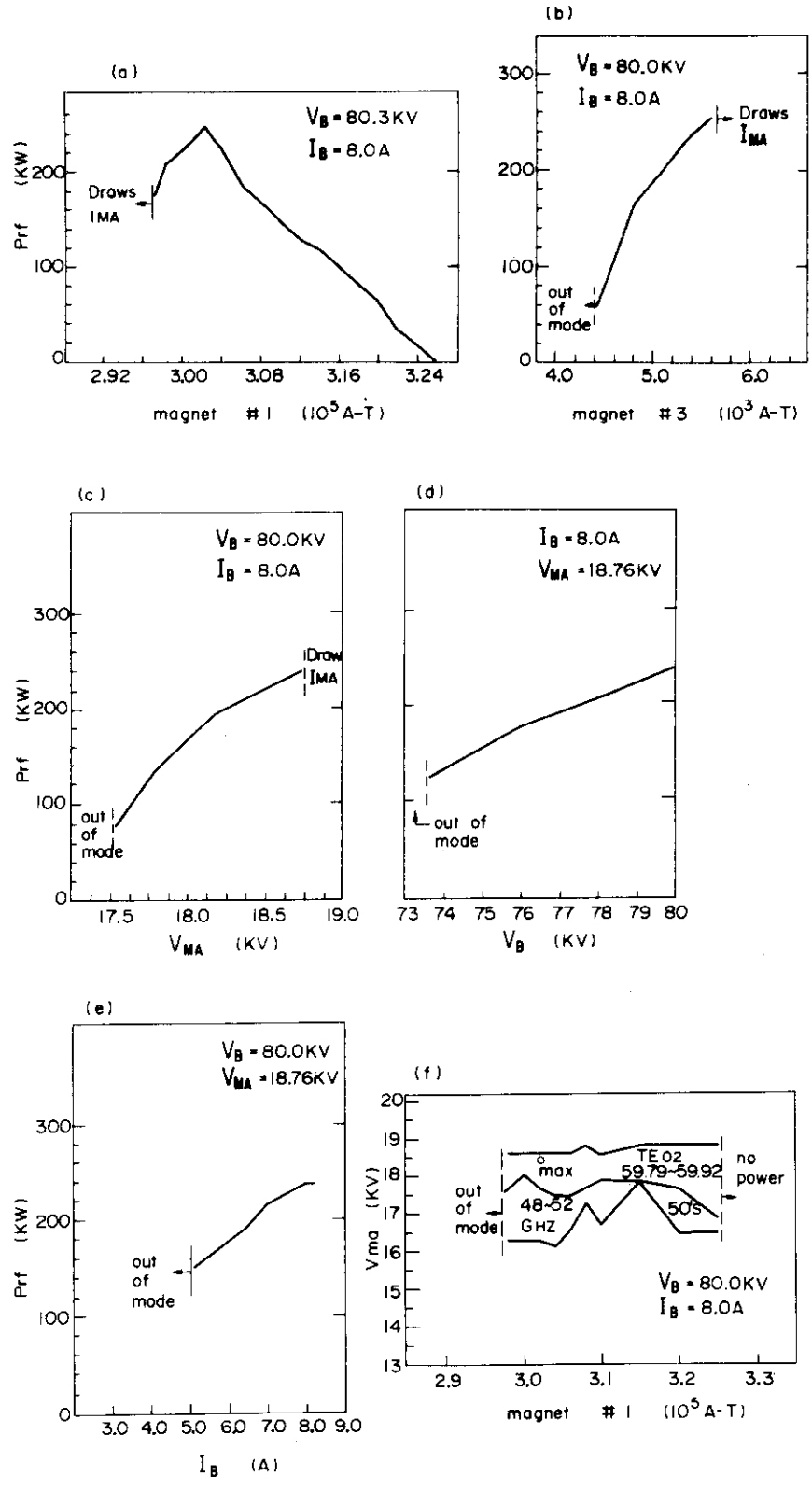

Fig.4-1 (a)-(f) Operation region of the gyrotron

Thus 200 kW, 100 ms pulse is obtained.

The important fast interception during the operations are as follows.

1. Body current I_{body} over current which means that the electron beam touches the wall (cavity, body) somewhere.
2. Gyrotron arc which means the break down near the gyrotron window.
3. Ion pump current over current which means the excessive out gas.
4. Reflected power over power which means the incorrect gyrotron oscillation or something happened in the rf transmission system (as break down in the waveguide). In the case of arc in the waveguide, one can hear the sound clearly.

The wave form of the forward power should be carefully wateched, to avoid the mode jump which appears in the rf signal. The frequency of the wave should be checked when a certain parameter is changed.

4.2 Monitor Wave Form during the Gyrotron Operation

Examples of time evolutions of the monitor signals are shown in Fig. 4-2(a). The collector current I_c (= beam current I_B) starts by the application of V_{MA} with the rise time of less than 100 μs. Body current I_{body} less than 5 mA and gun anode current I_{GA} flow during the pulse. The different pulse shapes are obtained between the forward rf power P_{rf} sampled by the TE_{02} mode directional couplper and general rf power $P_{samp.}$ monitored at the sampler. $P_{samp.}$ consists of various forward modes or reflected modes, and therefore does not indicate the forward power of the TE_{02} mode.

The rise time of V_{GA} ($\equiv V_{MA}$) should be as fast as possible to avoid the spurious mode oscillation which is expressed in Fig. 4-1(f) as 48 ~ 52 GHz mode. The detailed wave form during the rise is given in Fig. 4-2(b). The rise time of V_B is 380 μs and that of V_{GA} is 420 μs. We think it is not fast enough as a burst is observed during the rise time occasionally. We couldn't obtain the independent fast rises of V_B and V_{GA}. With a fast rise of V_{GA}, decrease in V_B occurs. The improvement of the rise time is now investigated.

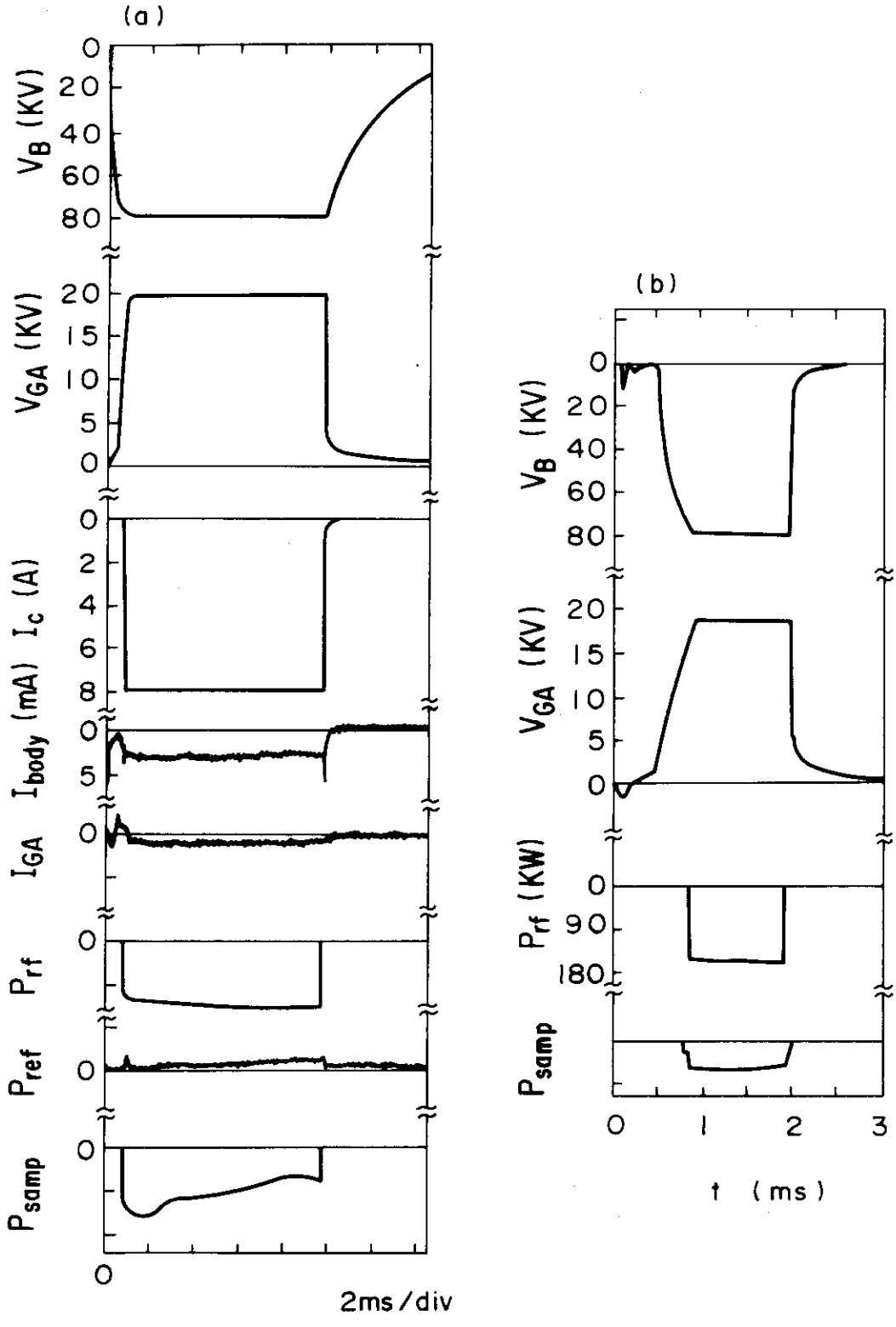

Fig.4-2 Monitor waveform of the gyrotron

4.3 Measurement of the Overall Transmission Loss in the RF Transmission System (Cold Test)

The measurement of the overall transmission loss in the RF Transmission System are done. The sweeper (BWO ascillater) and microwave circuits which is the same as that in Fig. 3-6 is set in the middle of the straight waveguides (point A in Fig. 3-2). By setting the receiver and recorder at point C or B, the loss of TE_{01} mode was measured. The results are summarized in Table 4-1. The overall loss between B C is found as -2.2 ~ -2.5 dB (61 % ~ 57 % transmission) (f = 59 ~ 60 GHz). Subtracting the bends loss -1.7 dB as was shown in Fig. 3-7, and the loss by the straight wave guide -0.4 ~ -0.7 dB (9 % ~ 15 % of the total power) attributes (calculated joule loss $5 \times 10^{-3} \times 25$ m = 125×10^{-3} = -0.13 dB) to the irregularities in connections at the bends and the straight wave guide or the imperfections in the setting (such as the bending).

4.4 Measurement of the Forward RF Power

First the measurement of the forward rf power by the water load at the output of the TE_{02} mode directional coupler was done (Fig. 3-2 D). The comparison of the rf power obtained from the TE_{02} mode directional coupler (using the coupling value measured by a cold test) with the rf power measured by the water load showed a good agreement within a several per cent. As the water load measures the total power (TE_{02} mode + non-TE_{02} mode) and the directional coupler measures mainly TE_{02} mode, the above result shows that purity of the TE_{02} mode from the gyrotron is good.

The power measured by the water load at point D in Fig. 3-2 $P_{WL,1}$ and output voltage of the forward arm of the TE_{02} mode directional coupler Vout is shown in Fig. 4-3(a). Next, the water load is set before the vacuum window (point E of Fig. 3-2). The power measured at the water load at point E in Fig. 3-2 $P_{WL,2}$ and Vout is shown in Fig. 4-3(b). From these figures, we can obtain the circuit loss between point D and E of Fig. 3-2 as shown in Fig. 4-3(c). It shows ~60 % ±10 % transmission of the rf and that value coinsides with the result of cold test in Sec. 4.3.

About 90 % of the power of the TE_{01} mode at the winodow is finally radiated in TE_{11} mode from the horn antenna. Therefore ~54 % of the

Table 4-1 Loss in the RF transmission System

Frequency	59.4 GHz	59.7 GHz	60.0 GHz
Loss between AB (21 m of straight wave guides + 2 bends + 2 arc detectors)	-1.86dB	-1.75	-2.04
Loss between AC (1 bend + 1 arc detector)	-0.45	-0.41	-0.41
Loss in total (CB)	-2.31dB	-2.16dB	-2.45dB
transmission	(58.7 %)	(60.8 %)	(56.9 %)

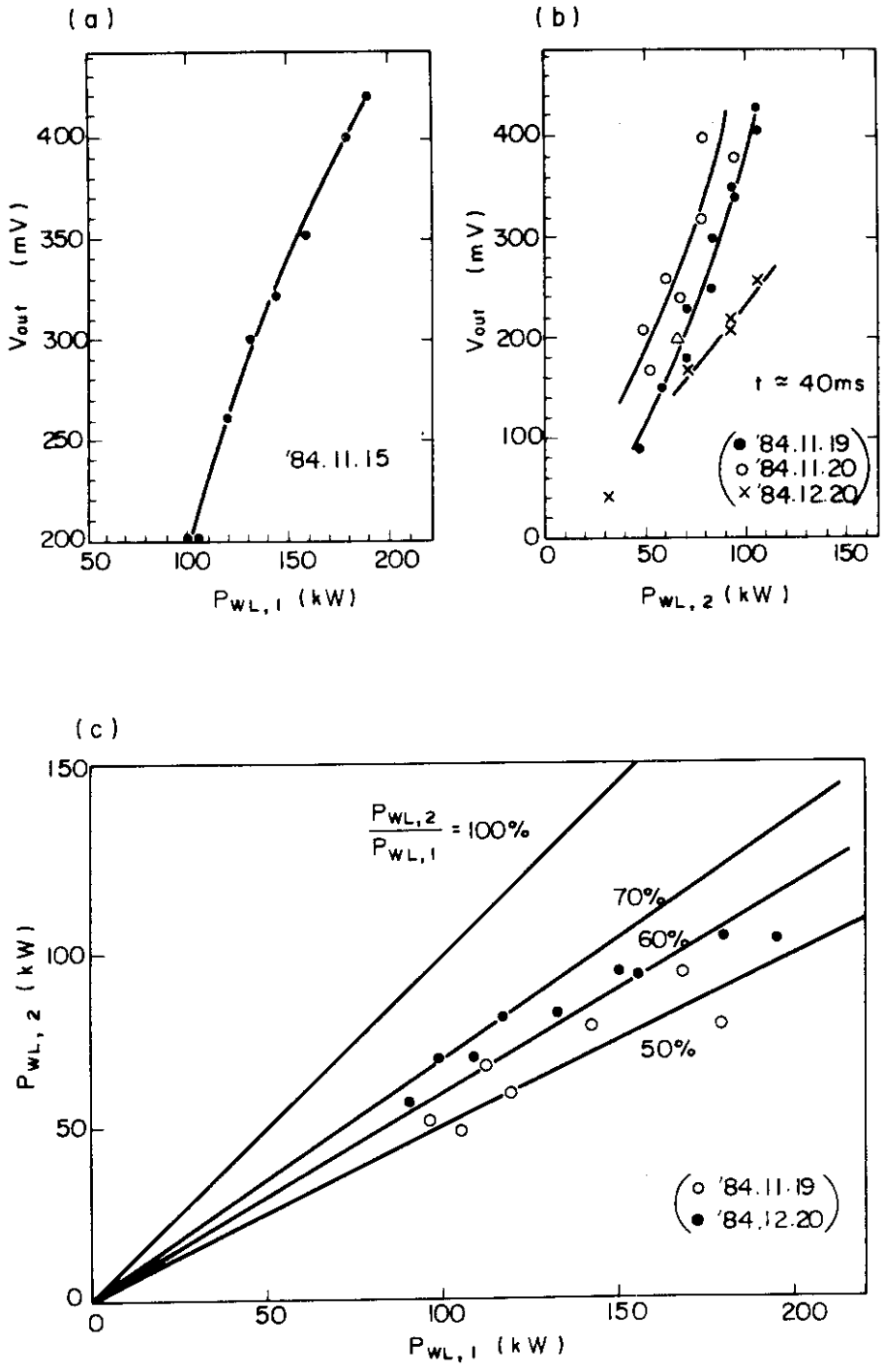

Fig.4-3 (a)the power measured by the water load at point D($P_{WL,1}$) and output voltage of the forward arm of the TE_{02} mode directional coupler
(b)the power measured by the water load at point E($P_{WL,2}$) and output voltage of the directional coupler
(c)Attenuation between point D and E

gyrotron TE_{02} output is finally radiated into the plasma in TE_{11} mode.

The measured reflected power was 3 kW in the 150 kW operation (2 % of the forward power) with the water load set above the gyrotron (point D) in Fig. 3-2. The reflected power increased when the water load is set near the machine (point E) to 5 kW in the 163 kW operation (3 % of the forward power). In case of the injection into the vacuum vessel the reflected power was smaller as 2.2 kW (1.6 % of the forward power of 140 kW). Thus the reflected power is negligibly small in this system.

Conclusion

A 60 GHz ECH system for the JFT-2M tokamak is designed, constructed and tested. It can launch not only extraordinary mode but also ordinary mode by rotating a mode converter by 90° in the vacuum chamber. We first thought that difficulties lie in the design of the mode converters two years ago (1983). Therefore we developed a design study of the mode converters as is described in Chap. 3.1.3. The efficiency of the mode converters completed coincided well with the computer calculation. But it was found that the bend loss is a severe problem which was unforeseen to us. The 32 % of the rf power is lost in the three bends. The improvement of the bends is now under way. An ECH experiment using this system was carried out in the last Nov. - Dec. . A ramp up of the plasma current by ECH of the LH sustained plasma, and local bulk heating of a tokamak plasma in which the core heating efficiency was the same as the foundamental wave ECH were obtained as reported in 5). We are going to get an another gyrotron and power up will be completed in this winter.

Acknowledgements

We would like to express our gratitude to Drs. R.Prater, C.P.Moeller, S.H.Lin and Messers D.Remsen, D.Irwin of GA Technologies Inc., San Diego, CA, USA, who carried out a pioneer work of making and operating a 60 GHz ECH system and carried out the ECH experiments on Doublet III tokamak to which two of the authors (K.H. and T.Y.) took part in. Though the design of our microwave components is different from their components, the basic layout of our transmission system is similar to theirs. We would like to acknowledge Dr. M.Sato of the Heliotron Center of Kyoto Univ. for his advice about the ECH system and many engineers of Mitsubishi Electric Co., who manufactured the ECH system. We are grateful to Mr. K.Suzuki, Drs. A.Funahashi, Y.Tanaka, M.Tanaka, Y.Obata, M.Yoshikawa, K.Tomabechi, Y.Iso and S.Mori of JAERI for their continuous encouragements.

Conclusion

A 60 GHz ECH system for the JFT-2M tokamak is designed, constructed and tested. It can launch not only extraordinary mode but also ordinary mode by rotating a mode converter by 90° in the vacuum chamber. We first thought that difficulties lie in the design of the mode converters two years ago (1983). Therefore we developed a design study of the mode converters as is described in Chap. 3.1.3. The efficiency of the mode converters completed coincided well with the computer calculation. But it was found that the bend loss is a severe problem which was unforeseen to us. The 32 % of the rf power is lost in the three bends. The improvement of the bends is now under way. An ECH experiment using this system was carried out in the last Nov. - Dec. . A ramp up of the plasma current by ECH of the LH sustained plasma, and local bulk heating of a tokamak plasma in which the core heating efficiency was the same as the foundamental wave ECH were obtained as reported in 5). We are going to get an another gyrotron and power up will be completed in this winter.

Acknowledgements

We would like to express our gratitude to Drs. R.Prater, C.P.Moeller, S.H.Lin and Messers D.Remsen, D.Irwin of GA Technologies Inc., San Diego, CA, USA, who carried out a pioneer work of making and operating a 60 GHz ECH system and carried out the ECH experiments on Doublet III tokamak to which two of the authors (K.H. and T.Y.) took part in. Though the design of our microwave components is different from their components, the basic layout of our transmission system is similar to theirs. We would like to acknowledge Dr. M.Sato of the Heliotron Center of Kyoto Univ. for his advice about the ECH system and many engineers of Mitsubishi Electric Co., who manufactured the ECH system. We are grateful to Mr. K.Suzuki, Drs. A.Funahashi, Y.Tanaka, M.Tanaka, Y.Obata, M.Yoshikawa, K.Tomabechi, Y.Iso and S.Mori of JAERI for their continuous encouragements.

References

1) LaHaye R.J., Moeller C.P., Funahashi A., Yamamoto T., Hoshino K., Suzuki N., Wolfe S.M., Efthimion P.C., Toyama H., and Roh T.: Nucl. Fusion 21, 1425 (1981).
2) Moeller C.P., Chan V.S., LaHaye R.J., Prater R., Yamaoto T., Funahashi A., Hoshino K., and Yamauchi T.: Phys. Fluids 25, 1211 (1982).
3) Prater R., and Moeller C.P.: Proc. of Third Joint Varenna-Grenoble Int. Symp. on Heating Toroidal Plasmas, 635 (1982).
4) Hoshino K., Yamamoto T., Funahashi A., Suzuki N, Matoba T., Yamauchi T., Matsumoto, H., Kawakami T., Kimura H., Konoshima S., Maeno M. et al.: J. Phys. Soc. Jpn. 54, 2503 (1985).
5) Hoshino K., Yamamoto T., Suzuki N., Uesugi Y., Kawashima H., Matoba T., Kasai S., Kawakami T., Maeno M., Matsuda T., Matsumoto H., Miura Y. et al.: in Proc. of the 12th European Conf. on Controlled Fusion and Plasma Physics, Budapest, Hungary, Sept. 2-7 vol. 2 p.184 (1985).
6) Stix T.H.: "The Theory of Plasma Waves", McGraw-Hill Book Co., Chap 1 & 9 (1962).
7) Ott E., Hui B., and Chu K.R.: Phys. Fluids 23, 1031 (1980).
8) Chandrasekhar S.: "Radiative Transfer", Dover Publications Inc., Chap 1 (1960).
9) Bornatici M., Cano R., Barbieri O., and Englemann F.: Nucl. Fusion 23, 1153 (1983).
10) Moeller C.P.: GA-A 16690 (1982).
11) Prater R., and Moeller C.P.: GA-A 16816, UC-20 (1982).
12) Moeller C.P.: GA-A 16784 (1982), Int. J. Electronics 53, 587 (1982).
13) Oguchi B.: "Microwave and Millimeter Wave Circuits" (in Japanese), Maruzen Publications Co., Ltd. (1964).
14) Hoshino K., Kawashima H., Hata K., and Yamamoto T.: JAERI-M Report 83-148 Sept. (1983).

APPENDIX 1. RF CURRENT-DRIVE(LHH+ECH) AND ELECTRON CYCLOTRON HEATING EXPERIMENTS ON JFT-2M TOKAMAK (A paper presented at 12th European Conference on Controlled Fusion and Plasma Physics, Budapest, Hungary, Sep. 2-6, 1985)

1. ABSTRACT

RF current-drive/ramp-up by the simulaneous injection of the lower hybrid were(LHW) and the electromagnetic wave of the frequency near the second harmonic electron cyclotron frequency(ECW) is investigated in the JFT-2M tokamak. A significant ramp-up of the toroidal current of 48 kA/sec is observed by the electron cyclotron heating(ECH) of the LH sustained tokamak plasma. Further, the local bulk electron heating by the second harmonic extraordinary mode (X-mode) ECH is observed.

2. INTRODUCTION

The rf current drive using the ECW seems to have several attractive features. First, it is possible to place the antenna far away from the plasma without the coupling problem. Second, the penetration of the ECW in the high density plasma is possible by choosing the frequency above the cutoff frequency. Third, as the resonant coupling of the ECW to the electrons occurs in the parameter space in which the electron cyclotron resonance(ECR) condition is satisfied, the power deposition(or the current) can be controlled by choosing the ECR condition appropriately. Fourth, the theoretical current drive efficiency by the ECW is as large as 3/4 of that by the LHW[1]. Fifth, the threshold power of the ECW parametric decay instability is relatively large, which means that high power density can be transmitted to the plasma core region to maintain the current.

The difficulty hitherto encountered to obtain the ECH driven current by the bulk heating of the plasma lies in that the large single path absorption sufficient for the energy absorption to occur in one side of the ECR layer[2] is needed. And there is a possibility that the drive efficiency may deteriorate by the tranpped particle effect by the bulk heating.

But by using the relativistically down shifted ECR of the high energy electrons, these difficulties are avoided. The reflection at

the vessel wall may increase the power deposition at the shifted ECR layer even if the absorption in single path is not large. Moreover, it was revealed that the current drive efficiency J/Pd is improved by the wave coupling to the high energy electrons[1),2)].

The combined effects of LHH+ECH are studied on the JFT-2M tokamak (R = 1.31 m, a = 0.35 m) experimentally. The frequency of the LHW is 750 MHz, and the spectrum of the parallel refractive index is controlled by four wave-guides[4)]. The launcher spectrum concentrates dominantly around $n_{/\!/} = 1 \sim 3$ when the phase difference is -90°. The frequency of the ECW is 60 GHz. The second harmonic X-mode with $n_{/\!/} = -0.17$ of the narrow beam divergence is launched in almost linear TE_{11} mode from the low field side of the torus.

3. LHH+ECH CURRENT DRIVE

Time evolutions are depicted in Fig. 1(a). The toroidal electric field is applied by the primary OH circuit in the initial 100 ms for the production of the target plasma, and then the primary voltage is shut down and held zero (AVR operation). The application of the LHW of pulse length ~400 ms and power 70 kW starts before the shut down of the primary voltage. In this way, the quick ramp-up of the plasma current I_p by the LHW is obtained. Ramp-up only by the LHW without the initial OH field takes longer time with less stability to reach 10 kA level of the driven current.

A saturation of the LHW driven current around $I_p \simeq 18$ kA with the efficiency 0.26 A/W is observed. The ECH pulse is applied for 100 ms during the saturation phase. A significant ramp-up of the current occurs almost linearly in time as shown in the figure. During the ECH pulse, the loop voltage drops and the plasma density changes. In this case, the 2nd harmonic ECR layer locates at $r_o = 0.1$ m outside and the plasma displacement is held inside of the center of the vacuum vessel with $B_{t0} = 1.15$ T.

The time rate of the current rise $(d/dt) I_p$ as a function of B_{t0} is given in Fig. 1(b). $\dot{I}_p$ has two peaks. A peak around $B_{t_0} = 1.0$ T corresponds to the location of the ECR layer around the plasma core which is shifted inside, and indicates the contribution of the bulk ECH to the current rise. The second peak in $B_{t_0} = 1.15 \sim 1.30$ T seems to be due to the coupling of the ECW to the LH sustained tail

electrons. The drive mechanisms are different between the two cases, namely, the coupling to the bulk electrons causes an increase in the bulk electron temperature which enhances the damping of the LHW and then the plasma current. The drive efficiency, however, stays constant. On the other hand, the second case is due to the coupling of the ECW to the LH sustained tail. There are marked different results between the two cases. In the former case, the increased current does not decrease after the ECH pulse, which implies that a new saturation level is set for the LHW current drive by the effect of bulk ECH, for instance, by increase in the bulk electron temperature. On the other hand, in the latter case, the current decrease after the end of the ECH pulse, indicating that the increased current is attributed to the ECW. The time behaviour of the density is also different between the two cases as shown in the figure. The density drop of B_{t0} = 1.0 T case is larger than that of B_{t0} > 1.1 T case in which a gradual increase in density occurs after the small density drop at the beginning of the ECW pulse. The ECW coupling to the trapped electrons at the ECR layer in the low field side may affect the paraticle transport.

The resonant energy of an electron is obtained as shown in Fig. 5-1(c) by the relativistic ECR condition

$$1-s\omega_{ce}/\omega - n_{/\!/} v_{/\!/}/c = 0 \qquad (s = 1, 2, 3, \ldots).$$

A divergence of the microwave beam from the horn antenna gives a spread of $-0.26 < n_{/\!/} < -0.09$. Owing to the 2nd harmonic resonance (s = 2), ECW couples to the tail electrons at the center of the vessel which have the energy of 12 ~ 17 keV in B_{t0} = 1.15 T (r_0 = .10 m) case, 20 ~ 45 keV in B_{t0} = 1.20 T (r_0 = .16 m) case and 45 ~ 85 keV in B_{t0} = 1.30 T (r_0 = .28 m) case. The resonant energy of the plasma core shifted inside is even higher. The energy spectrum analysis of the soft X-ray radiation shows that an increase of the photon counts of energy up to 80 keV occurs and the increment is a few times as large as the radiation from the LH sustained plasma. The contribution from the s = 3 resonance seems to be samll which is derived from the negligible $\dot{I}_p$ in $B_{t0} < 0.8$ T cases. The soft X-ray measurement shows also that the emission region is highly localized inside of the center of the chamber during the ECH pulse, implying that the current channel is localized inside. In the B_{t0} = 1.40 T case in which no bulk ECR

layer exists in the plasma column, the coupling to the tail electrons is detected by the ECE measurement in spite of no increase in the current. The increase in I_p decreases as the plasma density increases because of the decrease of the LH tail.

These observations show the coupling of the ECW to the high energy tail electrons satisfying the resonance condition, and resulting localized current channel. It brings the possibility of the formation of the hot electron channel in the high temperature tokamak plasmas which is proposed to stabilize the high beta tokamak plasmas[5].

4. BULK ELECTRON HEATING BY THE SECOND HARMONIC X-MODE ECH

Bulk ECH by a 28 GHz fundametal (s = 1) wave was investigated on the JFT-2 tokamak by launching three different modes[6]. In the JFT-2M, the bulk ECH by the 60 GHz 2nd harmonic (s = 2) X-mode is studied. The calculated absorption in single path is given in Fig. 2(a). The absorption rate increases with plasma density n_e and electron temperature T_e of the ECR layer. More than 80 % of the wave power is absorbed in the parameter region of $T_e > 500$ eV and $n_e > 1.0 \times 10^{19}$ m^{-3}. Therefore the local core heating by ECH is expected in the JFT-2M.

The experimental result of the density dependence of the increase of the center electron temperature ΔT_{eo} and the value $\Delta\Lambda \equiv \Delta(\beta_p + l_i/2)$, where β_p denotes poloidal beta value and l_i denotes the internal inductance, are plotted in Fig. 2(b). Calculated cutoff density of X-mode and O-mode is expressed by arrows in the abscissa. It is shown that the wave cutoff occurs above the right hand cutoff density. The ΔT_{eo} which is linear in rf power in $r_o = 0$ m case, depends much on r_o as shown in Fig. 2(c). In the off-center heating in which r_o = -0.13 m, +0.18 m, no increase in T_{eo} is observed. However, a drop in the loop voltage and increase of the laser electron temperature around the ECR layer are obtained. Namely, the temperature profile becomes broad. The change in l_i affects $\Delta\Lambda$ and the effect is not negligible, because the increase in β_p is small due to the decrease of the joule power during the ECH pulse the power of which is less than the jould power. The density drop by ECH was large in the off-center heating and was proportional to the plasma density as were observed in the 28 GHz on the JFT-2. A comparison with the fundamental ECH shows

almost the same core heating efficiency $\eta \equiv \Delta T_{eo} \bar{n}_e / P_{rf} / R = 5 \times 10^{19}$ eV/kW/m^4.

These observations show the local heating and the possibility of the profile control by the 2nd harmonic X-mode ECH. No impurity problem is observed up to the power level of 80 kW, which is one of the advantages of ECH.

REFERENCES OF THE APPENDIX 1

1) N.J.Fisch and A.H.Boozer, Phys. Rev. Lett., 45, 720 (1980).
2) O.C.Eldridge, ORNL/TM-7503 (1980).
3) I.Fidone, G.Giruzzi, G.Granata el al., Phys. Fluids, 27, 2468 (1984).
4) Y.Uesugi, K.Hoshino, T.Yamamoto el al., submitted to Nucl. Fusion.
5) J.Y.Hsu, C.S.Liu, R.Prater el al., GA-A 17731 (1984).
6) K.Hoshino, T.Yamamoto, A.Funahashi et al., J. Phys. Soc. Jpn., 54, 2503 (1985).

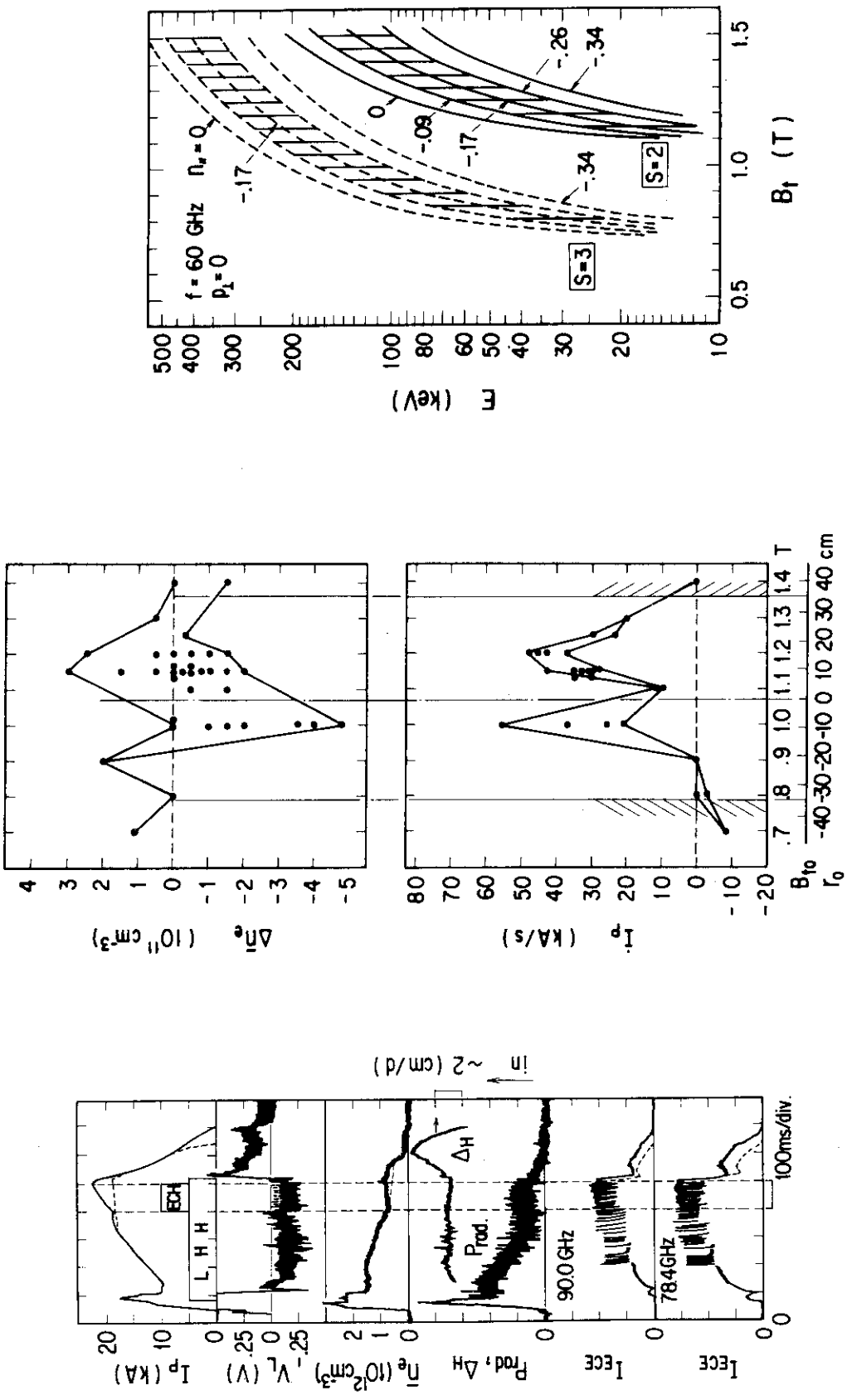

Fig. 1(a) Time evolutions. B_{to} = 1.15 T, P_{LH} = P_{ECH} = 70 kW. Δ_H denotes the displacement of the plasma column.

Fig. 1(b) $\dot{I}_p$ and $\Delta\bar{n}_e$ during the ECH pulse. r_o denotes the minor position of the bulk ECR layer (s = 2).

Fig. 1(c) Resonant energy v.s. the local magnetic field B_t. s denotes the harmonic number of the ECR.

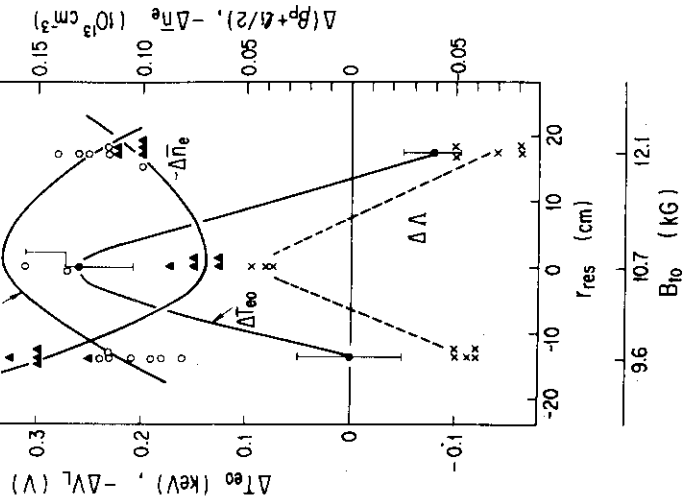

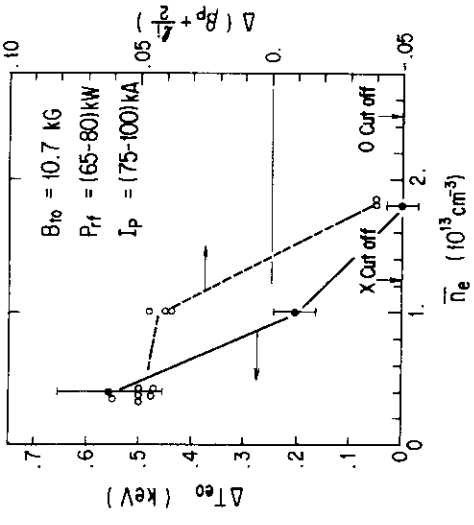

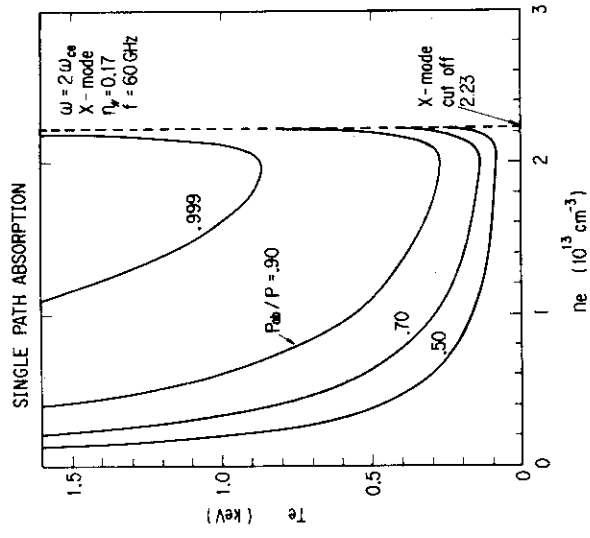

Fig. 2(a) Calculated power absorption rate P_{ab}/P_{rf} at the 2nd harmonic ECR layer. f = 60 GHz, $n_{//}$ = 0.17. Cutoff of the X-mode occurs at $n_e = 2.23 \times 10^{19}$ m^{-3} which is the right hand cutoff density.

Fig. 2(b) Density dependence of the increase in the center electron temperature ΔT_{eo} and the value $\Delta\Lambda \equiv \Delta(\beta_p + l_i/2)$. Position of the ECR layer is at the center of the chamber r_o = 0 m. Base $T_{eo} \simeq$ 700 eV (low density case) and $T_{eo} \simeq$ 600 eV (higher density cases).

Fig. 2(c) Dependence on the minor position of the ECR layer. $\bar{n}_e$ = 1.0×10^{19} m^{-3}, P_{rf} = 80 kW, I_p = 100 kA.

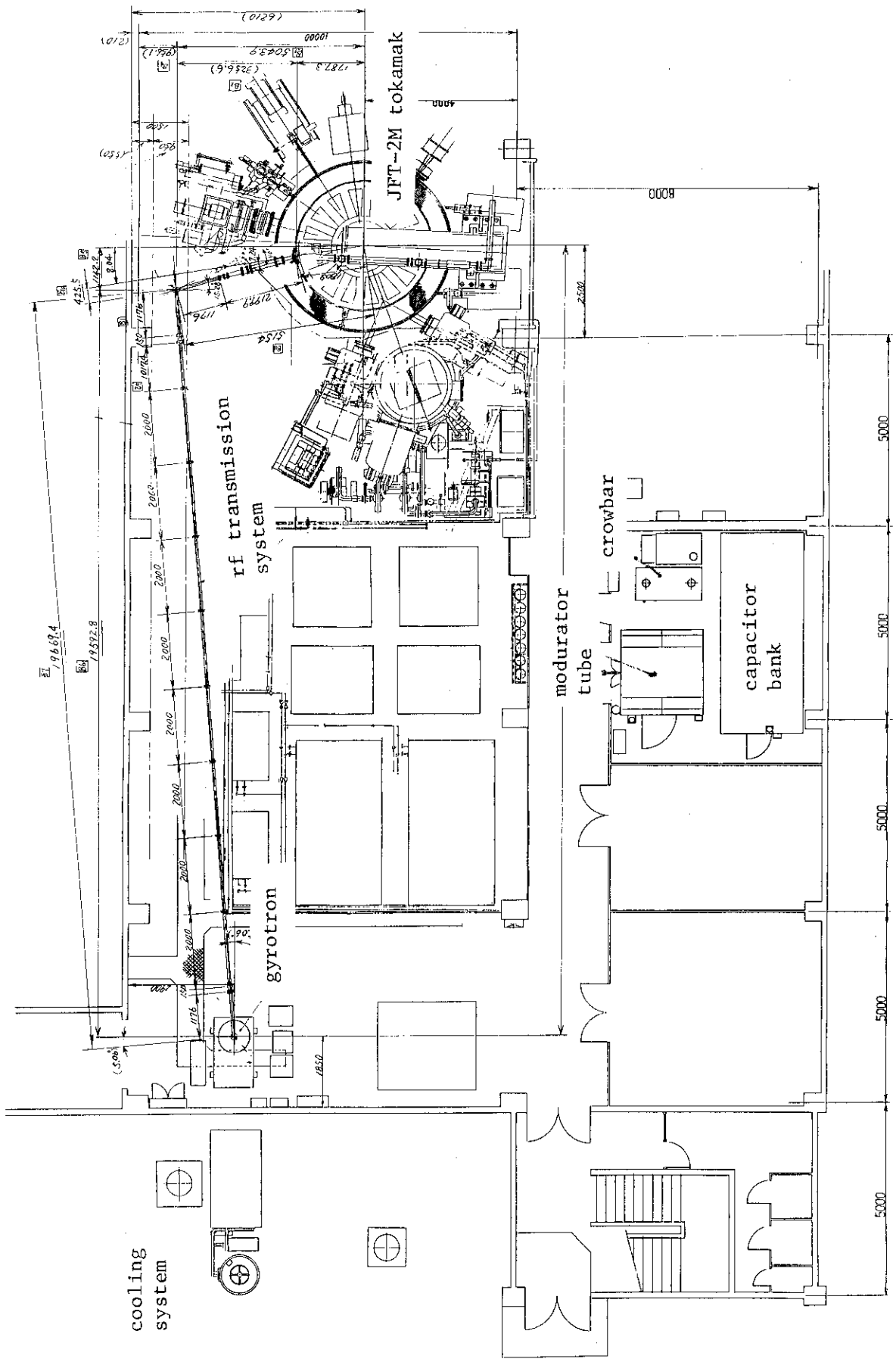

Appendix 2. Layouts of the ECH system

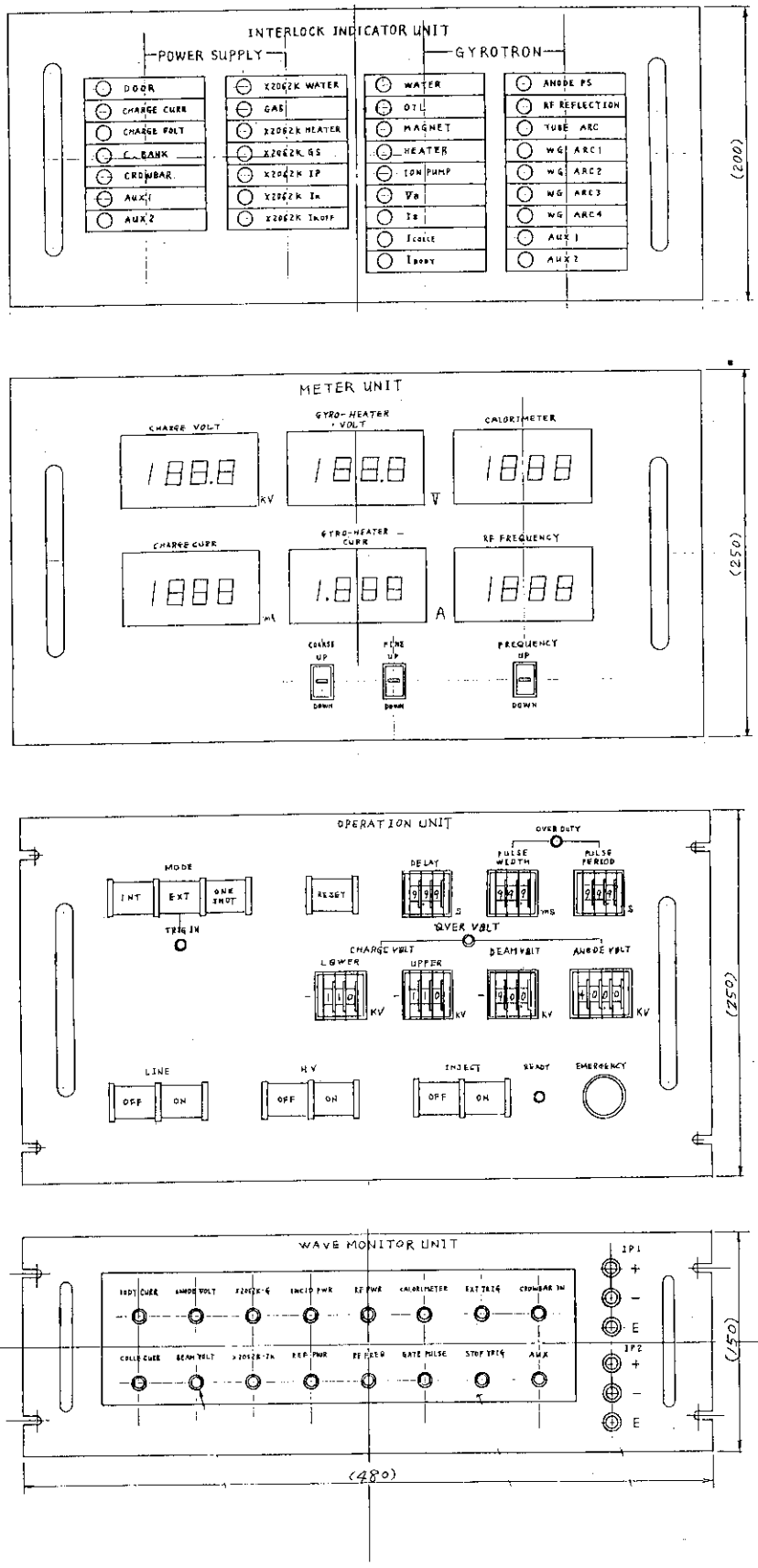

Appendix 3. Main control panel of the ECH system

(a)

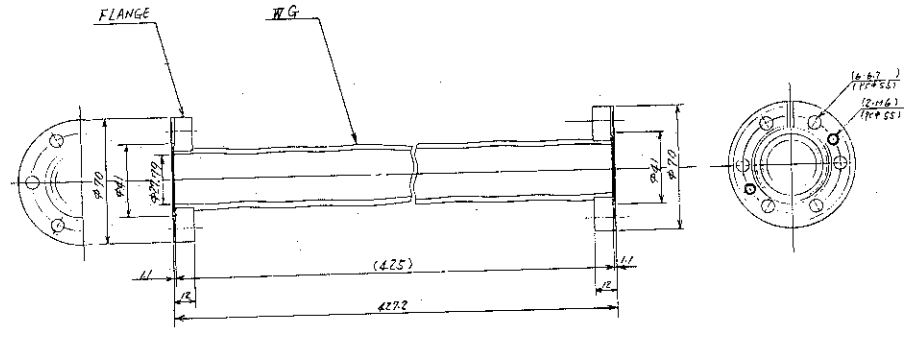

(b)

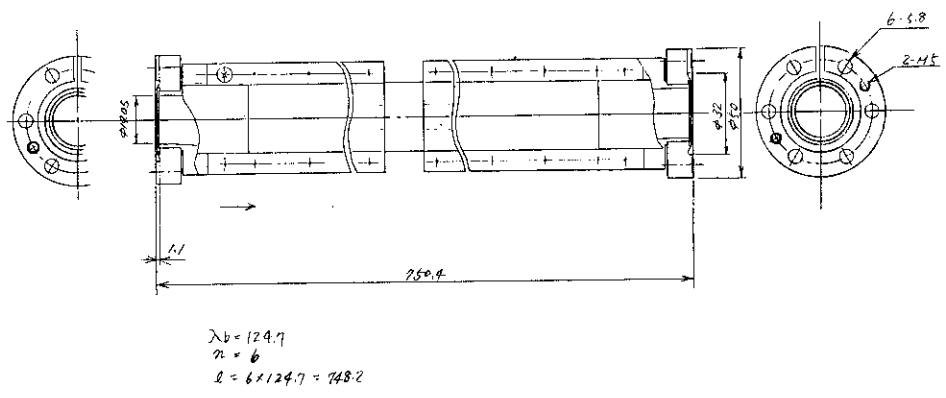

(c)

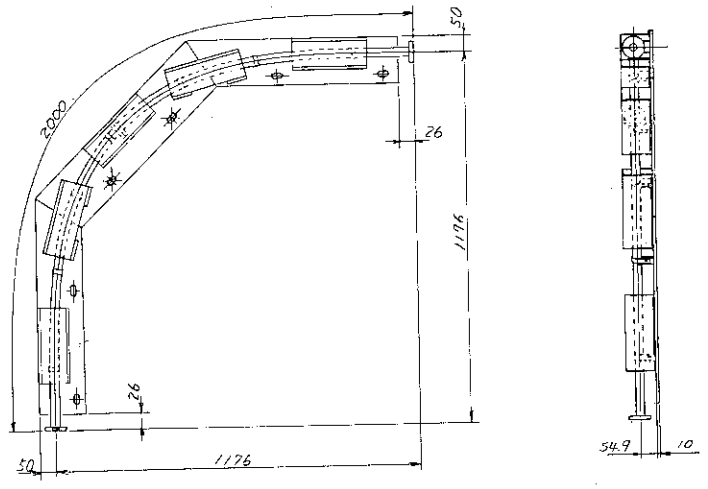

Appendix 4. Drawings of the microwave components
(a) TE_{02}-TE_{01} mode converter
(b) TE_{01}-TE_{11} mode converter
(c) Corrugated bend